





The Mean Metal-line Absorption Spectrum of Damped Ly α Systems in BOSS

Lluís Mas-Ribas^{1,2} , Jordi Miralda-Escudé^{2,3}, Ignasi Pérez-Ràfols^{2,4}, Andreu Arinyo-i-Prats² , Pasquier Noterdaeme⁵, Patrick Petitjean⁵, Donald P. Schneider^{6,7}, Donald G. York⁸, and Jian Ge⁹

¹Institute of Theoretical Astrophysics, University of Oslo, Postboks 1029, NO-0315 Oslo, Norway; l.m.ribas@astro.uio.no

²Institut de Ciències del Cosmos, Universitat de Barcelona (UB-IEEC), Barcelona E-08028, Catalonia, Spain

³Institució Catalana de Recerca i Estudis Avançats, Barcelona, Catalonia, Spain

⁴Departament de Física Quàntica i Astrofísica, Universitat de Barcelona, E-08028, Catalonia, Spain

⁵Institut d'Astrophysique de Paris, UPMC & CNRS, UMR7095 98bis Boulevard Arago, F-75014—Paris, France

⁶Department of Astronomy and Astrophysics, The Pennsylvania State University, University Park, PA 16802, USA

⁷Institute for Gravitation and the Cosmos, The Pennsylvania State University, University Park, PA 16802, USA

⁸Department of Astronomy and Astrophysics and the Enrico Fermi Institute, University of Chicago, 5640 South Ellis Avenue, Chicago, IL 60637, USA

⁹Department of Astronomy, University of Florida, Bryant Space Science Center, Gainesville, FL 32611-2055, USA

Received 2016 October 9; revised 2017 July 17; accepted 2017 July 21; published 2017 August 24

Abstract

We study the mean absorption spectrum of the Damped Ly α (DLA) population at $z \sim 2.6$ by stacking normalized, rest-frame-shifted spectra of $\sim 27,000$ DLA systems from the DR12 of the Baryon Oscillation Spectroscopic Survey (BOSS)/SDSS-III. We measure the equivalent widths of 50 individual metal absorption lines in five intervals of DLA hydrogen column density, five intervals of DLA redshift, and overall mean equivalent widths for an additional 13 absorption features from groups of strongly blended lines. The mean equivalent width of low-ionization lines increases with $N_{\text{H I}}$, whereas for high-ionization lines the increase is much weaker. The mean metal line equivalent widths decrease by a factor ~ 1.1 – 1.5 from $z \sim 2.1$ to $z \sim 3.5$, with small or no differences between low- and high-ionization species. We develop a theoretical model, inspired by the presence of multiple absorption components observed in high-resolution spectra, to infer mean metal column densities from the equivalent widths of partially saturated metal lines. We apply this model to 14 low-ionization species and to Al III, S III, Si III, C IV, Si IV, N V, and O VI. We use an approximate derivation for separating the equivalent width contributions of several lines to blended absorption features, and infer mean equivalent widths and column densities from lines of the additional species N I, Zn II, C II*, Fe III, and S IV. Several of these mean column densities of metal lines in DLAs are obtained for the first time; their values generally agree with measurements of individual DLAs from high-resolution, high signal-to-noise ratio spectra when they are available.

Key words: cosmology: observations – galaxies: abundances – intergalactic medium – quasars: absorption lines

1. Introduction

The existence of luminous quasars at high redshift is a gift of Nature. It allows us to explore in an unbiased way any population of gas clouds in the universe by means of the absorption lines they produce in the spectra of the background sources. Without luminous quasars, we would not have sources at high redshift that are sufficiently bright to obtain spectra of high resolution and signal-to-noise ratio (S/N) in which the Ly α line, as well as numerous ultraviolet metal absorption lines, are shifted to the optical range and can easily be observed from the ground. Damped Ly α systems (DLAs, hereafter; Wolfe et al. 1986) are generally defined to have hydrogen column densities $N_{\text{H I}} > 2 \times 10^{20} \text{ cm}^{-2}$. Systems of this high column density have two important characteristics: (i) they are self-shielded from the external cosmic ionizing background, implying that the hydrogen in these systems is mostly in atomic form (Vladilo et al. 2001), and (ii) the damped profile of their hydrogen Ly α line is clearly visible even in low-resolution spectra, so the column density can be measured from the absorption profile (see Wolfe et al. 2005; Barnes et al. 2014, for detailed reviews). DLAs provide a reservoir of atomic gas clouds that were available at high redshift for the formation of galaxies. The mean cosmic density of baryons contained in these systems is directly obtained from the measurements of the column density distribution, and accounts for a small fraction of the critical density $\Omega_{\text{DLA}} \simeq 10^{-3}$ at redshifts $2 < z < 3.5$ (e.g., Péroux et al. 2003b, 2005; Prochaska et al. 2005;

Noterdaeme et al. 2012; Zafar et al. 2013; Crighton et al. 2015; Padmanabhan et al. 2015; Sánchez-Ramírez et al. 2016). This value corresponds to $\sim 2\%$ of all the baryons in the universe, comparable to the fraction of baryons that had turned into stars at these redshifts (Prochaska et al. 2005; Noterdaeme et al. 2009; Prochaska & Wolfe 2009).

The metal absorption lines of DLAs have been explored since their discovery. High-resolution spectra reveal a diversity of velocity structures of the absorbers, characterized by multiple components. Sometimes a single component with a narrow velocity width close to the thermal value for photoionized gas clouds is observed, but often several components are seen over a typical velocity range ~ 100 – 300 km s^{-1} (Prochaska & Wolfe 1997; Zwaan et al. 2008). The derived metallicities are generally low, distributed over a broad range of 10^{-3} – $10^{-1} Z_{\odot}$ (Prochaska & Wolfe 2002; Prochaska et al. 2003b; Kulkarni et al. 2005; Ledoux et al. 2006), and on average declining with redshift (Kulkarni & Fall 2002; Vladilo 2002; Calura et al. 2003; Prochaska et al. 2003a; Khare et al. 2004; Akerman et al. 2005; Kulkarni et al. 2005; Rafelski et al. 2012, 2014; Jorgenson et al. 2013; Møller et al. 2013; Neeleman et al. 2013; Quiret et al. 2016). The complex velocity profiles suggest a highly turbulent environment, and models of clouds moving in random orbits in galactic halos or thick disks can generally explain the observations (Haehnelt et al. 1998; Fumagalli et al. 2011; Cen 2012; Barnes & Haehnelt 2014; Rahmati & Schaye 2014; Bird et al. 2015; Neeleman et al. 2015, but see also York et al. 1986).

The fact that several absorbing components are typically seen along a given line of sight, each corresponding to clouds moving at different velocities within a larger halo, implies that these clouds are colliding with each other about once every orbital period (McDonald & Miralda-Escudé 1999). For individual DLAs it can be difficult to model the column densities and velocity structure of the metal species due to a complex variety of gas phases arising from photoionization, shock-heating and collisions, leading to a broad range of temperatures and densities (e.g., Fox et al. 2007b; Berry et al. 2014; Dutta et al. 2014; Lehner et al. 2014; Cooke et al. 2015; Neeleman et al. 2015; Rubin et al. 2015).

In the context of the Cold Dark Matter model of structure formation, the nonlinear collapse of structure leads to hierarchical merging of dark matter halos. The cosmological theory, starting from a matter power spectrum that is now accurately determined from observations of the Cosmic Microwave Background (Planck Collaboration 2015, and references therein), predicts the number density of halos as a function of halo mass that exist at any epoch, $n(M_h, z)$. The observed rate of DLAs per unit of redshift in any random direction due to halos of mass M_h in the range dM_h is then $n(M_h, z) \Sigma(M_h, z) c dt/dz dM_h$, where $\Sigma(M_h, z)$ is the mean cross section (or area) within which a DLA is observed in a halo of mass M_h . Although it has been generally believed that DLAs are associated with dwarf galaxies (e.g., York et al. 1986; Dessauges-Zavadsky et al. 2004; Khare et al. 2007; Fumagalli et al. 2014; Bland-Hawthorn et al. 2015; Cooke et al. 2015; Webster et al. 2015), observations of the large-scale cross-correlation amplitude of DLAs with the Ly α forest absorption have determined their mean bias factor $b_{\text{DLA}} \simeq 2$ (Font-Ribera et al. 2012), which is consistent with DLAs being distributed over a broad range of halo masses $10^9 M_\odot \lesssim M_h \lesssim 10^{13} M_\odot$, from dwarf galaxies to halos of massive galaxies and galaxy groups.

The Baryon Oscillation Spectroscopic Survey (BOSS; Dawson et al. 2013) of the Sloan Digital Sky Survey-III (SDSS-III; Eisenstein et al. 2011) has obtained spectra for more than 160,000 quasars at $z > 2$, providing an unprecedentedly large sample of DLAs. Despite the relatively low resolution ($R \sim 2000$) and S/N of the BOSS spectra, the large number of observed DLAs allows an accurate measurement of the mean metal-line absorption strength by stacking many systems, and studying the dependence of the equivalent widths of any line on the hydrogen column density. This approach has the advantage of directly providing mean properties of the DLA population, rather than properties of individual systems which have a large intrinsic random variation. Although the study of individual systems in detail obviously results in invaluable additional information that is lost in a stacked spectrum of the global DLA population, even a single DLA has absorption that probes a mixture of different gas phases and is difficult to model in practice. Moreover, absorption lines that are located in the Ly α forest region can be accurately measured only after averaging over a large number of absorption systems, and they can provide important information that is not accessible from lines on the red side of Ly α (see Rahmani et al. 2010; Khare et al. 2012; Noterdaeme et al. 2014, for an analysis of composite DLA spectra from BOSS).

This paper presents the mean absorption spectra of metal lines in DLAs that are derived from the Data Release 12 (Alam et al. 2015) of BOSS, using the DLA catalog generated with the technique described in Noterdaeme et al. (2009). The two main results are: (i) the mean dependence of the equivalent width of

each metal species on the hydrogen column density, and (ii) an analytical model of the mean equivalent widths of multiple absorption lines of the same metal species to account for the effect of saturation and derive mean column densities in our DLA sample. We also present for the first time the mean equivalent widths in DLAs of various species that are usually difficult to measure owing to the confusion with the Lyman forest, e.g., S IV, S III, Fe III, and N II, as well as accurate determinations of the mean equivalent width and inferred column densities of more commonly measured species like O VI.

In Section 2, we present the method to calculate the mean quasar continuum spectrum and the DLA stacked absorption spectrum. We also detail the corrections we apply to improve the mean quasar continuum which, in turn, results in a more reliable stacked spectrum. In Section 3 we compute the mean equivalent width of detected metal lines; their dependence on the hydrogen column density is assessed and presented in Section 4, and in Section 5 we address the dependence on DLA redshift. In Section 6, a simple model is proposed to correct for line saturation and is used to infer the mean column densities of several low- and high-ionization species for which the mean equivalent width of absorption lines has been measured. We discuss our results in Section 7, before summarizing and concluding in Section 8.

All the equivalent widths in this paper are rest-frame.

2. Data Analysis

We use the spectra of quasars in the SDSS-III BOSS Data Release 12 Quasar Catalog “DR12Q” (Pâris et al. 2016). The SDSS telescope and camera are described in detail in Gunn et al. (1998, 2006), Ross et al. (2012), and the SDSS/BOSS spectrographs in Smee et al. (2013).

We use the DR12 DLA catalog, which is the expanded version of the catalog presented in Noterdaeme et al. (2012) for the DRQ9 (Pâris et al. 2012), and contains a total of 34,593 DLA candidates with a measured column density $N_{\text{H I}} > 10^{20} \text{ cm}^{-2}$. The detection of these systems is performed by means of a fully automatic procedure based on profile recognition using the Spearman correlation analysis, as described in Noterdaeme et al. (2009). Only 19,376 of the DLAs in the catalog have $\log(N_{\text{H I}}/\text{cm}^{-2}) > 20.3$ and can therefore be designated DLAs if we strictly use the standard definition. This column density threshold was, however, set for observational purposes, and to ensure that the hydrogen gas in the inner regions of the DLAs is mostly neutral due to self-shielding from the background radiation (Wolfe et al. 1986). We include systems down to $\log(N_{\text{H I}}/\text{cm}^{-2}) > 20$ because we find them to be also useful to characterize the mean properties of the population and their dependence on column density. We demonstrate below (Section 6.4) that the inclusion of systems with $\log(N_{\text{H I}}/\text{cm}^{-2}) < 20.3$ does not substantially change our results, although the mean equivalent widths do change with column density and redshift and, therefore, accurate comparisons with other stacked spectra in the future need to take into account our distribution of column densities and redshifts. A relatively low minimum continuum-to-noise ratio $C/N > 2$ is required to include a DLA in the catalog, with the goal of maximizing the size of the catalog without having a large number of false DLAs arising from spectral noise (Noterdaeme et al. 2012). This C/N threshold is specially important for systems with low column

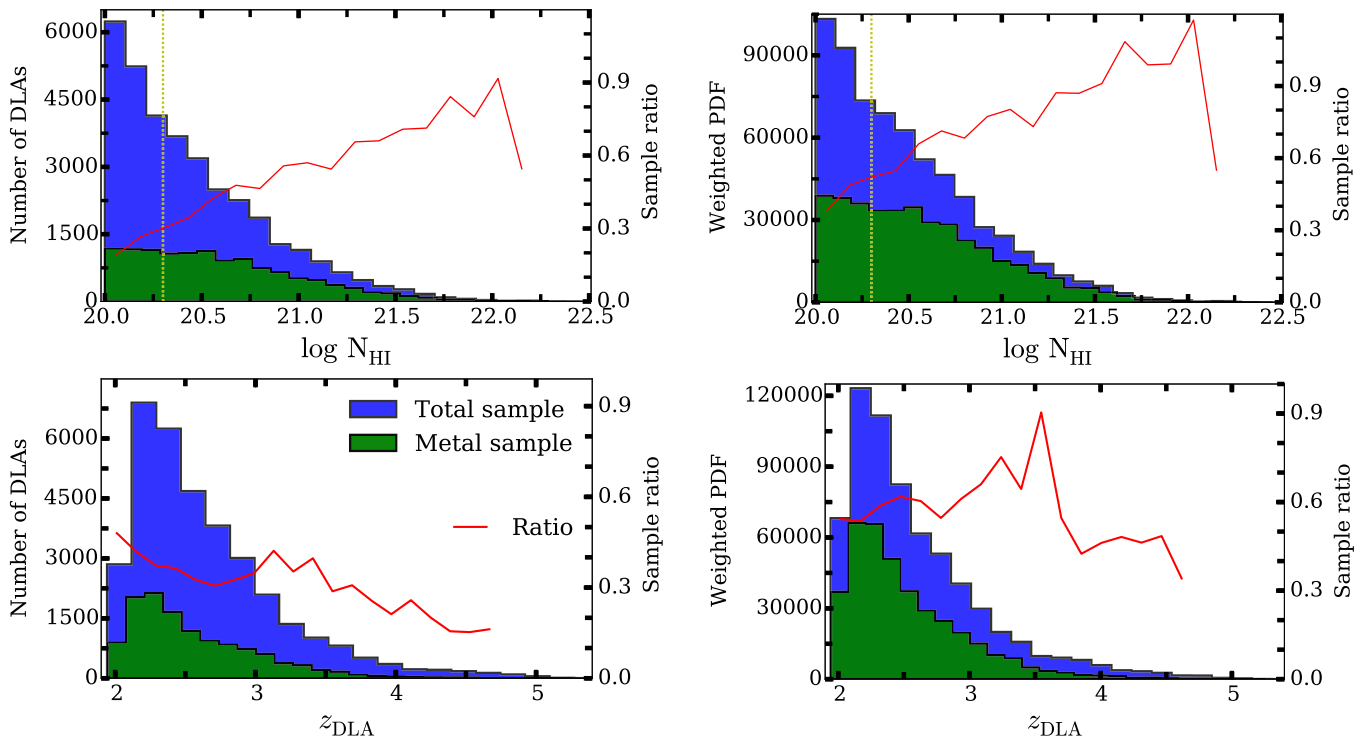


Figure 1. Left panels: neutral hydrogen column density (top) and redshift (bottom) distributions for the total sample (blue histogram, 34,593 DLAs) and the metal sample (green histogram, 12,420 DLAs) of the entire DLA catalog. Right panels: same distributions as in the left panel but considering only the systems that are used for the calculation of the composite spectra, after the application of our cuts, and weighting them according to the signal-to-noise calculation described in Section 2.1. These weighted total (blue histogram, 26,931 DLAs) and metal sample (green histogram, 10,766 DLAs) distributions are the true ones that give rise to the results presented in this work. In all panels, the red lines denote the ratio of DLAs between the metal and total samples, and the vertical dashed lines in the upper panels indicate the strict DLA column density lower limit, $N_{\text{HI}} = 2 \times 10^{20} \text{ cm}^{-2}$.

density since these have a higher probability to be false detections.

Most of the results presented in this paper are obtained from stacks using the whole DLA catalog, which is designated here as the **total sample**. This sample should be unbiased, in the sense that only the HI Ly α absorption line has been used to select the DLAs, and not the strength of the metal lines. However, DLA samples from optically selected quasars may be biased against systems containing substantial amounts of absorbing dust (e.g., Fall & Pei 1993; Boisse et al. 1998; Ellison et al. 2001; Smette et al. 2005; Noterdaeme et al. 2015), although the presence of dust in DLAs is expected to be small (e.g., Pettini et al. 1997; Akerman et al. 2005; Vladilo et al. 2008; Khare et al. 2012; Murphy & Bernet 2016, see also Kulkarni et al. 2005; Fukugita & Ménard 2015; Krogager et al. 2016). The presence of dust-biasing would have little impact on general HI studies (Trenti & Stiavelli 2006; Ellison et al. 2008), but it may significantly underestimate the metal content in DLAs (Pontzen & Pettini 2009). In addition, we study a subsample of the DLA catalog, which we call the **metal sample**, containing 12,420 DLA candidates where metal lines can be individually detected by using templates (of these, 8699 have $\log(N_{\text{HI}}/\text{cm}^{-2}) > 20.3$). The metal detection results from a cross-correlation of the observed spectrum with an absorption template containing the most prominent low-ionization metal absorption lines, which is done in addition to the previous Spearman correlation analysis for the Ly α line. If one or more metal absorption lines are detected in the individual spectra, these are used to refine the absorption redshift of the DLA (see Section 3.2 in Noterdaeme et al. 2009 for further details). The improved redshift of systems in the metal sample gives rise to

more sharply defined lines in the resulting stack, and allows detection of the weakest metal lines and measurement of the effect of redshift uncertainties in the total sample. However, the metal sample is obviously biased in favor of DLA systems with strong metal lines and/or high S/N, and therefore cannot be used to obtain mean properties of the true population of DLAs. The absence of metal lines is never used to discard candidate DLAs at a low S/N from the total sample. The mean stacked spectra of the DLAs used in each of these two samples are computed in a similar way, except for a few differences that are discussed below.

The left panels in Figure 1 present the redshift and N_{HI} distributions of the total (blue histogram) and the metal sample (green histogram). The ratio of the number of DLAs in the two samples is also denoted as the red line, with the scale on the right axis. The metal sample contains a greater fraction of high column density systems because the strength of metal lines increases, on average, with N_{HI} . The metal sample also has a smaller fraction of systems at high redshift, because of the declining mean metallicity of DLAs with redshift and the decreasing number of metal lines redward of Ly α that are observable with increasing redshift. In addition, the increased density of the Ly α forest at high redshift may give rise to an increase of false positive DLA detections, especially in the total sample (see, e.g., Rafelski et al. 2014). The right panels display the same two distributions as before, but now considering only the systems that are finally used for the calculation of the composite spectra, after the application of cuts in the DLA sample and after weighting the spectra as described in the next subsection. The distributions on the right panels are the actual ones that give rise to the results of this paper, which should be

used in order to precisely compare to any other future observational results or model predictions. The shape of the distributions in the right panels is similar to those in the left ones, but the metal sample has a higher contribution than in the left panels, in general. This difference is mostly because metal lines are more likely to be identified in high S/N spectra, which have higher weights, as explained in the next subsection, and because of the cuts that remove possible false DLAs in the catalog. Additionally, the redshift distribution of the total sample narrows when applying the cuts and weighting the spectra. The mean values for the total sample in the right (left) panels are $\log(\bar{N}_{\text{H I}}/\text{cm}^{-2}) = 20.49$ (20.70) for column density, and $\bar{z} = 2.59$ (2.65) for redshift.

2.1. Continuum Quasar Spectrum Calculation

A crucial part of computing a mean stacked spectrum of the transmitted flux fraction for a sample of DLAs is the calculation of the quasar continuum. We use a method similar to that in Pérez-Ràfols et al. (2014), who measured the mean absorption by Mg II around the redshift of a galaxy near the line of sight to a quasar. Some variations are necessary in our case, however, owing to the mean absorption by the Ly α forest and the presence of the DLA metal lines themselves. We now describe in detail our procedure for estimating the continuum.

The method starts by computing a mean spectrum of the quasars used in both the total and the metal sample. First, each quasar spectrum is shifted to the quasar rest-frame wavelength, $\lambda_r = \lambda_{\text{obs}}/(1+z_q)$, where λ_{obs} is the observed wavelength of every spectral bin, using the quasar redshift z_q provided in the DR12 DLA catalog (this is the visual inspection redshift of the quasar catalog from Pàris et al. 2016). The values and errors of the flux are rebinned into new pixels of width 1.0 Å in the rest-frame by standard interpolation, averaging the values in the original pixels as they are projected, partly or fully, onto the new pixels. Any pixels affected by skylines, as reported in Palanque-Delabrouille et al. (2013), are removed from the spectra and excluded from the analysis.

The spectrum of each individual quasar is then normalized by computing the mean flux in two fixed rest-frame wavelength intervals: $1300 \text{ \AA} < \lambda_r < 1383 \text{ \AA}$, and $1408 \text{ \AA} < \lambda_r < 1500 \text{ \AA}$. These intervals are chosen to avoid the principal broad emission lines of quasars and the region of the Ly α forest absorption, and to be roughly centered in the spectral range of interest for the DLA metal lines. The normalization factor for each quasar j is defined as

$$n_j = \sum_i \frac{f_{ij}}{N_j}, \quad (1)$$

where f_{ij} is the flux per unit wavelength in the pixel i of the quasar j , and the sum is done over all the N_j pixels that are located within the two wavelength intervals for the normalization. Some pixels in these two intervals are discarded because of the skylines that are removed or because of additional corrections discussed below (see Section 2.3). Any quasar for which more than 20% of the pixels in the normalizing intervals are discarded is removed from the sample. This results in the removal of 1074 quasars for the total sample and 298 for the metal sample.

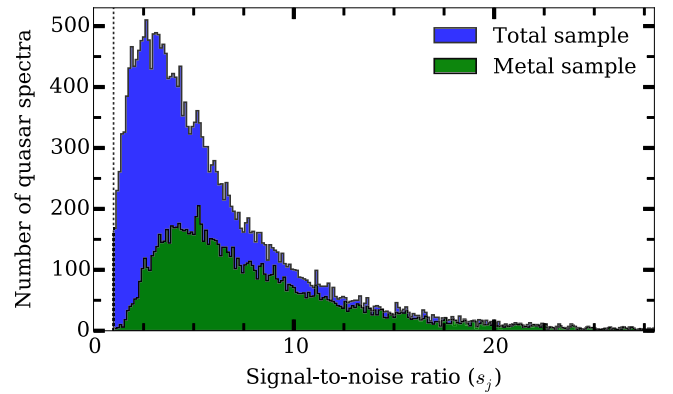


Figure 2. Distribution of the mean S/N parameter s_j for the total sample (blue) and the metal sample (green). Spectra with $s_j < 1.0$ have been discarded. The vertical dashed line denotes the point where S/N reaches the threshold unity value.

A mean S/N, s_j , is computed for each quasar spectrum using the same two rest-frame wavelength intervals,

$$s_j = \frac{\sum_i f_{ij}/N_j}{\left(\sum_i e_{ij}^2/N_j\right)^{1/2}}, \quad (2)$$

where e_{ij} is the uncertainty for the flux f_{ij} . The resulting distribution of the s_j parameter is presented in Figure 2 for the two samples. This distribution peaks at $s_j \simeq 2$ for the total sample, and at a higher value for the metal sample (as expected, because metal lines are more difficult to detect for low signal-to-noise). We discard from our sample any spectra with $s_j < 1.0$, because of their very poor quality, resulting in 264 and 5 spectra from the total and metal sample, respectively, not being further considered for our calculations. These discarded spectra are a small fraction of the total because of the independent constraint of a C/N > 2 in the Ly α forest region that was already applied to the DLA catalog with the method of Noterdaeme et al. (2009).

With the S/N values we assign a weight w_j to each quasar spectrum, defined as

$$w_j = \frac{1}{s_j^{-2} + \sigma^2}, \quad (3)$$

where σ is a constant that is introduced to prevent the quasars with highest s_j contributing excessively to the mean in the presence of an intrinsic variability of quasar spectra, in addition to observational noise. We choose, somewhat arbitrarily, a value $\sigma = 0.1$, which represents our estimate that the typical intrinsic variability of quasar spectra is 10%. We ran the stacking using $\sigma = 0.2$ and saw that this difference does not produce any relevant effect in our resulting spectrum.

Finally, the resulting mean normalized quasar spectrum is computed as a weighted mean,

$$\bar{f}_i = \frac{\sum_j w_j (f_{ij}/n_j)}{\sum_j w_j}, \quad (4)$$

where \bar{f}_i is the normalized flux per unit wavelength of the mean quasar spectrum at the quasar rest-frame wavelength pixel i . This mean quasar spectrum is displayed as the black line in Figure 3, with the most prominent emission lines labelled. This

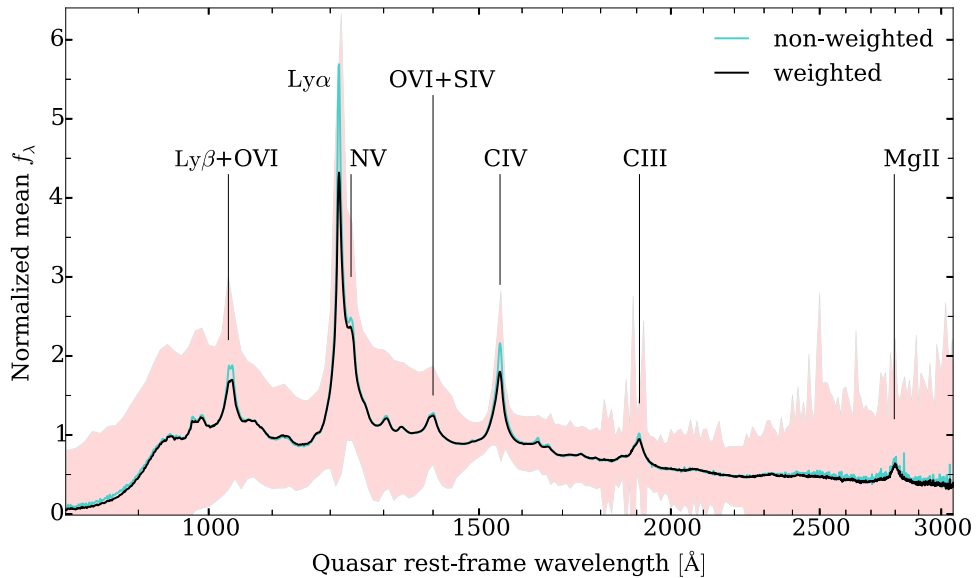


Figure 3. Mean quasar normalized spectrum for the total sample. The black line represents our weighted mean spectrum. For comparison, the cyan line denotes the non-weighted mean, resulting in stronger emission lines. The red region illustrates the 68% contours of the distribution of normalized spectra around the weighted mean. The wavelength scale is logarithmically spaced. We have labelled the most prominent emission lines.

is the mean spectrum of quasars that have (at least) a DLA absorption system. Therefore, the mean spectrum incorporates any mean modification that the DLA lines have produced. Some quasars ($\sim 20\%$ for both samples) have more than one DLA system in the catalog; in this case the same quasar contributes to the mean as many times as the number of DLAs it contains. The red region in Figure 3 illustrates the 68% contours of the distribution of normalized spectra around the mean. For comparison, we also plot the non-weighted mean, represented by the cyan line. This spectrum shows stronger emission lines compared to the weighted mean, because of the Baldwin effect: emission line equivalent widths decrease with quasar luminosity (Baldwin 1977). A small difference is also present in the $\text{Ly}\alpha$ forest region (barely visible in this plot), which is likely due to small variations of the distribution of S/N with redshift. Apart from this, we see that the black line is less noisy than the cyan one, which is our main reason for using the weights for computing the mean quasar spectrum.

2.2. Composite DLA Spectrum Calculation

To compute a stacked DLA absorption spectrum, we start by shifting each quasar spectrum to the DLA rest-frame, rebinning now into a pixel width of 0.3 \AA to obtain better sampling. We also discard pixels affected by skylines, and then divide by the previously computed mean quasar spectrum shifted to the same DLA rest-frame, obtaining the transmission at the rebinned pixel i of the quasar spectrum k ,

$$F_{ik} = \frac{f_{ik}/n_k}{\bar{f}_{ik}}, \quad (5)$$

where \bar{f}_{ik} now has the subindex k labeling each DLA only because the mean continuum \bar{f}_i has been shifted and rebinned on the DLA rest-frame. By means of error propagation, uncertainties are normalized and rebinned in the same way to obtain the error, E_{ik} , of the transmission spectrum of each DLA, F_{ik} . The final composite spectrum and its error is again

obtained from a weighted mean,

$$\bar{F}_i = \frac{\sum_k F_{ik} w_k}{\sum_k w_k}, \quad \bar{E}_i^{-2} = \frac{\sum_k E_{ik}^{-2} w_k}{\sum_k w_k}. \quad (6)$$

We set the weight w_k to be the same as in Equation (3), with the same value of $\sigma = 0.1$. This value does not really have to be the same for computing the mean quasar continuum and the mean DLA transmission spectrum; in general, we could choose a higher σ for stacking the DLA transmission because we need to take into account the intrinsic variability of the DLA metal lines as well. As we did for the case of the continuum, we have tested that increasing to $\sigma = 0.2$ does not substantially alter the results presented below; the two spectra have visually the same appearance.

The composite DLA transmission spectrum obtained after these calculations for the total sample is denoted by the black line in Figure 4. The gray line in this figure indicates the fraction of DLA systems contributing to the estimated stacked spectrum at each rest-frame wavelength bin. This fraction is less than unity on both sides of the range considered because a fraction of the quasar spectra, depending on their redshift, do not extend along the entire observed wavelength. The mean of the Lyman series lines due to hydrogen and many metal lines of our sample of DLAs are clearly evident. However, there are also broad regions where the mean transmission deviates from unity, which are clearly not associated with the narrow DLA absorption lines. This deviation may be due to several effects: the spectra that contribute to a given wavelength for the quasar composite are not the same that contribute to a given wavelength in the DLA composite, thus the quasar continuum is not entirely cancelled out. In addition, the $\text{Ly}\alpha$ forest causes an absorption both in the mean quasar spectrum and in the estimated transmission spectrum of each DLA, which does not exactly cancel when dividing by the mean quasar spectrum due to the redshift evolution of the $\text{Ly}\alpha$ forest. In the next subsection, we assess and apply several corrections for these

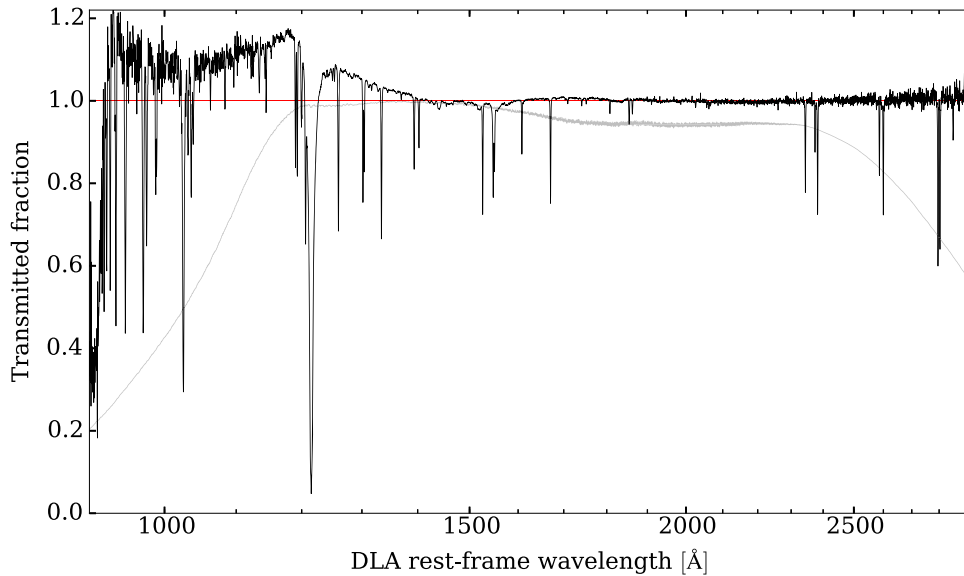


Figure 4. Composite DLA transmission spectrum computed for the total sample. The gray line indicates the fraction of the spectra used from the total sample contributing to the stacking at each wavelength pixel. The horizontal red line denotes the value unity for the transmission. The wavelength scale is logarithmically spaced.

effects to obtain a better quasar continuum and composite spectrum for the two samples.

The mean metal line equivalent widths that we will obtain in this paper, which vary with column density and redshift, depend on the selection of our sample. In addition, some fraction of the DLAs may be false and result from a concentration of Ly α forest lines that, in noisy spectra, may look like a DLA, while others may have large errors in redshift. This should cause a reduction of the mean equivalent widths measured in our stacked spectra, implying that our results may be sensitive to our adopted cut in the C/N and the way we choose to weight the contribution of DLAs depending on the S/N from Equation (3). We have tested the effect of eliminating the weights when calculating the composite spectrum (keeping the same sample of DLAs that we use after our cuts), which results in a very similar continuum, but substantially weaker metal absorption lines, with equivalent widths reduced typically by $\sim 30\%$. We believe most of this reduction is due to the fraction of false DLAs in the lowest S/N spectra, together with increased errors in redshift which wash out the metal lines in the stacked spectrum. Some of this reduction may also be due to a lower mean column density and higher mean redshift of the unweighted sample: The mean column density drops from from $\log(\bar{N}_{\text{H I}}/\text{cm}^{-2}) = 20.49\text{--}20.47$, and the mean redshift increases from $\bar{z} = 2.59\text{--}2.68$, when eliminating the weights, but as we shall see in our results (Figures 11 and 12), this accounts for only a small part of the reduction in mean equivalent widths when removing the weights.

However, by maintaining the weights, the contribution of false DLAs in low S/N spectra should be greatly reduced, and our systematic underestimate of the metal lines' mean equivalent widths should be much less than 30%. We have tested this by examining variations with the minimum threshold in C/N to accept DLAs in our sample. We find that the median relative increase of equivalent widths of metal lines analyzed in this paper is 2.5%, 3.7%, and 5% as the minimum C/N is raised to 3, 4, and 5, respectively. These fractional variations are, we believe, a fair estimate of our systematic errors caused

by impurity and large redshift errors in our DLA sample. Again, part of this increasing mean equivalent width with C/N may be caused by an increasing mean column density and decreasing redshift with C/N. In any case, this suggests that our weighting scheme is useful to reduce the effect of impurity in the DLA catalog, and that the remaining systematic reduction of mean equivalent widths is at the level of $\sim 5\%$.

For illustrative purposes, we have created two movies displaying the evolution of the mean quasar and composite DLA spectra as the number of stacked objects is increased. The two movies are publicly available and can be found, together with a brief description of the calculations, at <https://github.com/lluism>.

2.3. Corrections on the Continuum Spectrum

We now present the corrections that we apply to improve our first version of the transmission spectrum in Figure 4. Briefly, these corrections consist of detecting and removing bad pixels, correcting for the mean Ly α forest absorption, and correcting for the average effect of the DLA lines on the continuum spectrum. In addition, we describe the procedure applied to spectra where Ly β absorptions can be mistaken for Ly α . All these corrections, described in detail below, are applied equally for the total and metal samples.

2.3.1. Detection and Removal of Outliers

A variety of effects, e.g., cosmic rays, may cause large deviations of the flux in a few pixels from the correct values that clearly set them as outliers from the normal noise distribution. We prefer to eliminate these outliers, rather than working with median values which reduce the sensitivity to outliers, because we want to obtain mean equivalent widths in the end, and a relation of median to mean values would be model-dependent. Outliers cannot be eliminated by simply setting a maximum noise deviation of the transmission from the expected range of zero to unity, because the intrinsic variability of the quasar spectra can be large, implying that a more generous transmission range should be allowed.

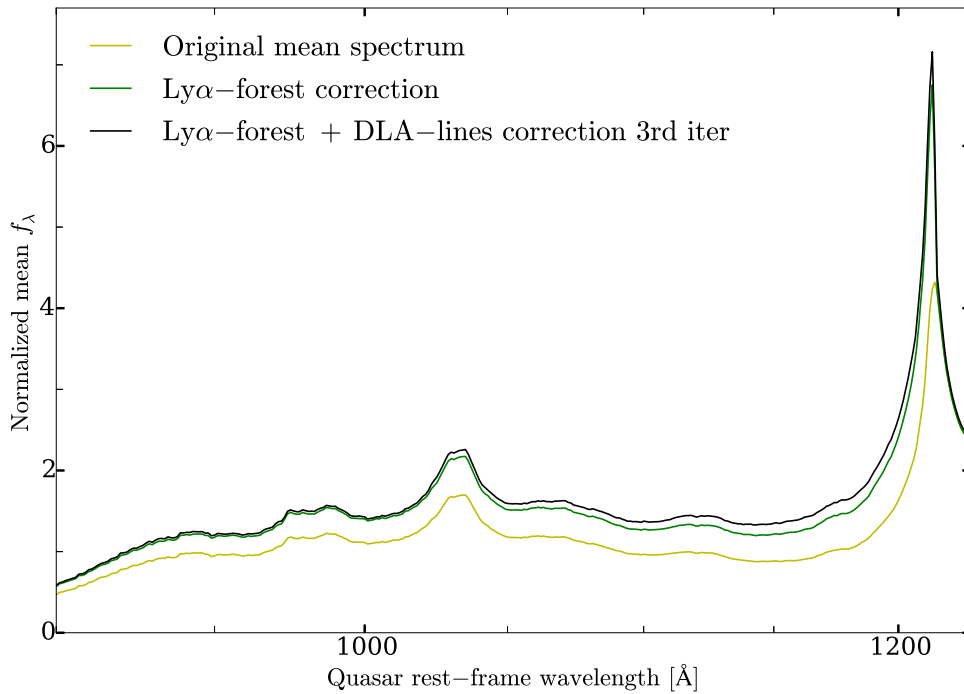


Figure 5. Original mean quasar spectrum before corrections (yellow), after correcting for Ly α forest absorption (dark green), and after the third iteration of the correction for DLA absorption lines (black). Modifications redward of the Ly α emission line are small, so only the Ly α forest region is shown here.

Therefore, for the purpose of eliminating outliers, we first obtain a fitted continuum, C_{ik} , to the transmission F_{ik} computed previously for each quasar. The detailed method we use to fit this continuum is described below in Section 3.1; essentially, C_{ik} is a smoothed version of F_{ik} computed once the regions of the expected metal lines of the DLA have been excluded. We then eliminate all pixels with a transmission F_{ik} that is outside the interval $[C_{ik} - 2 - 3 E_{ik}, C_{ik} + 2 + 3 E_{ik}]$, where E_{ik} is the transmission uncertainty in each pixel defined after Equation (5). This is a generously broad range, which allows for an uncertainty in the pixel flux of three times the estimated standard deviation E_{ik} , and adds an extra variation of twice the normalized mean quasar spectrum. Despite this broad range, it still excludes the most important outliers without eliminating any pixels that are not obviously bad. After the outliers are eliminated, we recalculate a new mean quasar continuum and a new stacked DLA absorption spectrum, which we adopt as the new composite spectrum in our analysis.

2.3.2. Mean Absorption of the Ly α Forest

The Ly α forest causes a systematic, redshift-dependent flux decrement blueward of the Ly α emission line of the quasar. The redshift evolution of this decrement means that, if it is not corrected, its mean value at a certain wavelength in the DLA rest-frame in our composite absorption spectrum is generally not equal to the mean value of the decrement in the mean quasar spectrum that was used to obtain the transmission from the observed flux, leaving a residual effect. This residual effect consists of an increase of the transmission in the DLA composite spectrum blueward of the Ly α feature, more important for longer wavelengths.

We use the fit obtained by Faucher-Giguère et al. (2008) for the mean fractional transmission as a function of redshift,

$$F_{\alpha}(z) = \exp[-0.0018(1+z)^{3.92}]. \quad (7)$$

We divide the normalized flux, f_{ij}/n_j in Equation (4), in the spectrum of each quasar by $F_{\alpha}(z)$ at the redshift $z = \lambda_{\text{obs}}/\lambda_{\alpha} - 1$ (where $\lambda_{\alpha} = 1215.67 \text{ \AA}$), before stacking to obtain the mean quasar spectrum. We then divide again each spectrum containing a DLA by F_{α} at the same redshift, before dividing by the mean quasar spectrum in Equation (5). The net correction does not completely cancel, and depends on the probability distribution of the DLA and quasar redshifts in our catalog, which is sensitive to selection effects reflecting the DLA detection probability.

Figure 5 displays the impact of the correction for the Ly α forest transmission on the mean quasar continuum. The original spectrum (yellow line) is raised by $\sim 20\%$ after this correction (green line), reflecting the mean decrement at the mean redshift of our quasar sample. The change of the composite DLA spectrum after applying this correction is presented in Figure 6 (yellow and green lines for the original and corrected spectra, respectively). Both figures display the result for the total sample.

Equation (7) includes the effect of the Ly α forest only. Metal lines are believed to increase the decrement by $\sim 5\%$ of that due to Ly α (Faucher-Giguère et al. 2008). We neglect these metal lines, and we also do not include the additional corrections for the forests of Ly β and higher-order hydrogen lines, although we do correct for the effect of all the lines associated with the DLAs themselves that are stacked in the final composite spectrum, as we describe below.

2.3.3. Effect of the DLA Absorption Lines

When we compute the mean quasar continuum, there is a mean incidence rate of hydrogen and metal lines of DLAs that are present in each quasar spectrum and contribute to lower the measured flux. This average flux decrement caused by the DLA lines is larger than in a random sample of quasars because we use only the quasars in the DLA catalog to obtain our mean

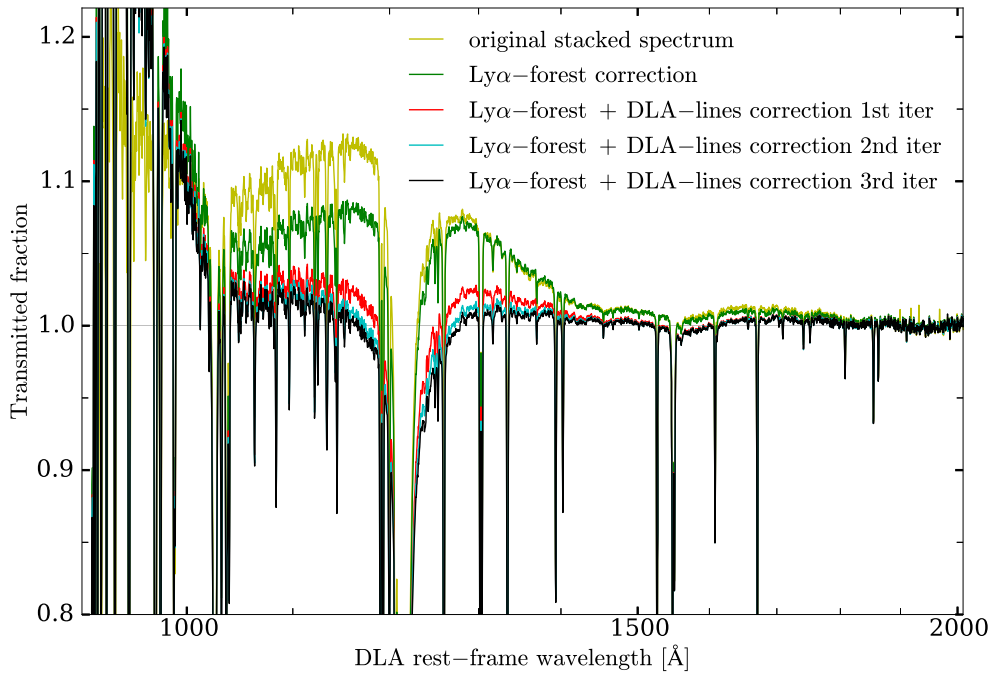


Figure 6. Stacked DLA spectrum before and after corrections. The original stacked spectrum, with some outliers causing deviations in a few pixels near 1900 Å and in the Ly α forest region, is shown in yellow. The spectrum after correcting for the Ly α forest mean a decrement and the removal of outliers is in dark green. The DLA lines correction is included in the red, blue, and black lines, after the first, second, and third iteration, respectively.

quasar spectrum where, by construction, each quasar spectrum contains at least one DLA. We now describe the procedure to correct for the presence of these DLA lines, which is applied both to the total and metal samples.

For each DLA in the catalog, we redo the quasar continuum spectrum calculation after modifying the flux values in pixels that are located within predefined windows around each of the expected DLA absorption lines. We also remove some of these pixels where the DLA absorption is strongest. We account for all the DLA metal absorption lines listed in Appendix A, in Tables 4 and 5, as well as for the blended lines listed in Table 1. We include in addition the hydrogen Lyman transitions from Ly α up to $n = 9$, covering the range between 920 and 3000 Å. The wavelength windows around each line center used for this correction are the same as those used for the computation of the equivalent width of the metal lines, described in detail in Section 3.1 below.

For each DLA absorption line, the flux in each pixel within its window is corrected as

$$f_L = \frac{f_{\text{QSO}}}{\bar{F}_D}, \quad (8)$$

where f_L is the corrected flux, f_{QSO} is the observed flux before correction in the quasar rest-frame at redshift z_q , and \bar{F}_D is the transmission in the mean DLA composite spectrum, after shifting to the quasar rest-frame by multiplying the wavelength by $(1 + z_{\text{DLA}})/(1 + z_q)$. The DLA composite spectrum is rebinned in order to match the quasar rest-frame, in the same way as in Section 2.2 when computing the mean quasar spectrum. This correction is applied only within each DLA absorption line window, when $1.0 > \bar{F}_D \geq 0.4$. For the strongest DLA lines, pixels where the DLA mean transmission is $\bar{F}_D < 0.4$ in the composite spectrum are removed instead of being corrected, and not taken into account for calculating the

improved quasar continuum. We adopted this approach to avoid excessive noise from the regions that are highly absorbed. Small variations for the threshold value 0.4 do not significantly change our results. This correction is applied without considering detecting any DLA line in the individual spectra, to correct for their mean expected absorption.

The new mean quasar continuum is used to recalculate the DLA composite spectrum. We can now iterate the same procedure, since the DLA composite spectrum is needed to compute the correction to each quasar continuum, until there is no significant improvement. This convergence is reached after three iterations. The black line in Figure 5 shows how the mean quasar continuum is further modified by these DLA lines in the region of the Ly α forest (this is mostly the effect of the DLA Ly α line), and Figure 6 indicates how the DLA composite spectrum is improved after the first, second, and third iterations (red, blue, and black lines, respectively; the spectrum is displayed only at $\lambda < 2000$ Å; at longer wavelengths the corrections to the continuum are very small). A clear improvement is seen after the first iteration (red line), in the sense that the continuum between the DLA metal lines moves closer to unity over most of the regions, but a smaller improvement is achieved with subsequent iterations.

Despite the improvements that result from these corrections, Figure 6 demonstrates that the continuum still deviates slightly from unity due to other uncorrected systematics. One contribution is probably the proximity effect, which accounts for the fact that the Ly α forest near the quasar redshift has a lower mean decrement than far from the quasar redshift. There is also a small rise of the continuum above unity in the region longward of the C IV line, which may be partly caused by the forest of C IV lines associated with the Ly α forest and Lyman limit systems. Further improving our continuum model would clearly require more detailed work to correct for these effects and other systematics that are likely present. We decided to

stop here and to use a simple method to flexibly fit the continuum between the DLA lines in the next section.

The correction involving the effect of the DLA absorption lines assumes that there is only one DLA in each quasar spectrum. For each DLA in the catalog, the quasar spectrum is corrected for the presence of only that DLA, ignoring the possible presence of other DLAs in the same spectrum. A more accurate procedure would take into account all the detected DLAs in each quasar spectrum. As mentioned above, $\sim 80\%$ of the spectra in both samples contain only one DLA, so we expect spectra with more than one DLA to produce a small effect on the mean quasar continuum.

Finally, in order to compare our method for correcting the effect of the DLA lines, we adopt a different approach. We calculate the mean quasar spectrum, now using all the spectra in the DR12 quasar catalog from BOSS that do not contain DLAs. After our cuts, this results in the use of $\sim 210,000$ quasar spectra. The continuum of this mean quasar spectrum overlaps with our previously computed mean spectrum, except in the Ly α forest region. The difference between the two corresponds to a $\sim 10\%$ increase of the flux in the forest for the sample without DLAs. Our correction (black line in Figure 5) increases the flux depending on wavelength, from $\sim 5\%$ at $\sim 1050 \text{ \AA}$ to $\sim 10\%$ at $\sim 1150 \text{ \AA}$. Therefore, our correction might simply account for a fraction of the total DLA effect but, because of other possible contributions to the observed difference (e.g., the strength of the emission lines are different in the two samples), we consider our original approach for further calculations. This will not affect our results because of the use of the additional continuum fit to the final composite spectrum.

2.3.4. Contamination by DLA Ly β Lines Mistaken for Ly α

When we first obtained the DLA composite spectrum, we noticed the presence of a few regions with unexplained anomalous absorption features. These can be seen in Figure 4, where the spectrum for the total sample has strange spectral features, for example, near 1440 or 1520 \AA (just to the left of the Si II line), which do not appear in the spectrum of the metal sample. The source of these features is that some Ly β absorption lines are incorrectly identified as DLA Ly α lines in the DLA catalog. This error produces spurious absorption features in the stacked spectrum and other undesired effects (the features are not present in the metal sample because the DLAs identified at a wrong redshift obviously do not yield any metal line detections). To avoid this problem, we have removed all the DLA spectra with a redshift $(1 + z_{\text{DLA}}) \leq 27/32(1 + z_q)$, ensuring that the detected Ly α lines cannot possibly be a Ly β line of a higher-redshift DLA. The amplitude of the fictitious features caused by these DLAs indicates that only $\sim 10\%$ of them are incorrect identifications of a Ly β line, but we have not further attempted to separate these mistaken detections in order to avoid any other selection effects in our total sample. This criterion reduces the number of DLAs in our total sample to $26,931$, and to $10,766$ in our metal sample, to which the whole analysis described above has been applied. In the rest of the paper, we analyze the results obtained for these restricted catalogs.

3. Analysis of the Composite DLA Spectrum

We measure the mean equivalent width of metal lines detected in the stacked DLA absorption spectra below. We also

divide the two DLA samples into five column density bins to assess the dependence of these mean equivalent widths on the hydrogen column density, $N_{\text{H I}}$, in Section 4. The results are tabulated in Table 1, and Tables 4–9 in Appendix A.

Figures 7 and 8 present an expanded version of the final composite absorption spectrum of DLAs, for the total and the metal sample, respectively, with labels denoting the detected absorption lines. Absorption lines in the metal sample (Figure 8) are usually stronger and present a sharper profile than those in the total sample, allowing for more detections of weak absorption features despite the noise. This is simply because the metal sample is selected to include only DLAs with individually detected metal lines, so DLAs of low metallicity and/or low C/N spectra are usually excluded, reducing the noise in the final stacked spectrum.

The Ly α absorption feature in Figure 7 does not present a broad, flat region with null flux at the position of the line center as observed in single systems. This effect has two causes. First, there may be some zero-flux error with a mean transmission of ~ 0.01 that is systematically added to all the spectra. Second, the DLA sample is not totally pure, and there may be a few percent of the absorbers cataloged as DLAs that are actually arising as a combination of lower column density absorbers and spectral noise, contributing also a residual flux at the Ly α line profile of the stacked spectrum. For the metal sample, where the percentage of false DLAs should be much smaller, there is a flatter bottom of the DLA mean profile that is consistent with the width of the damped profile expected for the lowest column densities present in the catalog. This may also affect the metal lines: as mentioned earlier, our equivalent widths may be systematically underestimated because of a fraction of DLAs in the catalog that are not real or have large redshift errors. The zero-flux error may cause an additional underestimation of metal line equivalent widths, but the relative error should be similar to the fraction of zero flux present at the bottom of the Ly α line in Figures 7 and 8, which is only a few percent. We ignore these systematic errors in this paper; future improvements on this work should use mocks of the Ly α spectra in BOSS to correct for the fraction of false DLAs in our catalog, as well as the zero-flux error (see, e.g., Bautista et al. 2015).

We detect transitions of elements rarely seen in DLAs, such as Ti II, C II*, P II, Co II, Ar I, and several lines of C I, a species that is associated with H₂ (Srianand et al. 2005; Ledoux et al. 2015). We also observe several high-ionization lines, including N V, O VI, and S IV, which are extremely difficult to detect in individual spectra; in fact, N V and S IV have been detected only in a few DLAs, and when they are detected they are hard to separate unambiguously from the Lyman forest lines, particularly for S IV and O VI lines which are always blended with the forest (Fox et al. 2007b; Lehner et al. 2008, 2014). Here, we will analyze a total of 42 low-ionization lines, 8 high-ionization lines, and 13 absorption features that are the result of blends of several metal lines that are unresolved at the BOSS resolution. These lines are listed in Tables 4 and 5 in Appendix A and in Table 1. The uncertainties in their equivalent widths indicate that not all of them are detected at a high confidence level, particularly in the total sample. We now describe how the equivalent widths and uncertainties are evaluated.

3.1. Line Windows and Fitted Continuum

We select the set of lines described above to measure their equivalent widths. These features were chosen simply from their visual appearance to have a detection in our composite spectrum of the metal sample. These lines, in addition to the first eight hydrogen Lyman transitions (all of them with wavelengths within the range $920 \text{ \AA} < \lambda < 3000 \text{ \AA}$), are the ones used for the computation of the fitted continuum described below, as well as for the quasar continuum correction presented in Section 2.3.3.

Before equivalent widths can be measured, a set of windows around each line need to be defined over which the absorption fraction is to be computed. We generally choose a total window width of 7 \AA centered in the DLA rest-frame line center, which is wide enough to include all appreciable absorption for any unblended line. The line profiles have all nearly the same widths because they are unresolved, thus the equivalent width is, in practice, the only information that can be obtained from these line profiles. We have tested that the measured equivalent widths do not vary significantly under small variations of the window widths. The Ly α and Ly β transitions are treated differently because they have a clearly resolved mean absorption profile. We use halfwidths of 40 \AA and 5 \AA for their windows, respectively. In addition, whenever several lines have overlapping windows, we define broader windows which include all the individual windows of the lines in the blend (this is described in detail below in Section 3.3).

Before measuring the equivalent widths, we perform a final continuum fitting of the DLA composite spectrum to remove the residual variations left after the corrections discussed in the previous section. This method is similar to that applied by, e.g., Pieri et al. (2014), Sánchez-Ramírez et al. (2016), and Berg et al. (2016). We proceed in the following manner: for each pixel outside any of the line windows described above, we compute the mean value of the transmission within a 10 \AA width window centered on the pixel, excluding any pixels that are inside the absorption line windows (pixels belonging to skylines or outliers have already been removed and do not contribute to the fitting calculation). We then compute a standard cubic-spline fit over the range $900\text{--}3100 \text{ \AA}$ in the DLA rest-frame, using only one (starting from the first) out of every 15 of these mean values for the transmission (pixels in the DLA stacked spectrum have widths of 0.3 \AA , therefore the averaging of the transmission is done over about 33 pixels, so all pixels contribute to the determination of this final continuum). The 15 pixel separation between successive points used for the spline fitting corresponds to a distance of 4.5 \AA when there are no absorption lines or other effects which can discard pixels in between. We have checked that using 20 or 10 pixels instead of 15 makes no substantial difference. This approach produces a smoother continuum compared to using the averaged flux in all pixels, which produces undesired “waves” over the regions of the absorption lines.

Despite averaging the continuum in 10 \AA width windows, this new fitted continuum is still affected by the pixel noise near the window edges. The statistical error that this effect introduces is accounted for with the bootstrap method described in Section 3.4, but any other possible systematic effects on equivalent widths introduced by our method are not included in our errors. The resulting cubic-spline fit is used as

the new continuum to calculate equivalent widths and limits on the detection of outliers described in Section 2.3.1.

The equivalent width calculation for the case of lines within the Ly α window needs special attention. We determine a continuum that includes the Ly α absorption, with the goal of being able to measure the equivalent widths of metal lines that are blended with the Ly α line. For the purpose of computing the continuum in the Ly α line region, we ignore the previously defined metal line windows, and select instead the following windows (in units of \AA) that appear to be free of absorption by metal lines in both the total and metal samples stacked spectra: [1175.67–1188], [1196–1198], [1202–1205], [1209–1235], [1246–1248], [1255–1255.67]. These intervals are selected as a compromise for maximizing the number of points used for the continuum and minimizing points near the metal absorption lines. We then use linear interpolation to connect all the pixels throughout this region, connecting also linearly the points at the window edges. This approach yields our fitted continuum over the region [1175.67–1255.67 \AA]. Outside this range, we use the previously described cubic-spline-fitted continuum.

The final fitted continuum is displayed as the red line in Figure 9 over the $1000\text{--}1700 \text{ \AA}$ range. Green points are used to fit the linear continuum in the Ly α line window.

We stress that our stacked Ly α line does not have the shape of a single Voigt profile because it arises from a superposition of DLAs with different column densities. We have not attempted to fit the observed profile by modeling it with a column density distribution for our sample, in view of the zero flux error and other complicated effects (e.g., the cross-correlation of DLAs and the Ly α forest). Ignoring this statement and forcing a fit to a single Voigt profile, we obtain a column density $\log(N_{\text{H I}}/\text{cm}^{-2}) = 20.49$, which coincides with the mean column density of our sample (with the weights applied in our stacked spectrum) as measured from the individual systems. In future work, it should be interesting to fit the mean profiles of all the Lyman series lines, which should contain valuable information on the distribution of velocity dispersions in the DLA systems.

3.2. Equivalent Width Estimator

We next fit a Gaussian optical depth line profile to each metal line within its window,

$$F = C_f \exp \left[-b \exp \left(\frac{-(\lambda - \lambda_0)^2}{2a^2} \right) \right], \quad (9)$$

where b and a are two free parameters, λ is the pixel wavelength in the DLA rest-frame, λ_0 is fixed to the known central wavelength of the line, and C_f is the value of the fitted continuum in each pixel. We perform a standard least-squares fit to the measured F in the pixels of each line window with the two free parameters a and b .

In practice, the parameter a in Equation (9), reflecting the width of the lines, is essentially determined by the spectrograph resolution of BOSS, except in a few cases of blended lines. The BOSS resolution depends smoothly on the observed wavelength, but once this smooth variation is taken into account, the resolution should not vary among different metal lines. Therefore, the accuracy of the fit to the line equivalent widths should improve if we impose a fixed width

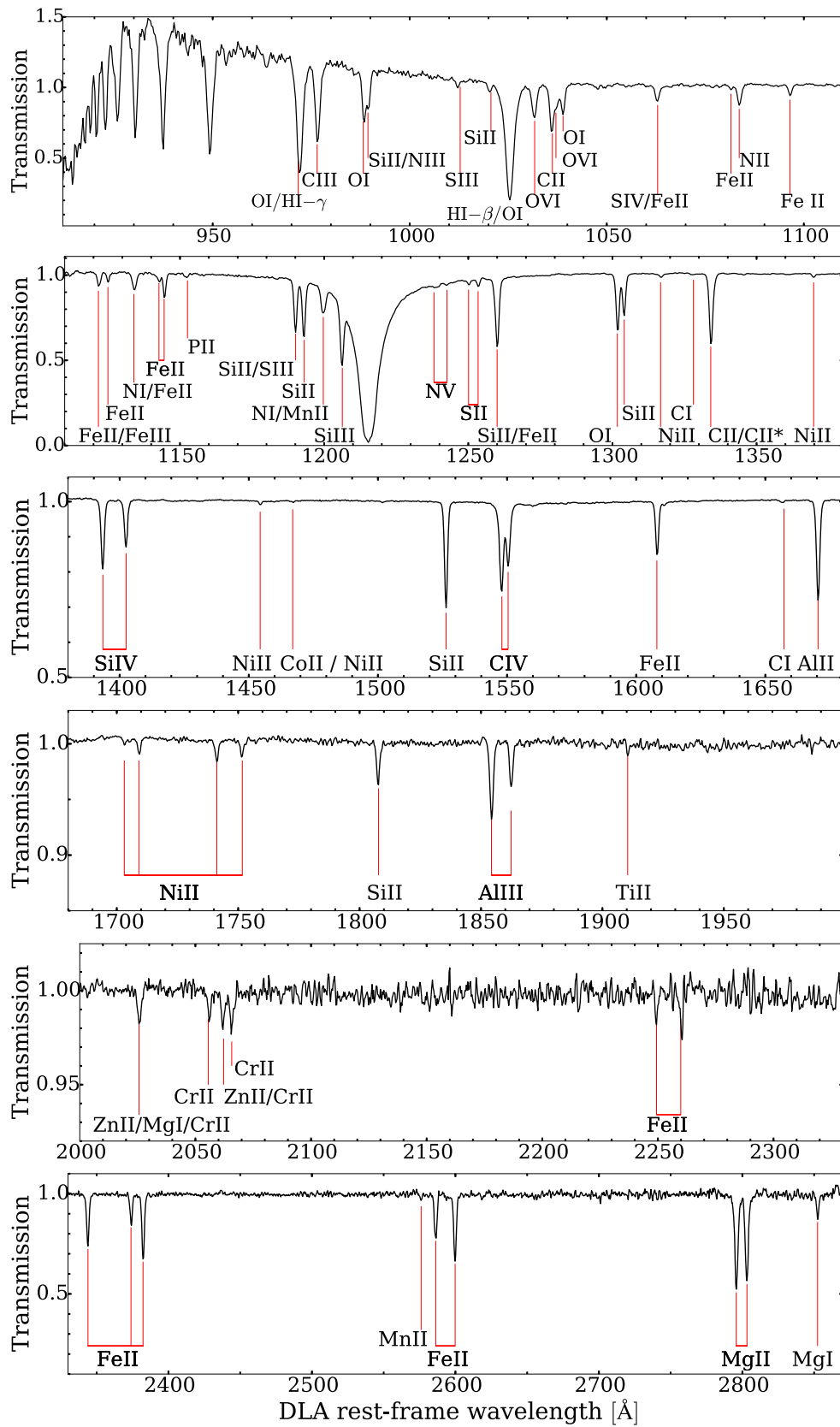


Figure 7. Expanded version of the final composite DLA transmission spectrum for the total sample. Labels under the red vertical lines denote the species. Only lines with wavelengths longer than 970 Å are shown. Lines at shorter wavelengths are severely blended with the Ly α forest, and the only features that are clearly visible are the higher-order Lyman series of hydrogen. Each panel has a different scaling for the transmission, selected to enhance the visibility of the lines.

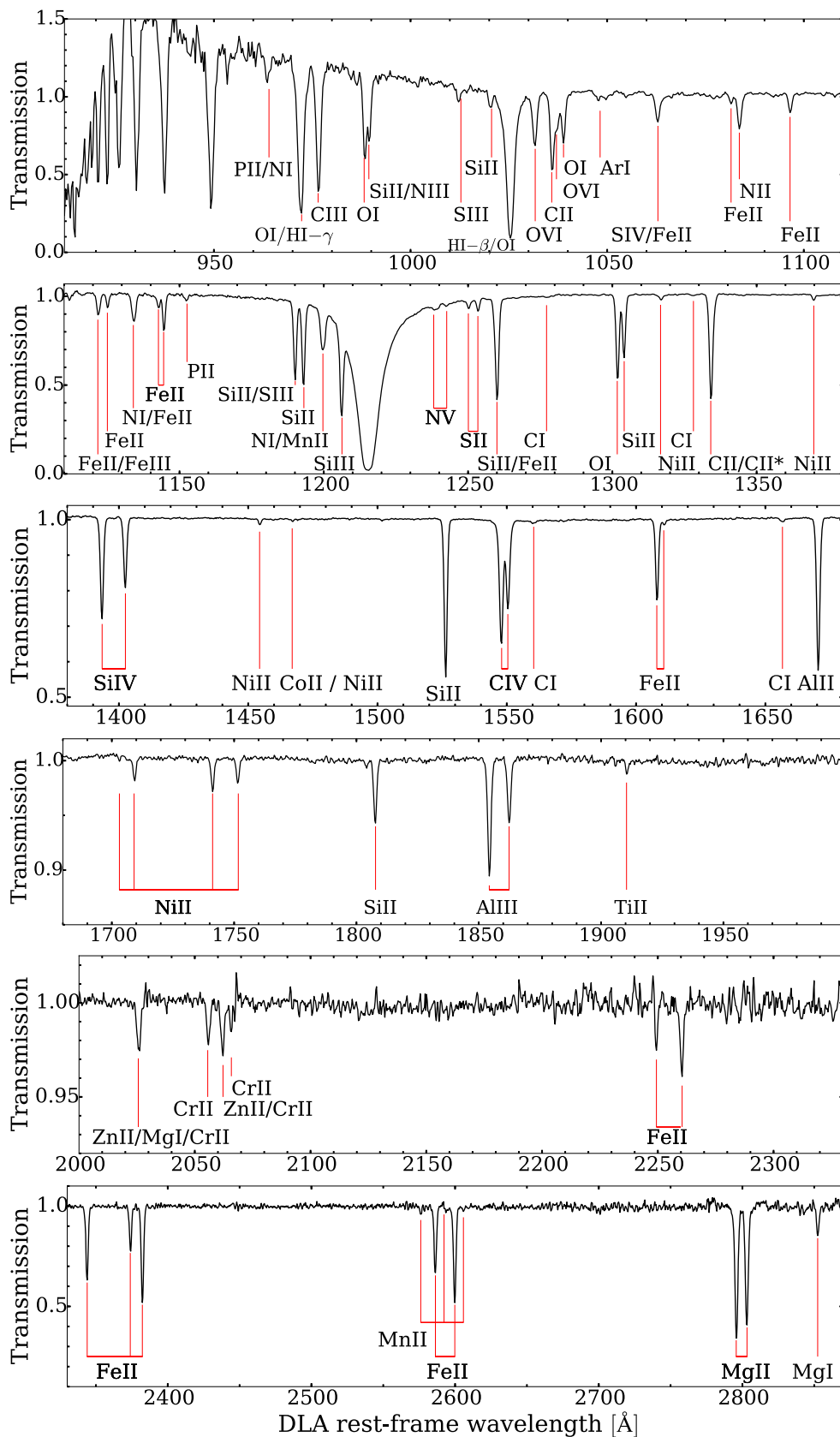


Figure 8. Same as Figure 7, here for the metal sample.

parameter a on the lines, assuming that the width is not affected by variable levels of saturation of the absorption lines. To examine the variation of a with wavelength, Figure 10 displays

the values of a obtained for all the metal lines, as a function of their rest-frame wavelength, for the case of the total sample. Yellow dots indicate blended lines, or lines that are apparently

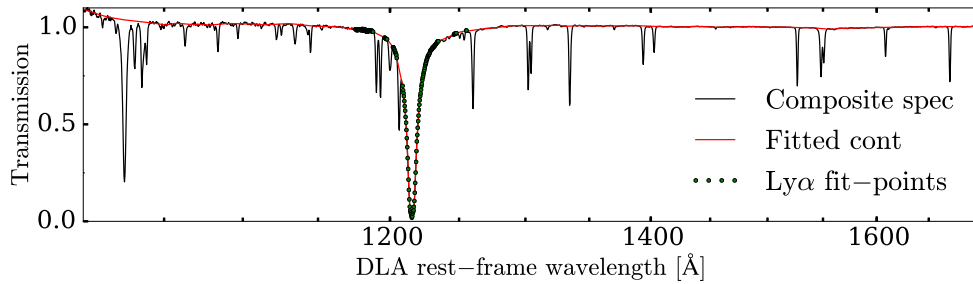


Figure 9. Fitted continuum (red line) used for the calculation of the rest-wavelength equivalent width of metal lines and detection of outliers over the stacked spectrum of the total sample (black line), shown over the range 1000–1700 Å. The pixels used for the linear fit in the Ly α line region are denoted as green circles.

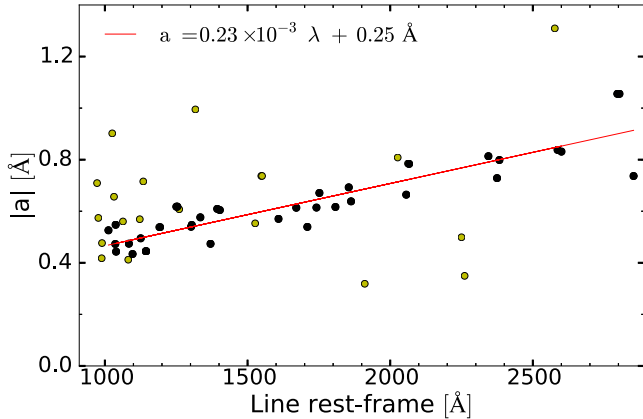


Figure 10. Fitted values of the a parameter for each absorption line in the stacked spectrum for the total sample. Black data points are used to compute the linear regression, shown as the red line. Yellow points are considered outliers, affected by blended lines or low S/N, and not used. The values for the a parameter can be considered as an estimation of the spectrograph resolution assuming that the lines are unresolved.

very weak and strongly affected by noise, so that they are deemed likely to present deviations of their width from any smooth dependence. In cases of lines forming part of an atomic doublet, they are jointly fitted and are required to have the same value of a , but different values of b .

It is apparent from Figure 10 that there is a smooth increase of the width parameter a with wavelength, with a small scatter for the black points corresponding to lines that are not affected by blends or a very weak S/N. There is no evidence for any difference in the width between low-ionization and high-ionization lines, which might have indicated a different contribution from a physical velocity dispersion to the measured widths. We fit a linear regression to the values of a as a function of wavelength using the black points only (with each point weighted equally), and we obtain the result

$$a = 0.23 \times 10^{-3} \lambda + 0.25 \text{ \AA}, \quad (10)$$

shown as the red line in Figure 10. The same procedure for the metal sample yields a linear regression of the form

$$a = 0.25 \times 10^{-3} \lambda + 0.18 \text{ \AA}. \quad (11)$$

These equations can be considered as an estimation of the spectrograph resolution assuming that the lines are unresolved. The difference between the two samples is mostly due to the better accuracy of the redshifts in the metal sample, which makes the lines appear slightly narrower. Having tested that the deviations of the a parameter from this linear regression arise

from noise and not from physical differences among the lines, we now repeat the fits to each line with Equation (9), but keeping a fixed to these linear regressions and fitting only the b parameter. We then integrate the area below the continuum represented by the function in Equation (9) to compute the corresponding equivalent width for each line.

In some cases, a group of absorption lines are close enough for their wings to overlap, but the absorption maxima are still well separated. In this case, we use a common window including the windows of all the blended lines and we measure their equivalent widths in a single joint fit. The optical depths modeled as Gaussians are added or, equivalently, the transmissions from each line are multiplied, to obtain the total profile. The equivalent widths of these lines, marked with a superscript denoting overlap, are listed together with all the other lines for the total and metal samples in Tables 4 and 5 in Appendix A. Their errors are computed using the bootstrap method described in Section 3.4.

Figures 17 and 18 in Appendix B present the fit for all the absorption features analyzed in the total sample. These figures display the line window, the continuum and the fitted absorption profile. In cases of overlap, each individual line is indicated separately in addition to the total absorption profile. Below, we discuss the case for lines that are strongly blended.

3.3. Strongly Blended Absorption Lines

There are several blended absorption lines that do not present separate absorption maxima. We designate these groups “strongly blended lines.” These groups and their individual blended lines are listed in Table 1.

We use the same procedure described above to perform a joint fit to all the lines belonging to a blend: we fix all central wavelengths and Gaussian widths, and only allow the amplitude of each line to vary. Any lines that may be part of a blend with an equivalent width expected to contribute less than 1% to the total equivalent width are ignored. In these fits, the only reliable measurement is usually the total equivalent width of each blended group, which is listed in the first column with its bootstrap uncertainty. The individual equivalent widths of each line (with wavelengths and oscillator strengths listed in the second and third columns, respectively), with highly correlated and larger errors, are listed in the fourth column. The fifth column reports a modeled estimate of individual equivalent widths, according to a theoretical model, described below in Section 6, that uses measurements of other absorption lines of the same species. Finally, the sixth column gives an inferred equivalent width for one of the blended lines once the modeled lines are taken into account, and in cases where all the

Table 1
Mean Rest Equivalent Widths of Strongly Blended Metal Absorption Lines in the Total Sample

| Total W | Lines | f | Fitted W | Model W | Inferred W |
|-------------------|--------------------------|--------|-------------------|-----------------------|-------------------|
| 0.393 ± 0.019 | O I $\lambda 988.58$ | 0.0005 | 0.000 ± 0.118 | 0.034 ± 0.002 | 0.524 ± 0.009 |
| | O I $\lambda 988.65$ | 0.008 | 0.283 ± 0.135 | 0.200 ± 0.004 | |
| | O I $\lambda 988.77$ | 0.047 | 0.131 ± 0.073 | 0.330 ± 0.004 | |
| 0.271 ± 0.021 | N III $\lambda 989.80$ | 0.123 | 0.089 ± 0.108 | 0.275 ± 0.002 | ... |
| | Si II $\lambda 989.87$ | 0.171 | 0.191 ± 0.110 | | |
| 0.157 ± 0.019 | Fe II $\lambda 1062.15$ | 0.003 | 0.004 ± 0.012 | 0.0115 ± 0.0004 | 0.024 ± 0.012 |
| | S IV $\lambda 1062.66$ | 0.049 | 0.020 ± 0.011 | | |
| | Fe II $\lambda 1063.18$ | 0.055 | 0.122 ± 0.010 | | |
| | Fe II $\lambda 1063.97$ | 0.005 | 0.013 ± 0.010 | | |
| 0.115 ± 0.009 | Fe II $\lambda 1121.97$ | 0.029 | 0.065 ± 0.007 | 0.077 ± 0.002 | 0.042 ± 0.008 |
| | Fe III $\lambda 1122.53$ | 0.054 | 0.051 ± 0.007 | | |
| 0.178 ± 0.014 | Fe II $\lambda 1133.67$ | 0.006 | 0.031 ± 0.011 | 0.0203 ± 0.0007 | 0.133 ± 0.010 |
| | N I $\lambda 1134.17$ | 0.015 | 0.013 ± 0.020 | | |
| | N I $\lambda 1134.41$ | 0.029 | 0.075 ± 0.020 | | |
| | N I $\lambda 1134.98$ | 0.042 | 0.063 ± 0.011 | | |
| 0.071 ± 0.010 | Fe II $\lambda 1142.36$ | 0.004 | 0.023 ± 0.006 | 0.0140 ± 0.0005 | 0.071 ± 0.004 |
| | Fe II $\lambda 1143.23$ | 0.019 | 0.048 ± 0.005 | | |
| 0.411 ± 0.006 | S III $\lambda 1190.21$ | 0.024 | 0.079 ± 0.015 | 0.056 ± 0.013 | 0.436 ± 0.006 |
| | Si II $\lambda 1190.42$ | 0.292 | 0.345 ± 0.012 | | |
| 0.296 ± 0.007 | N I $\lambda 1199.55$ | 0.133 | 0.135 ± 0.006 | 0.137 ± 0.005 | 0.293 ± 0.003 |
| | N I $\lambda 1200.22$ | 0.087 | 0.104 ± 0.008 | | |
| | N I $\lambda 1200.71$ | 0.043 | 0.063 ± 0.007 | | |
| 0.623 ± 0.008 | S II $\lambda 1259.52$ | 0.017 | 0.083 ± 0.006 | 0.095 ± 0.005 | 0.688 ± 0.008 |
| | Si II $\lambda 1260.42$ | 1.180 | 0.553 ± 0.006 | | |
| | Fe II $\lambda 1260.53$ | 0.024 | ... | | |
| 0.012 ± 0.007 | Ti II $\lambda 1910.61$ | 0.104 | 0.000 ± 0.004 | 0.006 ± 0.003 | 0.006 ± 0.003 |
| | Ti II $\lambda 1910.95$ | 0.098 | 0.012 ± 0.006 | | |
| 0.630 ± 0.007 | C II $\lambda 1334.53$ | 0.128 | 0.597 ± 0.006 | 0.597 ± 0.014 | 0.037 ± 0.005 |
| | C II* $\lambda 1335.71$ | 0.115 | 0.037 ± 0.005 | | |
| 0.035 ± 0.008 | Zn II $\lambda 2026.14$ | 0.501 | 0.033 ± 0.009 | 0.00030 ± 0.00009 | 0.025 ± 0.007 |
| | Cr II $\lambda 2026.27$ | 0.001 | 0.002 ± 0.009 | | |
| | Mg I $\lambda 2026.48$ | 0.113 | 0.000 ± 0.003 | | |
| 0.034 ± 0.007 | Cr II $\lambda 2062.23$ | 0.076 | 0.031 ± 0.008 | 0.022 ± 0.007 | 0.011 ± 0.007 |
| | Zn II $\lambda 2062.66$ | 0.246 | 0.003 ± 0.006 | | |

Note. First column: total measured equivalent width (in Å) for the absorption feature. Second column: lines contributing to each blend. Third column: oscillator strength of the contributing lines from Morton (2003). Fourth column: individual fitted equivalent widths. Fifth column: equivalent widths predicted from our model, using other absorption lines of the same species in Table 4. Sixth column: inferred total and individual equivalent widths fixing the modeled lines to the predicted equivalent widths from our model.

lines in a blend are modeled, it lists the inferred total equivalent width of the blend. These results will be discussed in detail in Section 6.3.

We wish to warn here, however, that the results for the fitted equivalent widths of blended lines in the fourth column are subject to an important systematic error: we are simply assuming that the transmission of the individual lines modeled with the profile in Equation (9) can be multiplied to fit the entire blend. This situation is actually not true because the absorbing components in each individual line are not

independent, but have a highly correlated velocity structure in each DLA. When the blended lines are very close together (for example, for the first blend in Table 1 for O I lines), the combined equivalent widths of the various lines may hardly increase in DLAs with very narrow lines, which are highly saturated even if the blended line at the BOSS resolution appears far from saturation, and may increase to some extent in DLAs with broader velocity profiles. It is impossible to make a reliable estimate of how the “fitted” equivalent widths of individual lines should be added to yield the total blend

equivalent width without a complete model of the absorbing subcomponents width distribution and velocity correlations. This effort would be much more ambitious than the simple model presented below in Section 6.1 for modeling single line equivalent widths in terms of mean column densities. We therefore choose to use the simple assumption of multiplying transmissions of all the individual lines. This approach produces approximately correct results only for blends of lines that are sufficiently separated or weak that they do not have frequently overlapping absorbing components that are saturated at full resolution.

The fits to the blended absorption profile in these cases are also presented in Figures 17 and 18. Due to the systematic errors mentioned above, individual line profiles are not separately shown for these strongly blended lines.

3.4. Bootstrap Error Computation

The errors on the line equivalent widths cannot be obtained from the errors on the observed flux in individual pixels because they are often dominated by continuum uncertainties. We therefore use a bootstrap method: we randomly split our DLA sample (both the total and the metal one) into 100 subsets containing roughly the same number of DLA candidates. We then generate 1000 new samples by randomly selecting 100 of these subsets, allowing for repetition, and we recompute the composite spectrum, the continuum fit and the equivalent width calculations for each new sample. We use the same values of a (λ) that were obtained in Equations (10) and (11), and we obtain the errors from the standard deviation of each metal line equivalent width among the bootstrap samples.

4. Dependence of Equivalent Widths on $N_{\text{H I}}$

We now examine the dependence of the mean equivalent width of the metal lines on the property that can be best measured for each individual DLA: the hydrogen column density $N_{\text{H I}}$, which determines the damped profile of the hydrogen Ly α line. We divide the total and the metal samples into five intervals in $\log(N_{\text{H I}}/\text{cm}^{-2})$ chosen to contain a similar number of DLAs: [20.0–20.13], (20.13–20.30), (20.30–20.50), (20.50–20.80), (20.80–22.50]. The logarithms of the mean values of the column density in these ranges are 20.06, 20.22, 20.40, 20.65, and 21.13, respectively. For each interval, we redo the previous calculations: a composite spectrum of transmission fraction is obtained for the DLAs that have a column density in the specified range, the continuum is fitted, and equivalent widths of our list of metal lines with bootstrap errors are obtained. The a parameter in Equation (9) is kept fixed to the same values used for the entire sample, assuming that it is independent of $N_{\text{H I}}$. The bootstrap errors are computed as before, using only the DLAs in every bootstrap subset which are in the $N_{\text{H I}}$ bin of interest when doing the stacking. The bootstrap subsets are large enough to contain similar numbers of DLAs in each column density bin. Results for the mean equivalent widths are tabulated in Tables 6–9 in Appendix A, separately for low-ionization and high-ionization species, and for the total and metal samples. The intermediate species C III, Si III, Al III, and S III are included in the table of low-ionization species owing to the fact that the kinematic properties for these elements resemble those of low-ionization species (Wolfe et al. 2005).

The dependence of the mean equivalent widths on column density is presented in Figure 11. Several low-ionization species are shown in the top panels (total sample on the left, metal sample on the right). Points are connected with dotted lines to help visualize the trend with $N_{\text{H I}}$ for each species (they are slightly shifted horizontally from the true mean column density values specified previously to avoid overlapping errorbars). A general trend of increasing W with increasing $N_{\text{H I}}$ is apparent, as expected. If the mean metallicity and dust depletion in DLAs do not vary substantially with column density, hydrogen is mostly atomic, and the low-ionization species displayed in Figure 11 are the dominant ionization stage of the respective elements, then we expect the metal column densities to increase linearly with $N_{\text{H I}}$. This prediction, however, cannot be tested directly because a large fraction of lines may be saturated, and the degree of saturation depends on a complex distribution of velocity dispersion, metallicity, and multi-component structure of the absorption systems.

The bottom panels show the dependence of the mean equivalent widths on column density for three high-ionization species, Si IV, O VI, and C IV, in the total and metal samples (left and right panels, respectively), and for an intermediate species, Al III. We also present the behavior of the Fe II $\lambda 1608$ line for comparison (in soft gray). The total sample demonstrates that there is also an increase in the mean equivalent width with column density, in all cases. However, the increase is much smaller than for low-ionization lines. Over the column density range $20 < \log(N_{\text{H I}}/\text{cm}^{-2}) < 20.7$, the mean equivalent width of the C IV and Si IV lines increases by a factor ~ 1.25 , whereas the increase for relatively weak lines of low-ionization species in the top panels over the same range is a factor ~ 3 , and even the strongest low-ionization line, C II (which is most saturated), increases by a factor ~ 1.8 . The Al III line increases by a factor that is intermediate between the low-ionization and high-ionization cases.

The metal sample presents a different behavior: the mean equivalent width is essentially independent of column density for the high-ionization lines, and has a weaker increase with $N_{\text{H I}}$ than in the total sample for the low-ionization ones. There are two possible reasons for this difference. First, the DLAs in the metal sample are selected to be those with measured redshifts from the metal lines, and therefore where the metal lines have been individually detected in the BOSS spectra. This procedure selects DLAs with strong metal lines, and also spectra of high S/N. The low column density DLAs are included in the metal sample with a lower frequency than the high column density ones, with an important selection in favor of systems with strong metal lines (either because of high metallicity or high velocity dispersion, which reduces the degree of line saturation). The second reason is that some fraction of the DLAs at low column density may be false detections, where a combination of noise and the presence of a cluster of Ly α forest lines may be confused with a DLA in low-S/N spectra. The low column density DLAs should have a higher impurity fraction, or fraction of false systems, and this impurity fraction is significantly reduced when selecting systems that have associated metal lines detected. Therefore, the $\sim 25\%$ increase in the high-ionization mean equivalent width with $N_{\text{H I}}$ may in part be real for the total sample (not suffering from metal selection effects), but may also be due to a worsening sample purity at low column density for the total sample. These effects illustrate why special care must be taken

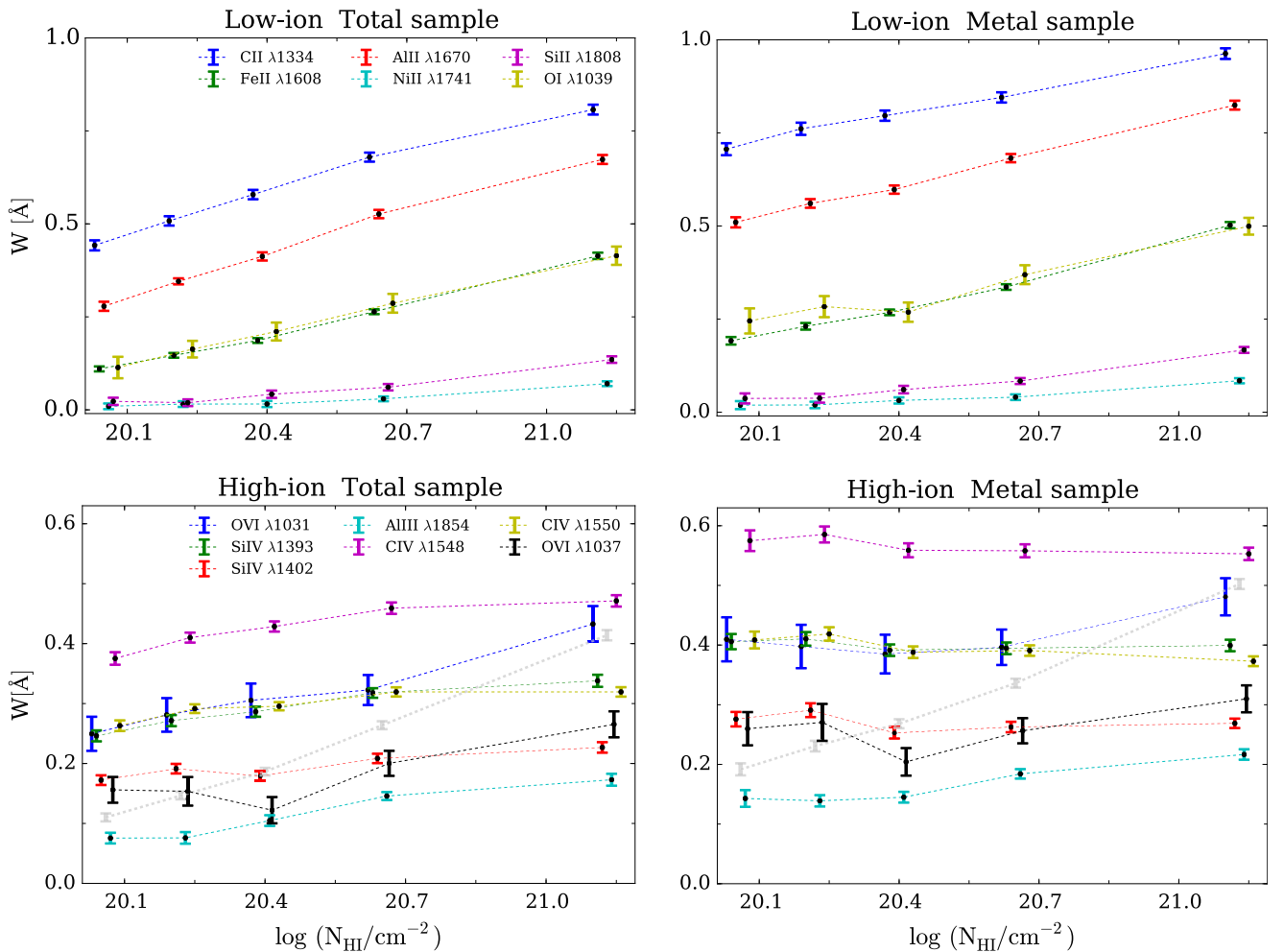


Figure 11. Top: mean equivalent width of low-ionization metal lines as a function of DLA H I column density, for the total (left panel) and metal sample (right panel). Bottom: same for the high-ionization doublet lines of C IV, Si IV, and O VI and the intermediate ionization line of Al III, for the total (left panel) and metal sample (right panel). The values of the Fe II $\lambda 1608$ line are also indicated in light gray for comparison between low- and high-ionization behaviors. Dotted lines connect the measured points to help visualize the dependence on N_{HI} . Horizontal positions of points with overlapping error bars have been slightly shifted for visual enhancement, but they are all based on a single set of five bins in N_{HI} . The large error bars of O VI lines reflect the effect of blending with the Ly α forest and other lines.

in the sample selection for evaluating mean properties of the DLA population.

Even though the metal sample results in a composite spectrum where weak lines can be detected at a greater statistical significance, it will not be used in the rest of this paper because it does not produce results that can be easily corrected for the sample selection effects. The question of the effect of the sample impurity (i.e., the rate of false DLAs in the total sample) needs to be addressed with simulations of DLA catalogs from mock spectra, and is left to be analyzed in future work when these simulations are available.

Additional interesting information can be obtained from the mean equivalent width ratio of the doublets of C IV and Si IV. The equivalent width ratio stays constant with column density near a value of 1.4–1.5 for both C IV and Si IV. This factor is between the values of 2 and 1, corresponding to the two extreme cases of completely optically thin and completely saturated lines, respectively. The fact that this ratio remains constant as the mean equivalent width increases suggests that the velocity dispersion, or the mean number of subcomponents, should be increasing with column density, although our uncertainties are still too large to place much confidence on this interpretation. The ratio of ~ 1.5 indicates that the

absorbers have a mixture of weak unsaturated components, and strong saturated ones, that contribute about equally to the total equivalent widths. The doublet equivalent width ratio of O VI appears to be larger, but the errors here are also larger and systematics due to the blending of the weaker line of the doublet with C II and O I lines are likely present.

5. Dependence of Equivalent Widths on z

We here explore the evolution of the mean metal line equivalent widths with redshift of the DLAs. We split the total and the metal samples into five DLA redshift intervals, [1.9–2.24], (2.24–2.4], (2.4–2.7], (2.7–3.0], (3.0–6.4], with mean redshift values 2.12, 2.32, 2.54, 2.84, and 3.50, respectively. The mean values of the column densities for each bin are 20.50, 20.50, 20.50, 20.49, and 20.46, respectively, showing little difference between them. We repeat the equivalent width and uncertainty calculations we did for the case of column densities, but this time for each redshift bin. The a parameter in Equation (9) is kept fixed to the same values used for the entire samples, assuming that it is independent of DLA redshift. The mean equivalent widths in every redshift bin are tabulated in Tables 10–13 in

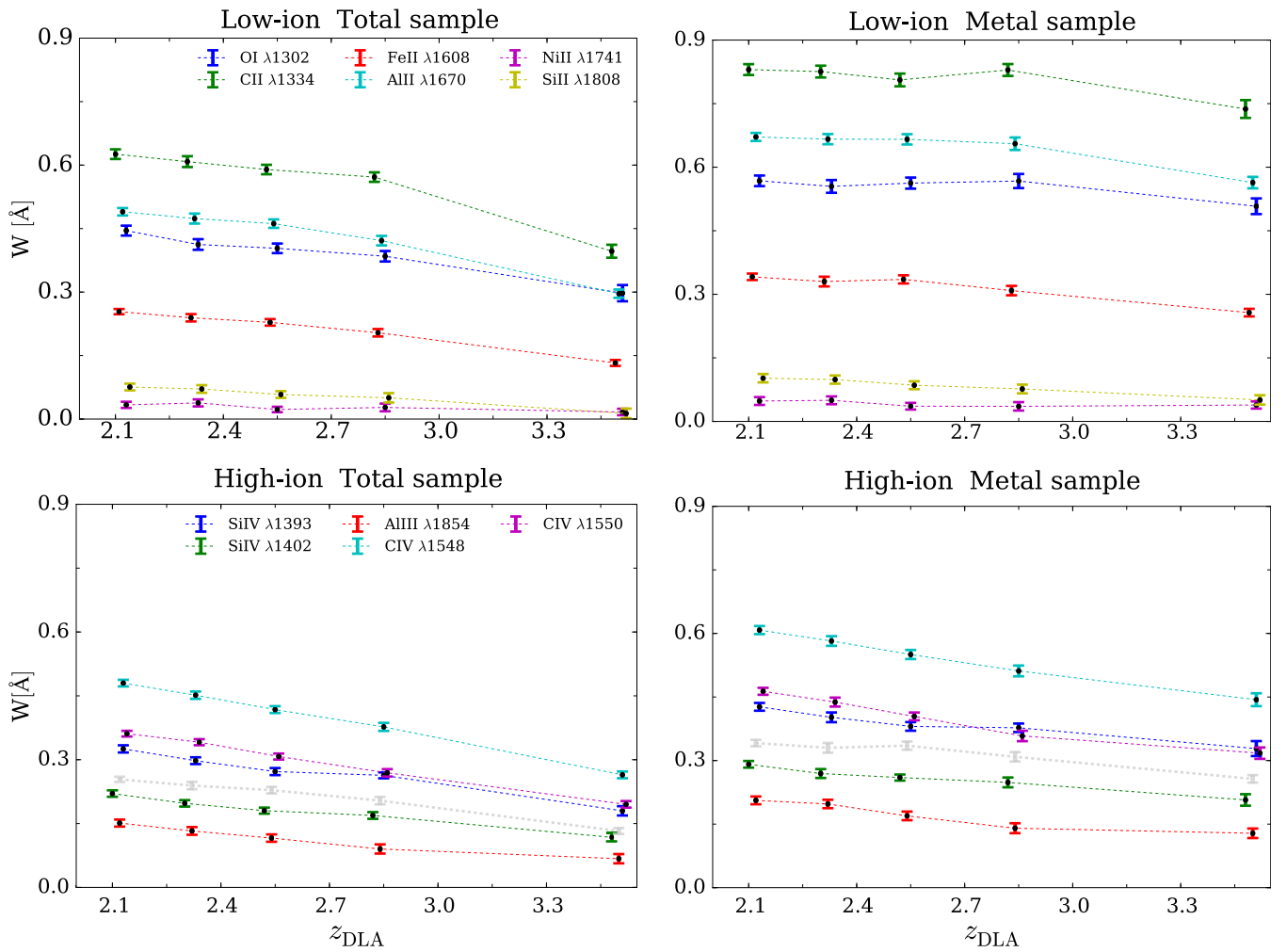


Figure 12. Top: mean equivalent width of low-ionization metal lines as a function of DLA redshift, for the total (left panel) and metal sample (right panel). Bottom: same for the high-ionization doublet lines of C IV and Si IV, and the intermediate ionization line of Al III. The values of the Fe II $\lambda 1608$ line are also indicated in light gray for comparison between low- and high-ionization behaviors. Dotted lines connect the measured points to help visualize the dependence on redshift. Horizontal positions of points with overlapping error bars have been slightly shifted for visual enhancement, but they are all based on a single set of five z_{DLA} bins.

Appendix A, separately for low-ionization and high-ionization species, and for the total and metal samples.

Figure 12 displays the evolution of the mean equivalent widths with redshift. The top panels show several low-ionization species. The points are slightly shifted horizontally from their original positions to clarify the visualization. A general decrease of equivalent width by a factor ~ 1.3 – 1.5 from $z \sim 2.1$ to $z \sim 3.5$ is apparent for the total sample (left panel). The nearly equal values of the mean column density at every redshift bin confirm that the observed trend is not driven by changes in $N_{\text{H I}}$. However, the effect of false positive DLA detections, which result in lower equivalent widths, might be present, especially at the highest- z bins. The evolution of the metal sample, which should be less affected by false positives, presents a slightly smoother decrease, by a factor ~ 1.1 – 1.2 in the same redshift range (right panel).

The bottom panels show the dependence of the mean equivalent widths on z for two high-ionization species, Si IV and C IV, and for an intermediate species, Al III. We also present the behavior of the Fe II $\lambda 1608$ line for comparison (in soft gray). The doublet of O VI is not shown as its rest-frame wavelength is only covered by the three upper redshift bins which, in turn, are those most affected by noise. Here, as for the

low-ionization species in the upper panels, the metal sample (right panel) suggests a smoother decrease with redshift than the total sample (left panel). However, for both samples, the equivalent width decreases by a factor $\gtrsim 1.5$ within the redshift range $z \sim 2.1$ to $z \sim 3.5$. Whether a different evolution between low- and high-ionization species exists or is an artifact driven by noise and/or systematics is unclear, and we defer more detailed examinations to future work.

6. Theoretical Model for Line Saturation

As previously described, the absorption profiles of the metal lines are mostly determined by the instrumental spectrograph resolution. The absorption system components are often much narrower than the BOSS resolution, and can therefore be saturated even though they appear to be weak (York et al. 2000). Although a fraction of DLAs are known to have velocity dispersions that are comparable to the BOSS resolution (Prochaska & Wolfe 1997), this intrinsic line width likely contributes only to extend the wings of the mean absorption profile that can be seen in the strongest lines (see, e.g., the C IV profile in Figure 18). Deconvolving the BOSS spectral point-spread function from the mean profile is difficult because of its wavelength and fiber-to-fiber dependence, and

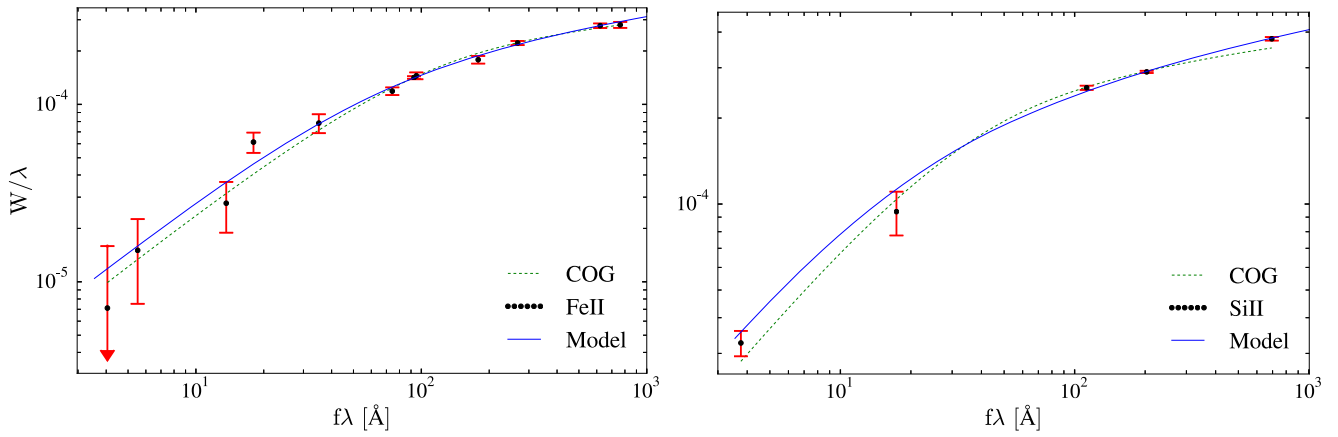


Figure 13. Equivalent widths divided by the line wavelength measured for the Fe II (left) and Si II (right) transitions in the stacked spectrum of the total sample, and best fit curve obtained with our model as a function of $f\lambda$ (solid blue lines). For comparison, we show the best fit curves from the curve of growth (COG) method (dashed green lines). The red arrow in the left panel denotes that the error is larger than the expected value.

inaccuracies in its determination. We therefore use only the mean equivalent widths of the lines as the quantity that can be determined from the BOSS stacked spectra we have created.

The physical quantities that the equivalent width depends on are the column density and the velocity distribution of each species. The velocity distribution is known to be generally complex, because several absorbing components are often resolved in the metal line profiles of DLAs (Prochaska & Wolfe 1997; Zwaan et al. 2008), which means that there is not a simple relation between mean equivalent widths and column densities that can be expressed in terms of a single velocity dispersion, as for a Voigt profile. The scenario that is usually invoked to explain the observed absorption profiles is that a number of gas clouds are orbiting inside a halo or thick disk (Haehnelt et al. 1998; Wolfe & Prochaska 1998; McDonald & Miralda-Escudé 1999), which randomly intercept the line of sight to the quasar. Every absorbing system is characterized by a halo velocity dispersion, which describes the random motions among the clouds seen as absorbing components in the spectra, and an internal cloud velocity dispersion, which can be partly thermal and partly turbulent, determining the width of the individual absorbing components. We shall use this scenario to construct a simple model for the relation of the mean equivalent width and column density for a large sample of DLAs similar to the one we are using here.

With this purpose in mind, we analyze in detail the transitions of Fe II and Si II for the total sample, which are the two species with the largest number of measurable absorption lines, 12 for Fe II and 5 for Si II (except for Ni II, which has 6 transitions, but they are weaker lines with a narrower range of oscillator strengths), most of which are strong enough to yield a reliable measurement of the mean equivalent width, W . We plot in Figure 13 the dimensionless ratio W/λ as a function of the product $f\lambda$ for each one of these transitions, where f is the oscillator strength of the line at wavelength λ . For a completely optically thin absorption line, the equivalent width is given by

$$\frac{W}{\lambda} = \pi f \lambda r_e N, \quad (12)$$

where $r_e = e^2/(m_e c^2)$ is the classical electron radius, e is the electron charge and m_e the electron mass. Therefore, in the optically thin regime, we expect $W/\lambda \propto f\lambda$ for the mean of a

DLA sample with any distribution of column densities. As an increasing fraction of the DLA components become optically thick with increasing f , the mean relation should flatten until W/λ becomes nearly constant with $f\lambda$ at a value determined by the mean maximum velocity range that is covered by the absorbing components in a DLA. This is indeed the behavior seen in Figure 13. The precise functional dependence of W/λ on $f\lambda$ cannot be reliably predicted from theory, because it depends on the detailed velocity and column density distribution and the internal velocity structure of the DLA absorbing components.

However, we can argue that all the low-ionization species measured in DLAs should follow the same functional form of W/λ versus $f\lambda$, except for a horizontal rescaling that reflects the element abundance. This relation follows from assuming that all the low-ionization species have the same distribution of velocities in the DLA sample we are using, and that different ionization corrections do not lead to significant differences, so that they all have the same distribution of optical depths within the velocity range of the absorbing systems except for the rescaling reflecting the abundance. In general, ionization corrections in DLAs are found to be <0.2 dex (e.g., Howk & Sembach 1999; Vladilo et al. 2001; Prochaska & Wolfe 2002; Kisielius et al. 2015), supporting the view that differences in the shape of the optical depth distribution among metal species should be minimal. A model is proposed below for the shape of W/λ versus $f\lambda$, which is displayed as the blue curves in Figure 13. This simple model allows us to infer mean column densities from the measured mean equivalent widths, up to the systematic errors arising from the model assumptions. We shall generally assume that the model can be applied with the same parameters to all low-ionization species. We will also apply the model to high-ionization species allowing for different fit parameters, since these absorbers are believed to reside in different regions and have different velocity distributions than the low-ionization species (e.g., Wolfe et al. 2005). We consider, however, this model to be less reliable for high-ionization species because of the lack of a test with many lines from the same species with different values of f , similar to the one provided by Fe II and Si II for low ionization.

Before describing this model, we should address the large differences in the error bars of different lines in Figure 13. Large errors are sometimes caused by blends with other

absorption features that are difficult to separate (e.g., the Si II $\lambda 1020$ transition appearing at $f\lambda = 17.1 \text{ \AA}$ in the right panel is blended with the Ly β transition), or when the lines are very weak. The leftmost Fe II line has an expected W value smaller than its uncertainty, so the lower edge of the error bar is replaced by an arrow.

6.1. Modeling Equivalent Widths as a Function of Oscillator Strength

For any metal line centered at wavelength λ_0 , we define the rest-frame equivalent width in units of velocity as:

$$W_v = \frac{c W}{\lambda_0} = \frac{c}{\lambda_0} \int d\lambda [1 - \exp(-\tau(\lambda))], \quad (13)$$

where the integral is performed over a rest-frame wavelength interval around λ_0 that contains the whole absorption line. We define the *linearized equivalent width* as

$$\frac{W_\tau}{c} = \int \frac{d\lambda}{\lambda_0} \tau(\lambda) = \pi f \lambda_0 r_e N, \quad (14)$$

Although the mean of W_τ is the quantity that is directly related to the mean column density, only the mean of W_v is measured from our BOSS stacked spectra.

For absorption lines that contain a single absorbing component with a Gaussian velocity dispersion (arising from thermal motions or from a turbulent velocity dispersion that also has a Gaussian distribution), the relation between W_v and W_τ is the well known Voigt curve of growth (Goody & Yung 1996). For a velocity dispersion σ , when $W_\tau \gg W_v$, we have

$$W_v \simeq 2\sigma \sqrt{2 \log[W_\tau / (\sqrt{2\pi} \sigma)]}. \quad (15)$$

The mean equivalent width resulting from the stacked metal lines of many DLAs is not related in the same simple way to the mean column density because each absorption system has a different distribution of optical depths. We search for a simple, physically motivated fitting formula to adjust the observed mean values of W_v of the low-ionization lines as a function of the values of W_τ that are theoretically predicted from column densities.

We assume the absorption lines are composed of subcomponents with an internal velocity dispersion σ , given by $\sigma_2 = \sigma_0^2 (m_H/m_i) + \sigma_h^2$, where σ_h is the turbulent (or hydrodynamic) velocity dispersion, assumed to be the same for all the lines of all the species, and σ_0 is the thermal velocity dispersion of hydrogen, which we shall fix to $\sigma_0 = 10 \text{ km s}^{-1}$, corresponding to the typical equilibrium temperature of photoionized gas $T \simeq 10^4 \text{ K}$. The mass of the atom of the species of each line is m_i , and m_H is the hydrogen mass.

We assume that the subcomponents of a certain absorption line are contained within an interval of velocity width V , which is wide enough so that any absorption outside this interval due to the line can be neglected. Let the probability distribution of the optical depth at any pixel in the spectrum within this interval of width V be $\psi(\tau)$. In other words, $\psi(\tau) d\tau$ is the fraction of pixels in the intervals of width V around the central wavelength of the line in any DLA that have an optical depth τ within the range $d\tau$. The two measures of the equivalent widths

are given by:

$$W_\tau = V \int d\tau \psi(\tau) \tau, \quad (16)$$

and

$$W_v = V \int d\tau \psi(\tau) [1 - e^{-\tau}]. \quad (17)$$

As a model for the probability distribution of the optical depth, we choose the function $\psi(\tau) = A/\tau$ within a certain range $\tau_{\min} < \tau < \tau_{\max}$, and $\psi = 0$ outside this range. The normalization constant is $A = 1/\log(\tau_{\max}/\tau_{\min})$. This definition is chosen as a simple approximation that assumes that τ varies over a broad range in a scale-invariant way. More realistically, there should be a continuous distribution of τ reaching down to zero, but we simply assume that τ_{\min} is small enough to neglect this detail. Let us now consider absorbers with a fixed W_τ , i.e., a fixed column density of a certain species absorption line. The maximum optical depth is obtained when only one Gaussian absorbing subcomponent accounts for all the absorption, with

$$\tau_{\max} = \frac{W_\tau}{\sqrt{2\pi} \sigma}. \quad (18)$$

When several subcomponents are present, each one must have a smaller central optical depth to produce the same W_τ , and our model assumes the distribution is flat in $\log \tau$. We now use the fact that the average number of absorbing subcomponents in DLAs is of order unity, to require that the mean W_τ , from Equation (16), be equal to that due to the case of a single component reaching the maximum optical depth τ_{\max} , i.e.,

$$VA(\tau_{\max} - \tau_{\min}) = W_\tau = \sqrt{2\pi} \sigma \tau_{\max}. \quad (19)$$

We assume that the ratio τ_{\max}/τ_{\min} is constant, independent of W_τ . We then obtain the following relation between V , τ_{\max} and τ_{\min} :

$$V = \frac{\sqrt{2\pi} \sigma \log(\tau_{\max}/\tau_{\min})}{1 - \tau_{\min}/\tau_{\max}} \equiv \sqrt{2\pi} \sigma_1, \quad (20)$$

where σ_1 is defined by the last equality to replace V , and can be interpreted as a rough estimate of the velocity dispersion of the subcomponent absorbers, or DLA clouds, within their host halo.

Finally, we find for the equivalent width W_v the expression

$$\frac{W_v}{W_\tau} = \frac{\log(\tau_{\max}/\tau_{\min}) - \int_{\tau_{\min}}^{\tau_{\max}} d\tau e^{-\tau}/\tau}{\tau_{\max} - \tau_{\min}}. \quad (21)$$

The model relating W_v to W_τ has only two free parameters: σ_h and σ_1 . The thermal dispersion is fixed to $\sigma_0 = 10 \text{ km s}^{-1}$. The fitting formula provides a value of W_v for any input value of W_τ : Equation (18) first reveals the value of τ_{\max} , the value of τ_{\min} is derived from Equation (20), and we then obtain W_v from Equation (21). These two free parameters can be fixed to be the same for all the low-ionization species, if we believe that the subcomponent kinematics are an invariant characteristic of the absorption profiles that has little dependence on the column density. Under this assumption, the dependence of W_v on W_τ is unique, and represents both the variation with absorption lines of different f for fixed column density, and the variation with column density for a fixed line. In addition, once σ_h and σ_1 are determined, the relation for each new species

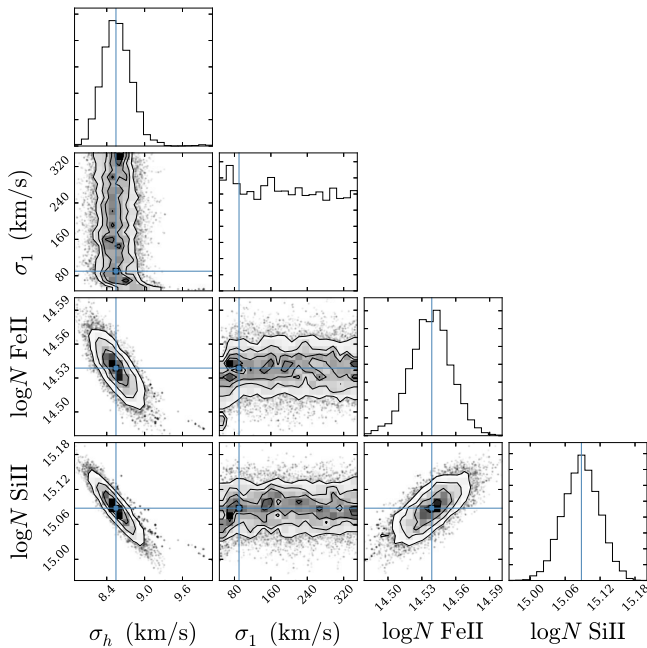


Figure 14. Parameter posterior probabilities of the joint fit of Fe II and Si II transitions for the estimation of σ_h and σ_1 and the two mean column densities in the total sample. The χ^2 contours are at 0.5, 1, 1.5, and 2σ levels (in some panels the 0.5σ contour is too small to be visible). The blue dots and lines, plotted over the contours, indicate the best fit. Note the large uncertainty of the σ_1 parameter. This figure has been produced using the open source code *triangle.py* from Foreman-Mackey et al. (2014).

depends on one additional parameter only: the ratio of its column density to the hydrogen one.

We obtain the best fit parameters for low-ionization species by computing a joint fit to the above-mentioned Fe II and Si II transitions, with the four free parameters $N_{\text{Fe II}}$, $N_{\text{Si II}}$, σ_h , and σ_1 , which minimizes the sum of the two χ^2 values. The column densities $N_{\text{Fe II}}$ and $N_{\text{Si II}}$ are the mean values for our DLA sample used directly in Equation (14) to compute W_τ for any absorption line. The best fit and parameter uncertainties are calculated with the open-source code *EMCEE* (Foreman-Mackey et al. 2013), using the Monte Carlo Markov Chain (MCMC) method. Figure 14 displays the one- and two-dimensional projections of the posterior probability distributions of the parameters; the contours are at 0.5, 1, 1.5, and 2σ levels.

The best-fit values and uncertainties, indicating the 16th and 84th percentiles (the mean of the two) in the marginalized distribution for σ_1 (for σ_h and $\log N$), are $\sigma_h = 8.56 \pm 0.22 \text{ km s}^{-1}$, $\sigma_1 = 90_{-16}^{+205} \text{ km s}^{-1}$, $\log N_{\text{Fe II}} = 14.538 \pm 0.011$ and $\log N_{\text{Si II}} = 15.087 \pm 0.012$. The fit reproduces the trend of the measured points, as seen in Figure 13 where our best-fit model is indicated by blue lines. The total χ^2 value of the fit is $\chi^2 = 14.98$, for an expected value of 13 (17 data points and four free parameters; some of the oscillator strengths have substantial uncertainties, which are not taken into account and may contribute to some increase in the value of χ^2). The halo velocity dispersion σ_1 is the parameter with the largest uncertainty: any value in the range $\sim 70\text{--}300 \text{ km s}^{-1}$ is essentially equally good, with no correlation with any of the other parameters. Our formula provides a good fit as long a turbulent velocity dispersion of individual components provides rough equipartition of the thermal and turbulent kinetic energies ($\sigma_h \simeq 8.6 \text{ km s}^{-1}$), and the well-

determined normalizations of the curves in Figure 13 correspond to the values of $N_{\text{Fe II}}$ and $N_{\text{Si II}}$.

For high-ionization species, we adopt the same assumptions as above and perform a joint fit to the two doublets C IV and Si IV, which have unblended, strong absorption lines. We use these species because they have the strongest lines, and are believed to be produced mostly by photoionization (e.g., Fox et al. 2007b). We assume the same fixed value for $\sigma_0 = 10 \text{ km s}^{-1}$ because these species are thought to arise in warm gas regions with temperatures $T \sim 10^4 \text{ K}$ (Lehner et al. 2008). We obtain the values $\sigma_h = 14.51 \pm 0.64 \text{ km s}^{-1}$, $\sigma_1 = 185_{-85}^{+112} \text{ km s}^{-1}$, $\log N_{\text{C IV}} = 14.396 \pm 0.019$ and $\log N_{\text{Si IV}} = 13.783 \pm 0.016$. The larger value for σ_h compared to the low-ionization species is indicative of a more violently turbulent environment for the high-ionization species. Changing the thermal velocity dispersion to $\sigma_0 = 30 \text{ km s}^{-1}$ reduces σ_h by $\sim 15\%$ and increases σ_1 by $\sim 5\%$, with variations of less than 1% on the column densities.

As explained in the previous section, the use of a curve of growth for fitting the transitions of a given species and obtaining the column density is not accurate for our composite spectra, due to the large number of components and systems contributing to the mean absorption features. Although a detailed assessment of our theoretical model is beyond the scope of this work, we perform a simple comparison with the curve of growth approach, since the latter is broadly used in absorption line studies, e.g., in the recent work by Noterdaeme et al. (2014). We use the publicly available package *linetools*¹⁰ to find the best-fit parameters of the curve of growth, column density, $N(\text{cm}^{-2})$, and velocity dispersion, $b(\text{km s}^{-1})$, applied to the species for which we have more transitions, i.e., Fe II, Si II, and Ni II. The dashed green lines in Figure 13 show the resulting curves for Fe II and Si II. The best-fit parameters for the three species are $\log N_{\text{Fe II}} = 14.452 \pm 0.010$, $\log N_{\text{Si II}} = 14.957 \pm 0.095$, and $\log N_{\text{Ni II}} = 13.843 \pm 0.072$, with Doppler parameters $b_{\text{Fe II}} = 24.04 \pm 0.73$, $b_{\text{Si II}} = 26.18 \pm 1.39$, and $b_{\text{Ni II}} = 3.21 \pm 0.49$. These results are significantly different from those obtained with our model, which allows for a distribution of component structure and velocity dispersions.

6.2. Mean Column Densities of Low- and High-ionization Species

We now assume σ_h and σ_1 to be constant for all the low- and high-ionization species, fixing their values to the best fit obtained for the Fe II and Si II transitions, $\sigma_h = 8.56 \text{ km s}^{-1}$ and $\sigma_1 = 90 \text{ km s}^{-1}$, and for C IV and Si IV, $\sigma_h = 14.51 \text{ km s}^{-1}$ and $\sigma_1 = 185 \text{ km s}^{-1}$, respectively. For every species we fit the curve of this fixed model with the mean column density N as the only free parameter, i.e., we assume the relation of W_ν and W_τ is fixed, and fit only the constant of proportionality relating W_τ to $f\lambda$, which is proportional to the mean column density of the species in our DLA sample through Equation (14). This approach yields a ratio of the ion abundance to that of H I considering the logarithm of the mean hydrogen column density of the total sample, $\log \bar{N}_{\text{H I}} = 20.49$. If the ionization corrections can be neglected (i.e., assuming that the fraction of the species in question is the same as the neutral hydrogen fraction), this result is equal to the element abundance compared to hydrogen.

The results of this model are presented in the middle column in Table 2. Errors include equivalent width measurement

¹⁰ <http://linetools.readthedocs.io/en/latest/index.html>

uncertainties only, computed earlier from our bootstrap analysis of the total DLA sample, and do not include any systematic errors arising from our model assumptions. We use all the lines reported in Table 4. For species that have only one line, the error of the column density directly reflects the error of the equivalent width; when there are several lines the error is reduced by obtaining the best fit to all the lines.

We also report column densities for four intermediate-ionization species from Table 4: Al III, C III, S III, and Si III, using the same parameters as for the low-ionization species since they are believed to have similar velocity distributions (Wolfe et al. 2005). For the high-ionization species we list the results obtained for the fit to C IV and Si IV for the results in Table 5 with their different parameters σ_1 and σ_h , and apply them also to N V and O VI. These more highly ionized species are believed to arise from higher temperature gas, (see Fox et al. 2007b; Lehner et al. 2008; Fox 2011, and Section 7), with velocity distributions that are likely broader than for C IV and Si IV, implying perhaps an overestimate of the O VI column density, but not for N V which produces lines that are mostly optically thin.

The strongly blended lines in Table 1 are in general not used for the determination of column densities whenever we have other lines of the same species in Table 4, because blending adds additional modeling uncertainties, as discussed in Section 3.3. However, there are several species that are only measurable using these blended lines. In the case of Ti II and N I, we use the Ti II blend at 1911 Å and the N I blend at 1200 Å, containing only lines from a single species, to determine the mean column densities directly from the “fitted W ” results of the lines. These lines are not very close together, so we believe that the systematic effects discussed in Section 3.3 are not important in this case. The Ti II line is in any case quite weak and has a large statistical error. The rest of the lines with column densities listed in Table 2 derived from blended groups are for Zn II, C II*, Fe III, and S IV, which are inferred after correcting for lines of other species. We will discuss these more complex cases further in Section 6.3.

The third column in Table 2 denotes the abundances obtained using the expression $[X/H I] = \log(N_X/N_{H I}) - \log(N_{X_e}/N_{H I})_{\odot}$, where X denotes the ion of interest, X_e the corresponding element, and \odot denotes solar values. We use solar abundances for elements from the photospheric data in Table 1 of Asplund et al. (2009). These results for $[X/H I]$ can be interpreted as element abundances relative to solar values if ionization and dust depletion corrections can be neglected. We give the abundances only for species that are expected to have fractional columns compared to their elements similar to the neutral hydrogen fraction (often the first ionized species, but the neutral one for O).

Doubly ionized species generally have column densities that are not much lower than the singly ionized ones. In particular, the Si III and Si II column densities are equal within the measurement error, and that of C III is substantially higher than for C II. In the case of C III, the column density we obtain is subject to a large systematic error due to our modeling assumptions. The C III column density is derived only from the line at 977 Å, which has the highest value of $W/\lambda \simeq 6.6 \times 10^{-4}$ of any of our lines, and involves a large extrapolation of our model relating W/λ to $f\lambda$ from the curve in Figure 13 which is not tested from the Fe II and Si II lines in the figure. For the cases of Si III, S III, and Al III, there is no extrapolation in the values of W/λ ; the velocity structure

Table 2
Derived Mean Column Densities in the Total Sample

| Metal Ion | $\log \bar{N}$ | $[X/H I]$ |
|-----------|--------------------|------------------|
| Al II | 13.806 ± 0.016 | -1.13 ± 0.03 |
| C II | 16.025 ± 0.060 | -0.90 ± 0.08 |
| C II* | 13.351 ± 0.060 | ... |
| Cr II | 12.908 ± 0.117 | -1.22 ± 0.12 |
| Fe II | 14.538 ± 0.011 | -1.45 ± 0.04 |
| Mg I | 12.387 ± 0.073 | ... |
| Mg II | 14.943 ± 0.041 | -1.15 ± 0.06 |
| Mn II | 12.300 ± 0.188 | -1.62 ± 0.19 |
| N I | 14.128 ± 0.025 | ... |
| N II | 14.497 ± 0.051 | ... |
| Ni II | 13.452 ± 0.030 | -1.26 ± 0.05 |
| O I | 15.959 ± 0.025 | -1.22 ± 0.06 |
| P II | 12.890 ± 0.141 | -1.01 ± 0.14 |
| S II | 14.731 ± 0.032 | -0.88 ± 0.04 |
| Si II | 15.087 ± 0.012 | -0.91 ± 0.03 |
| Ti II | 12.264 ± 0.193 | -1.19 ± 0.20 |
| Zn II | 12.157 ± 0.111 | -0.89 ± 0.12 |
| <hr/> | | |
| Al III | 12.946 ± 0.023 | ... |
| C III | 16.696 ± 0.121 | ... |
| S III | 14.345 ± 0.123 | ... |
| Si III | 15.107 ± 0.036 | ... |
| Fe III | 13.905 ± 0.095 | ... |
| <hr/> | | |
| C IV | 14.396 ± 0.019 | ... |
| N V | 13.074 ± 0.090 | ... |
| O VI | 14.771 ± 0.030 | ... |
| S IV | 13.707 ± 0.184 | ... |
| Si IV | 13.783 ± 0.016 | ... |

Note. Mean column densities derived from the measured equivalent widths and our model relating W_v to W_r , for low-, intermediate-, and high-ionization species are listed in the central column. Abundances, relative to solar values from Asplund et al. (2009) and derived with no ionization or dust depletion correction, are in the third column, using a mean $N_{H I} = 10^{20.49} \text{ cm}^{-2}$. Intermediate-ionization species, fitted using the low-ionization model parameters σ_1 and σ_h , are presented in the middle rows, while high-ionization species, using their own separate parameters, are listed at the bottom. Uncertainties include only the equivalent width measurement errors, and not model systematic errors, which are particularly severe for C III (derived from the line with the highest value of W/λ).

may still be different from the singly ionized species, but the overestimate of the column density this may induce is probably not large. These cases demonstrate that the doubly ionized species can have column densities close to the singly ionized species, implying a substantial ionization correction for the abundances. The ratios of double- to single-ionization species can be used to constrain photoionization models of DLAs (e.g., Vladilo et al. 2001). The column densities of more highly ionized species are, as expected, substantially lower than those of their low-ionization counterparts.

In the case of neutral species, the mean column density of N I is about half that of N II. Nitrogen, with an ionization potential of 14.5 eV, should be completely neutral in the deeply self-shielded inner parts of DLAs, so in this case the ionization correction is quite important. The fraction of oxygen in the form of O I is probably even smaller than for nitrogen, owing to its lower ionization potential, so our derived nitrogen and oxygen abundances are highly dependent on these uncertain ionization corrections.

Without ionization and dust depletion corrections, the abundances for iron and silicon would be $[\text{Fe II}/\text{H I}] = -1.45 \pm 0.04$ and $[\text{Si II}/\text{H I}] = -0.91 \pm 0.03$, respectively. In this case, the ionization corrections are likely to be similar for silicon and iron because of the similar ionization potentials. The measured ratio $[\text{Si II}/\text{Fe II}] \simeq 0.54 \pm 0.05$, significantly higher than the typical intrinsic α -element enhancement in DLAs relative to the Sun ($[\alpha/\text{Fe}] \sim 0.3$, e.g., Prochaska 2003; Rafelski et al. 2012; Cooke et al. 2015), reflects the effect of the large dust depletion of iron compared to silicon (e.g., Kulkarni et al. 1997; Pettini et al. 1997; Vladilo 2002; Akerman et al. 2005; Cooke et al. 2011, 2013; Vladilo et al. 2011).

6.3. Modeling Blended Lines

Many lines of high scientific interest are blended. As described in Section 3.3, the equivalent widths for the groups of blended lines listed in Table 1 are measured by jointly fitting the parameter b in Equation (9) for each line, while the a parameter is, as usual, kept fixed. This approach leads to large, correlated errors for the equivalent widths of the individual lines contributing to the blend, as listed in the fourth column of Table 1, and to systematic errors caused by our assumption that the total transmission is simply the product of the individual line transmissions. In several cases, we are particularly interested in measuring the equivalent width of one line in one of these groups, where all the other lines of the group can be modeled from other lines of the same species measured independently. For example, the only line available for S IV is at 1062 Å and is blended with several Fe II lines, which can be modeled from the set of all lines used in Figure 13. Using the model prediction for the Fe II lines can allow for a better estimate of the S IV line equivalent width.

We use this approach for five of the line groups listed in Table 1, in order to measure lines of S IV, Fe III, C II*, and Zn II (the last in two different blended groups). The predictions for the modeled lines are listed in the fifth column of Table 1, obtained from the column densities listed in Table 2 and the fixed values of the σ_1 and σ_h parameters of all the low-ionization lines. The errors of these modeled equivalent widths are small because they are derived from the error in the column density of each element, without including model uncertainties. We repeat the fit to the measured profile of the blended group by fixing the b parameter of all the modeled lines to reproduce these predicted equivalent widths, and leaving as a single free variable the b parameter of the line that is inferred from this model prediction (the a parameter of all lines is fixed as usual by Equation (10)). The results for the equivalent widths of these inferred lines are listed in the sixth column, for the five mentioned groups. Errors are computed from bootstrap realizations that keep the modeled lines fixed. They therefore include only the observational noise and continuum modeling, but not the systematic uncertainty of the modeled lines. This process is not applied in the case of the N III line at 990 Å, for which the equivalent width is strongly blended with a Si II line and partly blended also with the O I group, and is too small to be measured from our stacked spectrum.

As mentioned before, the Ti II group at 1911 Å and the N I group at 1200 Å are used as the only measurements to infer the Ti II and N I column densities. The inferred W values in the fifth column are then derived from our model using these inferred column densities.

Finally, there are five absorption features in which all the lines can be modeled from other measured lines: the O I group, the Fe II–N I group, the Fe II group, the S III–Si II group, and the Si II–Fe II group. These modeled equivalent widths are also given in the fifth column of Table 1. In addition, the table presents the total inferred equivalent width from these modeled lines in the sixth column, for these five blended groups. These values are often consistent with the measured total equivalent widths of the group, supporting the reliability of our model, with some exceptions. The main exception is the O I group, for which the inferred W is larger than the total W measured for the blend. This behavior can be attributed to the systematic error discussed in Section 3.3: the three O I lines are very close together, and while we assume that their absorbing components are independent and the transmission of the individual lines can simply be multiplied to obtain the total transmission, in reality the absorbing components are of course the same in all three lines in each individual DLA and are often much narrower than the BOSS spectrograph resolution, and almost certainly highly saturated. Therefore the measured W is smaller than the inferred W when treating the three lines as independent. The other smaller discrepancies in the remaining blend groups can be attributed to the same systematic effect.

Our treatment of the blend groups provides mean equivalent widths for lines of three species that are in general extremely difficult to measure: S IV $\lambda 1062$, Fe III $\lambda 1122$, and C II* $\lambda 1335$. The first two are in the Ly α forest, and blended with Fe II and Si II lines. The lines are therefore doubly difficult to measure from individual DLA systems, even in spectra of high resolution and S/N. The Ly α forest contamination is automatically removed in our technique, where we measure only the mean equivalent width of a large sample of DLAs. The Fe II or Si II contamination is reliably predicted by our model, as illustrated by the small scatter of the measured points in Figure 13 and the χ^2 value of our three-parameter fit to these points. The systematic effects of correlated components are in this case less serious, because the line separations are comparable to the BOSS resolution so that overlap of narrow components is not frequent. Still, the errors we obtain in the end for these species are relatively high, especially for S IV because it accounts for only $\sim 15\%$ of the total equivalent width of the blended line group.

Finally, we can derive the equivalent width of the Zn II lines from the blends at 2026 and 2062 Å. The most reliable measurement originates from the 2026 Å blend, for which the Cr II and Mg I contributions are a relatively small correction, so we use only this group to derive the Zn II column density included in Table 2. This result yields a mean abundance with no ionization correction of $[\text{Zn II}/\text{H I}] = -0.89 \pm 0.12$. This element is a particularly good tracer of metallicity because it is one of the least affected by dust depletion (e.g., Pettini et al. 1990, 1997; Prochaska & Wolfe 2002; Jenkins 2009; Cooke et al. 2011, 2013). We discuss and compare these abundance values in Section 7.

6.4. Behavior of the Model Parameters with $N_{\text{H I}}$

We now explore the behavior of our three model parameters (N , σ_1 , and σ_h) for the Fe II and Si II transition lines with $N_{\text{H I}}$. We make use of the total sample, now dividing it into the following three $N_{\text{H I}}$ intervals chosen to contain a similar number of DLAs: [20.0–20.24], (20.24–20.60], (20.6–22.50], with mean values of $\log(N_{\text{H I}}/\text{cm}^{-2})$ of 20.11, 20.41, and

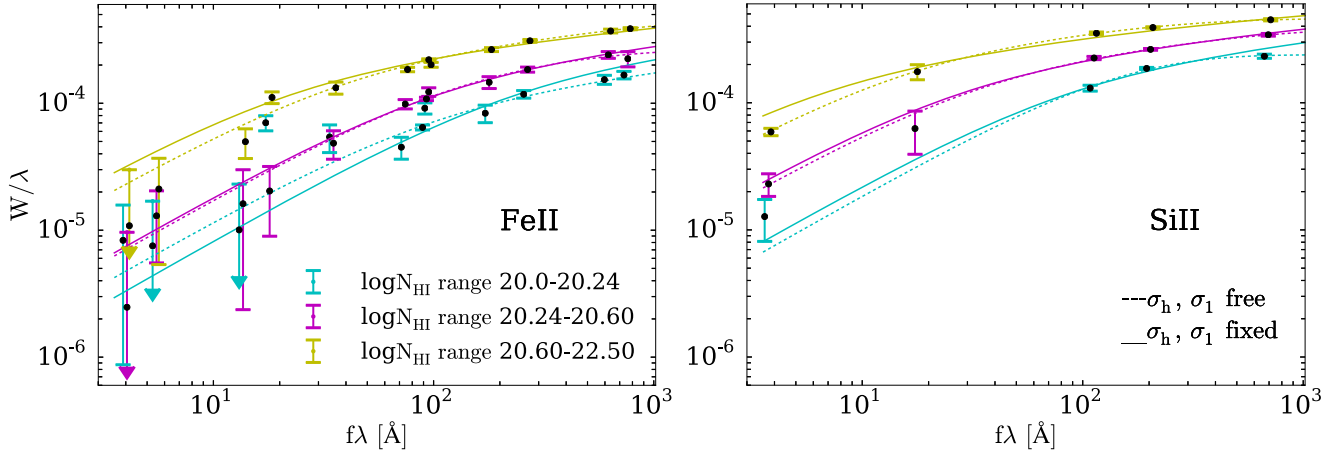


Figure 15. Measurements of W/λ vs. $f\lambda$ in $3N_{\text{H I}}$ intervals. Arrows at the bottom end of an error bar indicate that the error in W is larger than its expected value. The solid lines represent the modeled curves when the parameters $\sigma_h = 8.56 \text{ km s}^{-1}$ and $\sigma_1 = 90 \text{ km s}^{-1}$ are fixed to the values found in Section 6.1, and only the column density of the species, N , is set free. The dashed lines denote the model best-fit results when all three parameters are allowed to vary. Left panel: fit to the Fe II transitions. Only 11 lines are used for the fit, after excluding the line at $f\lambda \simeq 18 \text{ \AA}$. Right panel: fit to the Si II transitions. We consider five lines, except in the lowest column density range, where the effect of noise does not allow for reliably fitting one of the transitions. Data points are slightly shifted from their actual position in $f\lambda$ to avoid cluttering of error bars.

Table 3
Best-fit Parameters for the Three $N_{\text{H I}}$ Ranges

| $\log(N_{\text{H I}}/\text{cm}^{-2})$ | | Fe II | | Si II | |
|---------------------------------------|------------|--------------------|--------------------|--------------------|--------------------|
| | | Fixed | Free | Fixed | Free |
| 20.11 | $\log N_X$ | 13.967 ± 0.020 | 14.098 ± 0.072 | 14.423 ± 0.017 | |
| | σ_h | 8.56 | 5.59 ± 0.61 | 8.56 | |
| | σ_1 | 90 | 45^{+211}_{-23} | 90 | |
| | χ^2 | 33.36 | 13.20 | 23.55 | |
| 20.41 | $\log N_X$ | 14.334 ± 0.017 | 14.318 ± 0.053 | 14.913 ± 0.019 | 14.863 ± 0.086 |
| | σ_h | 8.56 | 9.92 ± 1.01 | 8.56 | 9.56 ± 0.61 |
| | σ_1 | 90 | 31^{+191}_{-12} | 90 | 46^{+202}_{-23} |
| | χ^2 | 4.92 | 3.96 | 3.49 | 1.25 |
| 20.97 | $\log N_X$ | 14.994 ± 0.015 | 14.773 ± 0.076 | 15.540 ± 0.017 | 15.320 ± 0.036 |
| | σ_h | 8.56 | 12.03 ± 0.88 | 8.56 | 12.15 ± 0.66 |
| | σ_1 | 90 | 51^{+198}_{-9} | 90 | 54^{+2}_{-2} |
| | χ^2 | 31.02 | 9.43 | 68.26 | 0.35 |

Note. Best-fit values and errors for the three fit parameters, and values of χ^2 for the fits, in the three column density intervals. The mean hydrogen column density is denoted in the first column. Parameter values for the fixed case (with the σ_h and σ_1 values found in Section 6.1) are given in the third and fifth columns for Fe II and Si II, and for the free case with three parameters allowed to vary in the fourth and sixth columns. Values of σ_h and σ_1 are in units of km s^{-1} . The expected χ^2 values are $\chi^2 = 9$ and 7 for Fe II, and $\chi^2 = 4$ and 2 for Si II, for the *fixed* and *free* cases, respectively. No fit is obtained for the lowest $N_{\text{H I}}$ interval in the free case for Si II, because two of the Si II lines do not have significant detections.

20.97, respectively. We compute the three composite spectra following the procedure explained in the above sections and calculate the equivalent widths of the metal lines. The left panel of Figure 15 presents the measurements of W/λ versus $f\lambda$ of the Fe II transition lines in these three $N_{\text{H I}}$ intervals. When modeling these results, we ignore the Fe II $\lambda 1125$ line, with points at $f\lambda \simeq 18 \text{ \AA}$ in this panel of Figure 15. This line is, particularly for the lowest column density interval, strongly affected by the noise and continuum systematic errors, and is a clear outlier from the relation followed by the other lines; for some reason that we have not been able to determine, this is not properly captured by our bootstrap calculation of the uncertainties. The right panel displays the five transitions of

Si II. For the lowest column density range we have considered four points since in one case we have not been able to obtain a measurement for the equivalent width, owing to excessive noise in this very weak transition line.

We obtain first a fit to the data setting σ_h and σ_1 to the fixed values found in Section 6.1, with the Fe II and Si II column densities as the only free parameter. The result is presented in Table 3, and the fitted curves are displayed as the solid lines in the left and right panels of Figure 15 for Fe II and Si II, respectively. The expected value of χ^2 is in this case equal to 10 for Fe II and 4 for Si II, with 11 and five lines (four in the lowest column density range due to noise effects) used for Fe II and Si II, respectively, and only one free parameter for each

species. The values of the fits in Table 3 demonstrate that the fits are not good except for the middle $N_{\text{H I}}$ interval: the slope of the W/λ versus $f\lambda$ curve is too shallow (steep) for the high (low) $N_{\text{H I}}$ interval, compared to the data, as clearly seen in the left panel of Figure 15 for the case of Fe II. A similar trend is observed for the Si II lines in the right panel.

Good fits are obtained when all three parameters are allowed to vary in each $N_{\text{H I}}$ interval, as represented by the values of χ^2 in Table 3 for the free cases. We have not been able to fit one of the Si II transitions, that at $f\lambda \sim 18 \text{ \AA}$, due to the effect of noise, and for this reason we do not present the values for this free case. The general improvement is mainly related to an increase of σ_h with $N_{\text{H I}}$, which allows adjusting the slope of the curve to that shown by the data, as visible in Figure 15. The value of σ_1 is lower than for the fixed case, but generally also with a large uncertainty for the allowed upper range. Surprisingly, for the upper density range of Si II, σ_1 is tightly constrained, contrary to the results in other cases. This behavior is produced by the three rightmost data points, which have the smallest uncertainties and are well fitted by the model. Therefore, small departures from the best-fit σ_1 value produce large changes in χ^2 , thus constraining the range of allowed values in the parameter space. The ratio of the metal column density to $N_{\text{H I}}$ now decreases slightly with $N_{\text{H I}}$.

We conclude that, although our model works well as a fitting formula for our observational results of the equivalent width dependence on f displayed in Figure 13, it should not be interpreted as a physical model in a straightforward way, because the values of σ_h and σ_1 need to vary when we consider DLAs in different $N_{\text{H I}}$ intervals. The increase of σ_h with $N_{\text{H I}}$ is probably not directly related to a real increase of the internal dispersion from turbulence of absorbing components, but to the need to fit a variable shape of the W/λ versus $f\lambda$ curves that is caused by other effects. A more accurate model that is calibrated to precisely account for the properties of metal lines in high-resolution spectra would be required to improve the physical interpretation of these fits. In the meantime, the validity of the column densities in Table 2 is subject to our assumption that the curve presented in Figure 13 has a unique shape for all the species we consider, and is furthermore not affected by any photoionization and dust depletion corrections.

The trend of the declining ratio $N_{\text{Fe II}}/N_{\text{H I}}$ and $N_{\text{Si II}}/N_{\text{H I}}$ with column density in the results of Table 3 appears only when all three parameters are allowed to vary. Several works have suggested a decrease of metallicity with hydrogen column density in DLAs (e.g., Boisse et al. 1998; Kulkarni & Fall 2002; Khare et al. 2004; Akerman et al. 2005; Meiring et al. 2006), which could also extend to sub-DLAs (Dessauges-Zavadsky et al. 2003; Péroux et al. 2003a; York et al. 2006; Khare et al. 2007; Kulkarni et al. 2007, 2015; Som et al. 2013, 2015). As seen in Figure 14, the value of σ_h and the derived metal column densities are anticorrelated. The trend of an increasing σ_h with $N_{\text{H I}}$ is therefore correlated with the decrease of the ratio of metal columns to the hydrogen column. In fact, when we fix the parameters σ_1 and σ_h , the column density ratios (see Table 3) remain constant. We have further checked this point by dividing our sample of DLAs into only two groups: systems that are usually classified as sub-DLAs in the literature, with $N_{\text{H I}} < 10^{20.3} \text{ cm}^{-2}$ (and a mean column density in our total sample of $10^{20.14} \text{ cm}^{-2}$), and standard DLAs, with $N_{\text{H I}} > 10^{20.3} \text{ cm}^{-2}$ (with a mean column density of $10^{20.72} \text{ cm}^{-2}$ in our total sample). We find results very similar to those in Table 3: the ratios of $N_{\text{Fe II}}$ and $N_{\text{Si II}}$ to $N_{\text{H I}}$ are higher

in sub-DLAs by ~ 0.2 dex compared to standard DLAs, but the value of σ_h is 7 km s^{-1} for sub-DLAs compared to 10 km s^{-1} for standard DLAs. These variations are consistent with the expected correlation of errors seen in Figure 14, and we therefore conclude that the decline of column density ratios with $N_{\text{H I}}$ is not necessarily a real effect.

We do not assess the evolution of our model parameters with redshift, because of the unknown systematic uncertainties and dependencies on the model, and the small redshift range covered by our DLA sample.

7. Discussion

This paper has presented a new technique to study mean properties of the metal lines of a sample of DLAs. After evaluating a continuum for the mean quasar spectrum in our sample of 34,593 detected DLAs, the composite DLA absorption spectrum presented in Figures 7 and 8 is obtained for the total and metal samples, respectively, from which we obtain mean equivalent widths of all the detectable metal lines. This is the largest sample of DLAs ever analyzed for this purpose. Previously, similar stacking techniques were applied by Khare et al. (2012) for the purpose of measuring the effect of dust reddening and determining mean equivalent widths. Here, we have focused on completing a more extensive analysis of mean equivalent widths of all the metal lines we can detect with our much larger sample, for which we are presenting detailed tables with bootstrap errors that include the uncertainty in the continuum determination. Specifically, we have analyzed the dependence of the mean equivalent width on $N_{\text{H I}}$ for low- and high-ionization lines, developed a model for the effects of line saturation to relate equivalent widths to mean column densities, and used the model to separate the contributions of lines contributing to several blended groups listed in Table 1.

The advantage of using this stacking technique with a very large sample is that the superposition of the forest of Ly α and higher-order Lyman series lines from the intergalactic medium with the metal lines associated with DLAs is automatically removed. We can therefore measure several lines at wavelengths which have never been previously measured without the ambiguity due to the contamination by the forests. Of course, the BOSS spectra are missing all the information on the rich velocity structure of the DLA metal lines that is observed in high-resolution, high-S/N spectra, but we must bear in mind that even in the highest-quality spectra, the individual components in metal lines can be highly saturated and arise from gas at different densities and temperatures, with a variable degree of turbulence, a situation which is not essentially different from the situation we face when trying to model the mean equivalent widths we measure here.

7.1. Dependence of Mean Equivalent Widths on $N_{\text{H I}}$

As described in Section 4, whereas there is a clear increase of W with $N_{\text{H I}}$ for low-ionization lines, the equivalent widths of high-ionization lines stay practically constant as $N_{\text{H I}}$ increases. This result is clear observational evidence in favor of the widely believed picture that low-ionization metal lines arise in self-shielded gas that is centrally concentrated in the absorption systems in a similar way as atomic hydrogen (e.g., Wolfe et al. 2005, and references therein). The high-ionization lines must, on the other hand, arise in a more extended gas distribution

around the self-shielded gas to explain their weak dependence on N_{HI} . This picture has also been supported in the past by the different velocity profiles of low-ionization and high-ionization species, indicating that they arise from different gaseous structures (Wolfe & Prochaska 2000; Prochaska & Wolfe 2002; Fox et al. 2007b), but our results uniquely demonstrate that the high-ionization gas arises in a more extended spatial region that surrounds the low-ionization gas, as this is the only way to understand the nearly uniform properties of high-ionization lines over DLAs with highly variable low-ionization column densities, combined with independent observations of the higher incidence rate of absorption systems selected from C IV and other high-ionization lines compared to DLAs (Shull & Thronson 2012).

As explained in Section 4, it is not clear from our observations if the high-ionization lines have a weak increase of W with N_{HI} , owing to selection effects in the DLA samples we use. Our metal sample, which includes only DLAs with a detected presence of metal lines at the individual basis, is consistent with a constant W with N_{HI} , but this result may be affected by a stronger selection in favor of metal-rich systems at low N_{HI} , compared to the mean. This interpretation is in fact consistent with the histograms in the top panel of Figure 1, demonstrating a clear increase of the fraction of DLAs in the metal sample with N_{HI} . However, the effect may also be due in part to a fraction of false DLAs in our sample that is higher at the low end of our column density range. The relative importance of these two effects can only be modeled with detailed mocks that simulate the entire process of DLA detection. Undertaking such a task is difficult because false DLAs will often be the result of clusters of Ly α forest lines of high column density (not reaching DLA values) that may also have metals associated with them.

At present, we can only conclude that any correlation of the high-ionization lines with N_{HI} in DLAs cannot be stronger than the result we have found for our total sample. The general picture described above postulates that most of the atomic hydrogen in DLAs, together with low-ionization metal lines, should arise from relatively dense, self-shielded clouds, whereas the high-ionization species should mostly arise in lower density, more extended, unshielded gas. Therefore, in this picture, the column densities of the two types of species should present little correlation in any individual halo. However, a correlation may be induced by a dependence of the N_{HI} radial profile in the self-shielded clouds of DLAs on the metallicity or velocity dispersion of the halo (note that the velocity dispersion increases the metal equivalent widths, even at fixed metallicity, because of line saturation effects). Indeed, a correlation between the equivalent widths of the lines C IV λ 1548 and Si II λ 1526 was reported by Prochaska et al. (2008) (their Figure 8). If absorption systems with weak metal lines have broad cores and rarely reach the highest hydrogen column densities in our sample, whereas systems with stronger metal lines have more cuspy N_{HI} profiles with higher central values, that would induce an increase of the high-ionization lines W with N_{HI} even if the high-ionization gas has a constant W unrelated to N_{HI} for individual systems. This topic can motivate further work on correcting for any sample selection effects in the future.

We have also measured the dependence of W on N_{HI} for the intermediate-ionization species Al III, C III, S III, and Si III. The

results, given in Tables 6 and 8, and in Figure 11 for the Al III case, tend to show an increase of W with N_{HI} that lies between the behavior of low- and high-ionization lines, although with fairly large uncertainties. These intermediate species can be formed via X-ray photoionization in self-shielded regions, and may arise in the same gas region as low-ionization species (Wolfe et al. 2005), but may also have an important contribution from the more extended regions of the high-ionization gas. The results suggest that S III and Si III behave more similarly to the high-ionization lines, and Al III and C III behave more similarly to the low-ionization lines, but the uncertainties are too large to reach a clear conclusion at this point, and further modeling of the sample selections is required. The point we wish to stress here is that these observations have a high potential to constrain models for the distribution of gas in halos and their photoionization state, and to test theoretical results from simulations of galaxy formation.

7.2. Mean Abundances of Low-ionization Species

In Section 6, we presented our model for line saturation used to derive the column densities listed in Table 2. How reliable are these column densities? Our basic argument for believing they are approximately correct is that the curves presented in Figure 13 have reached the unsaturated regime at low $f\lambda$, i.e., they follow a linear relation $W/\lambda \propto f\lambda$ from which the column densities are derived. The problem is, of course, that the lines we can measure at low $f\lambda$ have large equivalent width errors, and the column densities directly derived from the weakest lines are also subject to these errors. Our model is used to reduce the error by fitting all the other lines at higher $f\lambda$ with a three-parameter curve that approaches the linear regime at low $f\lambda$ according to reasonable assumptions on the distribution and velocity dispersions of the individual absorption components. For internal bulk velocity dispersions of these components $\sigma_h \simeq 9 \text{ km s}^{-1}$, metal lines should reach the unsaturated regime roughly at $W/\lambda \sim \sigma_h/c \simeq 3 \times 10^{-5}$, which is consistent with our measurements shown in Figure 13. For ions other than Fe II and Si II, we assume that their lines follow the same curve, with variations only in the mean column density. If the lines for which our column densities are based on are very weak (i.e., in the unsaturated regime), they are not subject to any model dependence, but if they are saturated then our model assumption of a single curve for all the low-ionization ions is used to extrapolate to low values of $f\lambda$ and correct for the saturation effects.

In general, our derived abundances are slightly higher, although in broad agreement, than previous determinations. Our results for $[\text{Fe II}/\text{H I}] = -1.45 \pm 0.04$, $[\text{Si II}/\text{H I}] = -0.91 \pm 0.03$, $[\text{Cr II}/\text{H I}] = -1.22 \pm 0.12$, $[\text{Mn II}/\text{H I}] = -1.62 \pm 0.19$, $[\text{Ni II}/\text{H I}] = -1.26 \pm 0.05$, and $[\text{Zn II}/\text{H I}] = -0.89 \pm 0.11$ are within 0.5 dex of those reported by Khare et al. (2012) (their Table 5). We can also compare our results with high-resolution studies of smaller numbers of DLAs. Our zinc result is within 3σ of the mean value reported by Pettini (2006), $[\text{Zn}/\text{H}] = -1.2$, at $1.8 < z < 3.5$. To compare with the results of Rafelski et al. (2012), we use our mean DLA redshift $z = 2.59$ in their expression for the evolution of the mean DLA metallicity with redshift, $\langle Z \rangle = (-0.22 \pm 0.03) z_{\text{DLA}} - (0.65 \pm 0.09)$, to find $\langle Z \rangle = -1.22 \pm 0.10$ for their result, which is in agreement within 3σ of our $[\text{Zn II}/\text{H I}]$ value and also with our result for sulfur, $[\text{S II}/\text{H I}] = -0.88 \pm 0.04$, both species being commonly used as metallicity

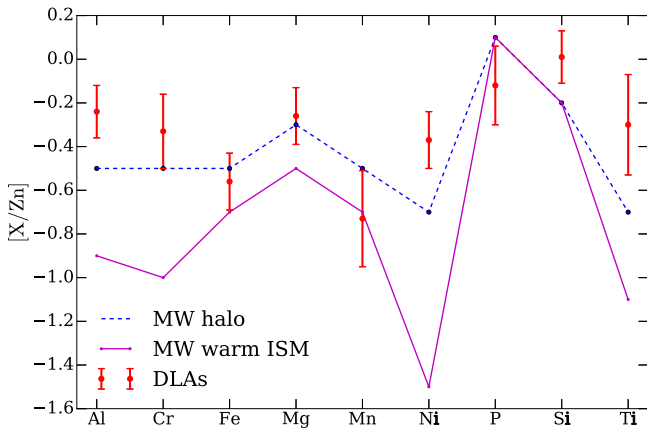


Figure 16. Measurements of relative abundances, $[X/Zn]$, and their uncertainties, for several species compared with the depletion patterns of the Milky Way halo (dashed blue line) and warm ISM (magenta line) gas from Welty et al. (1999).

indicators (Wolfe et al. 2005). Considering Equation (4) in Quirot et al. (2016), $\langle Z \rangle_{\text{DLAs}} = (-0.15 \pm 0.03)_{Z_{\text{DLA}}} - (0.60 \pm 0.13)$, we obtain a H I-weighted mean DLA metallicity of $\langle Z \rangle_{\text{DLAs}} = -0.99 \pm 0.15$, consistent within 1σ with our $[Zn \text{ II}/\text{H I}]$, $[\text{S II}/\text{H I}]$, and $[\text{Si II}/\text{H I}]$ results. Our mean abundances of titanium and phosphorus from Table 2, $[\text{Ti II}/\text{H I}] = -1.19 \pm 0.20$ and $[\text{P II}/\text{H I}] = -1.01 \pm 0.14$, are within 2σ and 3σ , respectively, from a small number of detections reported by Prochaska et al. (2001) (their Table 41), with mean values $[\text{Ti}/\text{H}] \sim -1.45$ (13 data points) and $[\text{P}/\text{H}] \sim -1.42$ (5 data points).

Our measurement of $[\text{Cr II}/\text{Zn II}] = -0.33 \pm 0.17$, which is the ratio normally used to estimate the dust content in DLAs, is in agreement with high-resolution studies of DLAs with abundances $[\text{Zn II}/\text{H I}] \sim -1$ (Pettini et al. 1997; Prochaska & Wolfe 2002; Akerman et al. 2005). We also find $[\text{Fe II}/\text{Zn II}] = -0.56 \pm 0.13$ and $[\text{Ni II}/\text{Zn II}] = -0.37 \pm 0.14$, which agree with the values by, e.g., Prochaska et al. (2001), Pettini (2004), Khare et al. (2004), and Rafelski et al. (2012). Figure 16 illustrates that, in general, our $[X/Zn]$ measurements are in broad agreement with the gas depletion pattern in the halo of the Milky Way reported by Welty et al. (1999), who analyzed the absorption signatures of the Milky Way and LMC gas in the spectra of the supernova SN1987A. The value for $[\text{Fe II}/\text{Zn II}]$ indicates a modest dust depletion effect in DLAs which yields a correction for the abundances (e.g., Vladilo 2002; Vladilo et al. 2011). Silicon is more weakly depleted, and sulfur is extremely weakly depleted, and the values $[\text{Si II}/\text{Fe II}] = 0.54 \pm 0.05$ and $[\text{S II}/\text{Fe II}] = 0.57 \pm 0.06$ are in agreement, for example, with those of Prochaska & Wolfe (2002), Dessauges-Zavadsky et al. (2006), Rafelski et al. (2012), and Berg et al. (2015), when we use our measured value of $[\text{Zn II}/\text{Fe II}] \simeq 0.6$. Ratios of strongly depleted elements, such as $[\text{Cr II}/\text{Fe II}] = 0.23 \pm 0.12$ and $[\text{Mn II}/\text{Fe II}] = -0.17 \pm 0.19$, are also in agreement with various high-resolution studies (e.g., Dessauges-Zavadsky et al. 2006).

Adding the column densities of neutral and singly ionized nitrogen, our measured ratios of $[\text{N}/\text{S II}] = -0.79 \pm 0.08$ and $[\text{N}/\text{Si II}] = -0.76 \pm 0.08$ agree with the results found for evolved DLAs, $[\text{N}/\alpha] \sim -0.7$ (Pettini et al. 2002; Prochaska

& Wolfe 2002; Centuri3n et al. 2003; Petitjean et al. 2008; Zafar et al. 2014).

7.3. Doubly Ionized Species

On the intermediate-ionization species, our mean measured ratio for $[\text{Al III}/\text{Al II}] = -0.86 \pm 0.03$ is in good agreement with the results of Vladilo et al. (2001), who reported this ratio to vary from -0.2 to -1.2 as $\log(N_{\text{H I}}/\text{cm}^{-2})$ varies from 20.3 to 21.0. We find higher values for the ratios $[\text{Si III}/\text{Si II}] = 0.02 \pm 0.04$, $[\text{S III}/\text{S II}] = -0.39 \pm 0.12$, $[\text{Fe III}/\text{Fe II}] = -0.63 \pm 0.10$, and $[\text{C III}/\text{C II}] = 0.67 \pm 0.12$, which indicate that doubly ionized species often have comparable column densities to the singly ionized ones. As explained in Section 6.2, we do not consider the unusually high ratio obtained for the case of carbon to be reliable, because the C III column density depends on an extrapolation of our model to a large value of W/λ that is untested in our data. The other ratios, however, are probably not affected so severely by the systematic modeling uncertainty of saturated lines, and they illustrate the potential of our method to derive mean column densities for various species in DLAs. These results can be further developed and analyzed in the future to probe the photoionization state of DLAs.

7.4. High-ionization Species

We also report in this paper measurements of the mean column density of several lines of high-ionization species. The strongest features are the doublets of C IV and Si IV. The doublet ratios for the total sample are, from Table 5, equal to 1.44 ± 0.02 for C IV and 1.50 ± 0.04 for Si IV. The doublet ratio for both species denotes that the absorbers have a mixture of weak, unsaturated and strong, saturated components, contributing almost equally to the total absorption feature. The fact that this ratio is constant with DLA column density implies that the velocity dispersion, or the mean number of subcomponents, should increase with column density.

Our result for the mean column density of C IV in our DLA sample is $\log N_{\text{C IV}} = 14.40 \pm 0.02$. We can compare that to the results on C IV absorption of DLAs reported by Fox et al. (2007b), who studied a sample of 63 DLAs and found a relation of C IV column density to the DLA metallicity of $\log N_{\text{C IV}} = 15.8 + 1.2 [Z/\text{H}]$. Using our mean metallicity derived from the zinc abundance, $[\text{Zn II}/\text{H I}] = -0.89$ (from our Table 2), there is a remarkably good agreement with our measured mean C IV column density. Our measured Si IV column density is lower than that of C IV by a factor ~ 4 , also in agreement with the results of Fox et al. (2007a). We also obtain for the first time a mean column density of Si IV in DLAs, which is difficult to obtain because of the blend with Fe II lines, and we find a value similar to the column density of Si IV.

The O VI lines at 1031 and 1037 Å are clearly detected, thanks to the elimination in our stacked spectrum of the usual difficulty due to blending with Lyman forest lines. We also detect the much weaker lines of N V at 1238 and 1242 Å. It has been demonstrated that O VI is commonly present in DLAs (Fox et al. 2007b; Rahmani et al. 2010). The mean column density we obtain, $N_{\text{O VI}} = 14.77 \pm 0.03$, should therefore be a typical value in halos hosting DLAs which, as we have seen in Figure 11, does not strongly depend on the H I column density.

For N V, which has nearly optically thin lines, the mean column density we obtain is $N_{\text{N V}} = 13.07 \pm 0.09$, a remarkable measurement given the small number of cases where N V has been detected in individual DLAs (Pettini et al. 1995; Prochaska & Wolfe 2002; Centurión et al. 2003; Fox et al. 2007b, 2009; Henry & Prochaska 2007; Lehner et al. 2008; Petitjean et al. 2008). This result confirms the presence of phases of highly ionized gas around DLAs, and provides observational constraints for clarifying the photoionized or collisionally ionized state of this gas.

7.5. Atomic and Excited Ionized Carbon

We report a detection of the average column of excited C II, or C II*, from the absorption line at 1335.71 Å. We are able to deblend this line from the C II line at 1334.53 Å but, as can be seen in Figure 17, the detection is only made from a slight asymmetry in the blended absorption profile and is therefore subject to systematic errors. Nevertheless, our mean inferred column density of $\log N_{\text{C II}^*} = 13.35 \pm 0.06$ is in rough agreement with the results of Wolfe et al. (2003). Measuring the C II* column density yields estimates of the cooling rate in the DLA gas (Wolfe et al. 2003, 2004).

There is clear evidence for the presence of C I absorption lines in our stacked spectrum, a species that is usually a good tracer of molecular gas (Srianand et al. 2005; Ledoux et al. 2015). These absorption lines are indicated in Figure 8 at $\lambda \simeq 1278, 1329, 1560, \text{ and } 1657 \text{ \AA}$, but they are extremely weak and we have not attempted to measure them.

7.6. Possible Contamination by Broad Absorption Line Systems

Some of the DLAs in the catalog we use might be broad absorption line systems that have been incorrectly identified as DLAs in the low-S/N BOSS spectra. To test the possible influence of this potential contamination, we remove from our total sample all DLAs at a velocity separation $v < 5000 \text{ km s}^{-1}$ from the quasar. There are 3295 such objects, which is $\sim 10\%$ of the total sample. After calculating the stacked spectrum for the remaining systems, we visually confirm that there are no significant differences between this and the total sample spectrum.

8. Summary and Conclusions

We have calculated DLA composite absorption spectra using the DLA catalog of Noterdaeme et al. (2012) of Data Release 12 of BOSS. We have measured the mean equivalent width of 50 absorption lines, 38 from low-ionization species (neutral or singly ionized), four from doubly ionized species, and eight from high-ionization species. In addition, we have measured the total equivalent widths of 13 groups of strongly blended lines. We have performed the same analysis with a subsample of DLAs with individually identified metal lines, called the metal sample, containing about a third of the total sample, which allows for the detection of fainter absorption lines but is not representative of the mean DLA properties. We have divided the two previous samples into five $N_{\text{H I}}$ and five z ranges and have analyzed the dependence of the metal equivalent widths on the DLA hydrogen column density and redshift, in Sections 4 and 5, respectively.

The increase of the mean W with $N_{\text{H I}}$ for the low-ionization lines confirms that these species are closely associated with the self-shielded atomic hydrogen in DLAs. The much weaker dependence of the high-ionization lines on $N_{\text{H I}}$, conversely, demonstrates that these species occur in a different gas phase at lower density that is more extended and surrounds the low-ionization region, in view of the fact that high-ionization lines are ubiquitous in DLAs. The equivalent widths decrease by a factor $\sim 1.1\text{--}1.5$ from redshift $z \sim 2.1$ to $z \sim 3.5$, in general, with the high-ionization species showing a slightly steeper evolution. However, it is not clear whether this possible difference has a physical origin or it is simply driven by systematics.

We have presented a new, simple model to correct for line saturation and derive column densities for all the species we measure, described in Section 6. Our model is quite successful in fitting the available lines of Fe II and Si II with different oscillator strengths, as displayed in Figure 13. The inferred abundances for other species generally agree with the determinations that have been made from high-resolution spectra, when available. We have also been able to measure the mean column density of O VI associated with DLAs, which is otherwise difficult to do because of the superposition with the Ly α forest. For the first time, we obtained also a mean equivalent width and inferred column density for N V and S IV for DLAs. We obtained inferred column densities of several doubly ionized species, like Al III, S III, and Si III, which we believe are generally reliable (although not in the case of C III owing to the required extrapolation of our simple model for line saturation correction), and can be used to test models of photoionization of the various layers surrounding DLAs.

In conclusion, the techniques we have developed here to use stacked DLA absorption spectra demonstrate a promise to explore the photoionization state and abundances of the various heavy element species present in DLAs, with some advantages that can be exploited with very large samples of DLAs even when the resolution and S/N of individual spectra are poor. Further refinement of our simple model for deriving column densities from partly saturated lines, measurement of correlations among different absorption lines, and correlations of the large-scale bias factor of DLAs (Font-Ribera et al. 2012) with metal lines are all promising avenues for future research.

We thank the anonymous referee for a detailed and careful analysis which improved the quality of our work. We are very grateful to Mat Pieri, Hélión du Mas des Bourboux, Hadi Rahmani, Benjamin Racine, Pilar Gil-Pons, Signe Riemer-Sorensen, Xavier Prochaska, Sebastián López, Céline Péroux, George Becker and Max Pettini for their useful comments and suggestions during the different stages of this work. This research was partially supported by the Munich Institute for Astro- and Particle Physics (MIAPP) of the DFG cluster of excellence “Origin and Structure of the universe.” L.M. and J. M. have been partly supported by Spanish grant AYA2012-33938. Funding for SDSS-III has been provided by the Alfred P. Sloan Foundation, the Participating Institutions, the National Science Foundation, and the U.S. Department of Energy Office of Science. The SDSS-III web site is <http://www.sdss3.org/>. SDSS-III is managed by the Astrophysical Research

Table 4
Rest Equivalent Widths of Low-ionization Metal Absorption Lines
for the Two Samples

| Transition | f | Total Sample W (Å) | Metal Sample W (Å) |
|-----------------------|-------|-------------------------|-------------------------|
| Al II λ 1670 | 1.740 | 0.452 ± 0.005 | 0.656 ± 0.005 |
| Al III λ 1854 | 0.559 | 0.117 ± 0.006 | 0.172 ± 0.006 |
| Al III λ 1862 | 0.278 | 0.067 ± 0.006 | 0.096 ± 0.006 |
| C II λ 1036* | 0.118 | 0.418 ± 0.012 | 0.579 ± 0.020 |
| C III λ 977* | 0.757 | 0.646 ± 0.019 | 0.884 ± 0.033 |
| Cr II λ 2056 | 0.103 | 0.028 ± 0.009 | 0.043 ± 0.008 |
| Cr II λ 2066* | 0.051 | 0.034 ± 0.020 | 0.028 ± 0.009 |
| Fe II λ 1081* | 0.013 | 0.030 ± 0.010 | 0.058 ± 0.013 |
| Fe II λ 1096 | 0.032 | 0.086 ± 0.010 | 0.134 ± 0.013 |
| Fe II λ 1125* | 0.016 | 0.069 ± 0.009 | 0.090 ± 0.010 |
| Fe II λ 1144* | 0.083 | 0.166 ± 0.007 | 0.228 ± 0.010 |
| Fe II λ 1608 | 0.058 | 0.228 ± 0.004 | 0.329 ± 0.004 |
| Fe II λ 2249 | 0.002 | 0.016 ± 0.020 | 0.029 ± 0.024 |
| Fe II λ 2260 | 0.002 | 0.034 ± 0.017 | 0.068 ± 0.012 |
| Fe II λ 2344 | 0.114 | 0.520 ± 0.014 | 0.717 ± 0.014 |
| Fe II λ 2374 | 0.031 | 0.282 ± 0.014 | 0.413 ± 0.014 |
| Fe II λ 2382 | 0.320 | 0.669 ± 0.026 | 0.973 ± 0.013 |
| Fe II λ 2586 | 0.069 | 0.462 ± 0.023 | 0.680 ± 0.023 |
| Fe II λ 2600 | 0.239 | 0.722 ± 0.021 | 1.002 ± 0.025 |
| Mg I λ 2852 | 1.830 | 0.231 ± 0.030 | 0.277 ± 0.031 |
| Mg II λ 2796* | 0.616 | 1.149 ± 0.034 | 1.598 ± 0.030 |
| Mg II λ 2803* | 0.306 | 1.067 ± 0.025 | 1.437 ± 0.025 |
| Mn II λ 2576 | 0.361 | 0.040 ± 0.021 | 0.059 ± 0.019 |
| N II λ 1084* | 0.111 | 0.168 ± 0.010 | 0.250 ± 0.011 |
| Ni II λ 1317 | 0.057 | 0.032 ± 0.005 | 0.040 ± 0.005 |
| Ni II λ 1370 | 0.077 | 0.027 ± 0.005 | 0.037 ± 0.005 |
| Ni II λ 1454 | 0.032 | 0.016 ± 0.002 | 0.041 ± 0.003 |
| Ni II λ 1709 | 0.032 | 0.023 ± 0.004 | 0.032 ± 0.004 |
| Ni II λ 1741 | 0.043 | 0.029 ± 0.005 | 0.042 ± 0.005 |
| Ni II λ 1751 | 0.028 | 0.024 ± 0.005 | 0.034 ± 0.005 |
| O I λ 1039* | 0.009 | 0.251 ± 0.013 | 0.343 ± 0.016 |
| O I λ 1302 | 0.048 | 0.460 ± 0.006 | 0.621 ± 0.007 |
| P II λ 1152 | 0.245 | 0.021 ± 0.008 | 0.038 ± 0.010 |
| S II λ 1250* | 0.005 | 0.044 ± 0.005 | 0.064 ± 0.006 |
| S II λ 1253* | 0.011 | 0.063 ± 0.005 | 0.086 ± 0.005 |
| S III λ 1012 | 0.044 | 0.067 ± 0.017 | 0.093 ± 0.022 |
| Si II λ 1020* | 0.017 | 0.096 ± 0.017 | 0.116 ± 0.026 |
| Si II λ 1193* | 0.582 | 0.452 ± 0.006 | 0.617 ± 0.008 |
| Si II λ 1304* | 0.086 | 0.333 ± 0.006 | 0.453 ± 0.007 |
| Si II λ 1526 | 0.133 | 0.443 ± 0.004 | 0.630 ± 0.004 |
| Si II λ 1808 | 0.002 | 0.059 ± 0.006 | 0.088 ± 0.006 |
| Si III λ 1206 | 1.630 | 0.555 ± 0.008 | 0.755 ± 0.007 |

Note. The third and fourth columns give the measured rest equivalent widths in the total and metal samples and their bootstrap errors. All low-ionization lines are included, except for the strongly blended ones that are in Table 1. The doubly ionized aluminum and silicon lines are also included here. The superscript * denotes weakly blended lines with equivalent widths measured from a joint fit in a common window. Figures 17 and 18 in Appendix B display the lines included in each blend.

Table 5
Same as Table 4 for High-ionization Metal Absorption Lines

| Transition | f | Total Sample W (Å) | Metal Sample W (Å) |
|----------------------|-------|-------------------------|-------------------------|
| C IV λ 1548* | 0.190 | 0.429 ± 0.004 | 0.565 ± 0.005 |
| C IV λ 1550* | 0.095 | 0.298 ± 0.003 | 0.394 ± 0.005 |
| N V λ 1238* | 0.156 | 0.023 ± 0.006 | 0.031 ± 0.007 |
| N V λ 1242* | 0.078 | 0.015 ± 0.006 | 0.015 ± 0.007 |
| O VI λ 1031 | 0.133 | 0.331 ± 0.015 | 0.411 ± 0.025 |
| O VI λ 1037* | 0.066 | 0.191 ± 0.011 | 0.256 ± 0.014 |
| Si IV λ 1393 | 0.513 | 0.292 ± 0.004 | 0.400 ± 0.005 |
| Si IV λ 1402 | 0.254 | 0.195 ± 0.004 | 0.270 ± 0.005 |

Consortium for the Participating Institutions of the SDSS-III Collaboration including the University of Arizona, the Brazilian Participation Group, Brookhaven National Laboratory, Carnegie Mellon University, University of Florida, the French Participation Group, the German Participation Group, Harvard University, the Instituto de Astrofísica de Canarias, the Michigan State/Notre Dame/JINA Participation Group, Johns Hopkins University, Lawrence Berkeley National Laboratory, Max Planck Institute for Astrophysics, Max Planck Institute for Extraterrestrial Physics, New Mexico State University, New York University, Ohio State University, Pennsylvania State University, University of Portsmouth, Princeton University, the Spanish Participation Group, University of Tokyo, University of Utah, Vanderbilt University, University of Virginia, University of Washington, and Yale University.

Appendix A Rest Equivalent Width Measurement

This appendix presents the tables for the calculated rest equivalent widths and their uncertainties. Tables 4 and 5 present the values for the low- and high-ionization species in the metal and total samples, respectively. For the case of the five $N_{\text{H I}}$ ranges, we present Tables 6–9, which list the measurements of low- and high-ionization species, in the total and metal samples, respectively. Whenever the convergence of the fitting method is not reached or the measurements present negative values, the equivalent widths are set to zero while the uncertainties remain unchanged. The values for $N_{\text{H I}}$ displayed in the tables are those computed taking the mean column density within the corresponding interval. Tables 10–13 correspond to the same cases for the five redshift bins, \bar{z}_{DLA} . Positions with no values indicate the cases where the corresponding line wavelength is not covered by the spectrum in that redshift bin. The oscillator strengths, f , are those tabulated by Morton (2003) except for the Ni II λ 1317 line, where we use the value measured by Dessauges-Zavadsky et al. (2006).

Appendix B Absorption Line Fitting

Figures 17 and 18 display the result of the profile fits of every absorption feature analyzed in this work.

Table 6
Rest Equivalent Widths of Absorption Low-ionization Lines with Respect to the Hydrogen Column Density for the Total Sample

| $\log(\bar{N}_{\text{H I}}/\text{cm}^{-2})$ Transition | f | 20.06 W (Å) | 20.22 W (Å) | 20.40 W (Å) | 20.65 W (Å) | 21.13 W (Å) |
|---|-------|-------------------|-------------------|-------------------|-------------------|-------------------|
| Al II λ 1670 | 1.740 | 0.278 \pm 0.012 | 0.345 \pm 0.008 | 0.412 \pm 0.011 | 0.526 \pm 0.011 | 0.673 \pm 0.012 |
| Al III λ 1854 | 0.559 | 0.076 \pm 0.009 | 0.076 \pm 0.010 | 0.105 \pm 0.009 | 0.146 \pm 0.007 | 0.173 \pm 0.010 |
| Al III λ 1862 | 0.278 | 0.039 \pm 0.011 | 0.045 \pm 0.010 | 0.060 \pm 0.010 | 0.085 \pm 0.008 | 0.097 \pm 0.008 |
| C II λ 1036 | 0.118 | 0.260 \pm 0.022 | 0.318 \pm 0.022 | 0.356 \pm 0.021 | 0.481 \pm 0.022 | 0.613 \pm 0.024 |
| C III λ 977 | 0.757 | 0.553 \pm 0.048 | 0.699 \pm 0.042 | 0.551 \pm 0.048 | 0.701 \pm 0.043 | 0.811 \pm 0.045 |
| Cr II λ 2056 | 0.103 | 0.000 \pm 0.014 | 0.000 \pm 0.014 | 0.022 \pm 0.015 | 0.043 \pm 0.013 | 0.079 \pm 0.013 |
| Cr II λ 2066 | 0.051 | 0.011 \pm 0.010 | 0.094 \pm 0.089 | 0.016 \pm 0.011 | 0.024 \pm 0.012 | 0.042 \pm 0.012 |
| Fe II λ 1081 | 0.013 | 0.030 \pm 0.018 | 0.000 \pm 0.017 | 0.005 \pm 0.018 | 0.027 \pm 0.019 | 0.087 \pm 0.015 |
| Fe II λ 1096 | 0.032 | 0.025 \pm 0.018 | 0.057 \pm 0.018 | 0.064 \pm 0.017 | 0.096 \pm 0.017 | 0.179 \pm 0.019 |
| Fe II λ 1125 | 0.016 | 0.056 \pm 0.015 | 0.015 \pm 0.013 | 0.048 \pm 0.017 | 0.076 \pm 0.014 | 0.154 \pm 0.015 |
| Fe II λ 1144 | 0.083 | 0.096 \pm 0.015 | 0.101 \pm 0.013 | 0.150 \pm 0.013 | 0.184 \pm 0.013 | 0.286 \pm 0.012 |
| Fe II λ 1608 | 0.058 | 0.110 \pm 0.007 | 0.147 \pm 0.006 | 0.186 \pm 0.006 | 0.264 \pm 0.007 | 0.414 \pm 0.009 |
| Fe II λ 2249 | 0.002 | 0.033 \pm 0.020 | 0.028 \pm 0.021 | 0.000 \pm 0.020 | 0.031 \pm 0.015 | 0.003 \pm 0.068 |
| Fe II λ 2260 | 0.002 | 0.011 \pm 0.029 | 0.018 \pm 0.021 | 0.027 \pm 0.020 | 0.050 \pm 0.017 | 0.049 \pm 0.055 |
| Fe II λ 2344 | 0.114 | 0.279 \pm 0.027 | 0.342 \pm 0.026 | 0.463 \pm 0.026 | 0.621 \pm 0.023 | 0.816 \pm 0.024 |
| Fe II λ 2374 | 0.031 | 0.101 \pm 0.027 | 0.158 \pm 0.028 | 0.264 \pm 0.023 | 0.315 \pm 0.020 | 0.544 \pm 0.022 |
| Fe II λ 2382 | 0.320 | 0.441 \pm 0.024 | 0.406 \pm 0.101 | 0.616 \pm 0.072 | 0.778 \pm 0.023 | 1.041 \pm 0.023 |
| Fe II λ 2586 | 0.069 | 0.212 \pm 0.046 | 0.300 \pm 0.035 | 0.414 \pm 0.062 | 0.484 \pm 0.031 | 0.846 \pm 0.030 |
| Fe II λ 2600 | 0.239 | 0.451 \pm 0.035 | 0.529 \pm 0.040 | 0.644 \pm 0.060 | 0.911 \pm 0.040 | 0.997 \pm 0.042 |
| Mg I λ 2852 | 1.830 | 0.185 \pm 0.053 | 0.083 \pm 0.065 | 0.100 \pm 0.048 | 0.282 \pm 0.062 | 0.364 \pm 0.036 |
| Mg II λ 2796 | 0.616 | 0.700 \pm 0.080 | 1.014 \pm 0.048 | 1.256 \pm 0.078 | 1.258 \pm 0.095 | 1.500 \pm 0.050 |
| Mg II λ 2803 | 0.306 | 0.760 \pm 0.053 | 0.793 \pm 0.063 | 1.062 \pm 0.048 | 1.215 \pm 0.042 | 1.491 \pm 0.045 |
| Mn II λ 2576 | 0.361 | 0.017 \pm 0.033 | 0.001 \pm 0.039 | 0.004 \pm 0.034 | 0.051 \pm 0.056 | 0.134 \pm 0.025 |
| N II λ 1084 | 0.111 | 0.103 \pm 0.018 | 0.127 \pm 0.019 | 0.142 \pm 0.020 | 0.201 \pm 0.016 | 0.258 \pm 0.020 |
| Ni II λ 1317 | 0.057 | 0.029 \pm 0.011 | 0.018 \pm 0.010 | 0.029 \pm 0.011 | 0.031 \pm 0.012 | 0.055 \pm 0.011 |
| Ni II λ 1370 | 0.077 | 0.002 \pm 0.009 | 0.015 \pm 0.009 | 0.021 \pm 0.010 | 0.021 \pm 0.009 | 0.067 \pm 0.008 |
| Ni II λ 1454 | 0.032 | 0.000 \pm 0.004 | 0.010 \pm 0.005 | 0.011 \pm 0.004 | 0.022 \pm 0.004 | 0.043 \pm 0.004 |
| Ni II λ 1709 | 0.032 | 0.012 \pm 0.009 | 0.008 \pm 0.007 | 0.011 \pm 0.008 | 0.023 \pm 0.006 | 0.051 \pm 0.007 |
| Ni II λ 1741 | 0.043 | 0.009 \pm 0.008 | 0.015 \pm 0.008 | 0.016 \pm 0.008 | 0.030 \pm 0.006 | 0.070 \pm 0.006 |
| Ni II λ 1751 | 0.028 | 0.012 \pm 0.007 | 0.016 \pm 0.008 | 0.012 \pm 0.008 | 0.029 \pm 0.006 | 0.050 \pm 0.007 |
| O I λ 1039 | 0.009 | 0.114 \pm 0.029 | 0.163 \pm 0.022 | 0.211 \pm 0.024 | 0.287 \pm 0.025 | 0.414 \pm 0.025 |
| O I λ 1302 | 0.048 | 0.288 \pm 0.011 | 0.362 \pm 0.010 | 0.429 \pm 0.012 | 0.543 \pm 0.012 | 0.654 \pm 0.013 |
| P II λ 1152 | 0.245 | 0.010 \pm 0.015 | 0.027 \pm 0.013 | 0.025 \pm 0.015 | 0.030 \pm 0.013 | 0.000 \pm 0.016 |
| S II λ 1250 | 0.005 | 0.014 \pm 0.012 | 0.023 \pm 0.010 | 0.041 \pm 0.011 | 0.042 \pm 0.011 | 0.092 \pm 0.010 |
| S II λ 1253 | 0.011 | 0.039 \pm 0.011 | 0.022 \pm 0.010 | 0.046 \pm 0.010 | 0.081 \pm 0.009 | 0.116 \pm 0.010 |
| S III λ 1012 | 0.044 | 0.074 \pm 0.032 | 0.020 \pm 0.031 | 0.065 \pm 0.037 | 0.029 \pm 0.037 | 0.121 \pm 0.036 |
| Si II λ 1020 | 0.017 | 0.000 \pm 0.032 | 0.093 \pm 0.031 | 0.076 \pm 0.032 | 0.048 \pm 0.033 | 0.240 \pm 0.029 |
| Si II λ 1193 | 0.582 | 0.333 \pm 0.018 | 0.362 \pm 0.010 | 0.433 \pm 0.014 | 0.529 \pm 0.012 | 0.605 \pm 0.014 |
| Si II λ 1304 | 0.086 | 0.177 \pm 0.012 | 0.251 \pm 0.010 | 0.315 \pm 0.011 | 0.390 \pm 0.010 | 0.513 \pm 0.012 |
| Si II λ 1526 | 0.133 | 0.275 \pm 0.008 | 0.337 \pm 0.008 | 0.407 \pm 0.008 | 0.514 \pm 0.009 | 0.656 \pm 0.010 |
| Si II λ 1808 | 0.002 | 0.023 \pm 0.010 | 0.019 \pm 0.009 | 0.042 \pm 0.010 | 0.061 \pm 0.009 | 0.135 \pm 0.009 |
| Si III λ 1206 | 1.630 | 0.472 \pm 0.016 | 0.517 \pm 0.014 | 0.586 \pm 0.015 | 0.614 \pm 0.014 | 0.612 \pm 0.017 |

Note. The values for $N_{\text{H I}}$ are the mean values of each range, for which values of the rest-frame equivalent width W with its error are given for each line.

Table 7
Rest Equivalent Widths of Absorption High-ionization Lines with Respect to the Hydrogen Column Density for the Total Sample

| $\log(N_{\text{H I}}/\text{cm}^{-2})$ Transition | f | 20.06 W (Å) | 20.22 W (Å) | 20.40 W (Å) | 20.65 W (Å) | 21.13 W (Å) |
|---|-------|-------------------|-------------------|-------------------|-------------------|-------------------|
| C IV λ 1548 | 0.190 | 0.375 ± 0.010 | 0.410 ± 0.008 | 0.429 ± 0.009 | 0.459 ± 0.010 | 0.471 ± 0.010 |
| C IV λ 1550 | 0.095 | 0.263 ± 0.009 | 0.291 ± 0.007 | 0.296 ± 0.007 | 0.319 ± 0.008 | 0.319 ± 0.008 |
| N V λ 1238 | 0.156 | 0.024 ± 0.013 | 0.061 ± 0.013 | 0.018 ± 0.012 | 0.022 ± 0.012 | 0.000 ± 0.011 |
| N V λ 1242 | 0.078 | 0.010 ± 0.013 | 0.025 ± 0.014 | 0.028 ± 0.012 | 0.018 ± 0.013 | 0.000 ± 0.013 |
| O VI λ 1031 | 0.133 | 0.250 ± 0.028 | 0.281 ± 0.028 | 0.305 ± 0.028 | 0.323 ± 0.025 | 0.433 ± 0.030 |
| O VI λ 1037 | 0.066 | 0.156 ± 0.021 | 0.154 ± 0.024 | 0.122 ± 0.022 | 0.200 ± 0.021 | 0.265 ± 0.022 |
| Si IV λ 1393 | 0.513 | 0.246 ± 0.009 | 0.272 ± 0.009 | 0.286 ± 0.008 | 0.318 ± 0.008 | 0.338 ± 0.010 |
| Si IV λ 1402 | 0.254 | 0.172 ± 0.008 | 0.191 ± 0.008 | 0.179 ± 0.008 | 0.208 ± 0.008 | 0.227 ± 0.009 |

Table 8
Rest Equivalent Widths of Absorption Low-ionization Lines with Respect to the Hydrogen Column Density for the Metal Sample

| $\log(N_{\text{H I}}/\text{cm}^{-2})$ Transition | f | 20.06 W (Å) | 20.22 W (Å) | 20.40 W (Å) | 20.65 W (Å) | 21.13 W (Å) |
|---|-------|-------------------|-------------------|-------------------|-------------------|-------------------|
| Al II λ 1670 | 1.740 | 0.510 ± 0.014 | 0.561 ± 0.012 | 0.598 ± 0.011 | 0.682 ± 0.011 | 0.825 ± 0.012 |
| Al III λ 1854 | 0.559 | 0.143 ± 0.014 | 0.139 ± 0.009 | 0.145 ± 0.009 | 0.184 ± 0.008 | 0.217 ± 0.009 |
| Al III λ 1862 | 0.278 | 0.082 ± 0.014 | 0.085 ± 0.011 | 0.079 ± 0.010 | 0.104 ± 0.009 | 0.114 ± 0.009 |
| C II λ 1036 | 0.118 | 0.505 ± 0.033 | 0.513 ± 0.030 | 0.504 ± 0.024 | 0.595 ± 0.022 | 0.731 ± 0.025 |
| C III λ 977 | 0.757 | 1.053 ± 0.077 | 1.229 ± 0.074 | 1.156 ± 0.071 | 1.300 ± 0.082 | 1.489 ± 0.097 |
| Cr II λ 2056 | 0.103 | 0.017 ± 0.021 | 0.015 ± 0.017 | 0.018 ± 0.014 | 0.043 ± 0.014 | 0.093 ± 0.012 |
| Cr II λ 2066 | 0.051 | 0.011 ± 0.007 | 0.013 ± 0.014 | 0.011 ± 0.018 | 0.022 ± 0.012 | 0.057 ± 0.016 |
| Fe II λ 1081 | 0.013 | 0.024 ± 0.022 | 0.039 ± 0.023 | 0.023 ± 0.021 | 0.063 ± 0.019 | 0.097 ± 0.015 |
| Fe II λ 1096 | 0.032 | 0.083 ± 0.024 | 0.098 ± 0.023 | 0.098 ± 0.021 | 0.121 ± 0.019 | 0.216 ± 0.016 |
| Fe II λ 1125 | 0.016 | 0.040 ± 0.022 | 0.038 ± 0.016 | 0.075 ± 0.016 | 0.088 ± 0.015 | 0.169 ± 0.016 |
| Fe II λ 1144 | 0.083 | 0.151 ± 0.019 | 0.156 ± 0.016 | 0.205 ± 0.016 | 0.220 ± 0.015 | 0.331 ± 0.014 |
| Fe II λ 1608 | 0.058 | 0.192 ± 0.010 | 0.231 ± 0.009 | 0.268 ± 0.008 | 0.336 ± 0.008 | 0.502 ± 0.008 |
| Fe II λ 2249 | 0.002 | 0.042 ± 0.025 | 0.042 ± 0.022 | 0.023 ± 0.024 | 0.043 ± 0.018 | 0.006 ± 0.077 |
| Fe II λ 2260 | 0.002 | 0.029 ± 0.028 | 0.060 ± 0.022 | 0.040 ± 0.019 | 0.062 ± 0.018 | 0.120 ± 0.017 |
| Fe II λ 2344 | 0.114 | 0.447 ± 0.033 | 0.519 ± 0.037 | 0.640 ± 0.030 | 0.783 ± 0.020 | 0.989 ± 0.022 |
| Fe II λ 2374 | 0.031 | 0.168 ± 0.032 | 0.265 ± 0.042 | 0.364 ± 0.026 | 0.435 ± 0.023 | 0.657 ± 0.020 |
| Fe II λ 2382 | 0.320 | 0.686 ± 0.030 | 0.794 ± 0.029 | 0.922 ± 0.027 | 1.016 ± 0.024 | 1.230 ± 0.022 |
| Fe II λ 2586 | 0.069 | 0.433 ± 0.048 | 0.484 ± 0.050 | 0.601 ± 0.067 | 0.676 ± 0.030 | 0.984 ± 0.031 |
| Fe II λ 2600 | 0.239 | 0.719 ± 0.037 | 0.818 ± 0.047 | 0.884 ± 0.081 | 1.108 ± 0.051 | 1.261 ± 0.052 |
| Mg I λ 2852 | 1.830 | 0.263 ± 0.077 | 0.202 ± 0.051 | 0.231 ± 0.056 | 0.306 ± 0.069 | 0.394 ± 0.040 |
| Mg II λ 2796 | 0.616 | 1.168 ± 0.159 | 1.519 ± 0.057 | 1.580 ± 0.048 | 1.746 ± 0.050 | 1.812 ± 0.049 |
| Mg II λ 2803 | 0.306 | 1.142 ± 0.088 | 1.210 ± 0.068 | 1.450 ± 0.053 | 1.482 ± 0.042 | 1.733 ± 0.047 |
| Mn II λ 2576 | 0.361 | 0.003 ± 0.042 | 0.037 ± 0.035 | 0.000 ± 0.043 | 0.040 ± 0.035 | 0.147 ± 0.027 |
| N II λ 1084 | 0.111 | 0.183 ± 0.023 | 0.224 ± 0.025 | 0.211 ± 0.022 | 0.268 ± 0.019 | 0.311 ± 0.019 |
| Ni II λ 1317 | 0.057 | 0.051 ± 0.014 | 0.028 ± 0.012 | 0.032 ± 0.014 | 0.032 ± 0.012 | 0.057 ± 0.010 |
| Ni II λ 1370 | 0.077 | 0.017 ± 0.012 | 0.029 ± 0.012 | 0.035 ± 0.009 | 0.020 ± 0.010 | 0.071 ± 0.008 |
| Ni II λ 1454 | 0.032 | 0.000 ± 0.006 | 0.020 ± 0.005 | 0.011 ± 0.005 | 0.021 ± 0.004 | 0.042 ± 0.004 |
| Ni II λ 1709 | 0.032 | 0.012 ± 0.013 | 0.018 ± 0.009 | 0.017 ± 0.008 | 0.031 ± 0.008 | 0.059 ± 0.006 |
| Ni II λ 1741 | 0.043 | 0.019 ± 0.011 | 0.019 ± 0.009 | 0.032 ± 0.008 | 0.040 ± 0.008 | 0.084 ± 0.007 |
| Ni II λ 1751 | 0.028 | 0.023 ± 0.011 | 0.021 ± 0.011 | 0.020 ± 0.009 | 0.031 ± 0.007 | 0.063 ± 0.007 |
| O I λ 1039 | 0.009 | 0.245 ± 0.034 | 0.283 ± 0.028 | 0.269 ± 0.026 | 0.369 ± 0.025 | 0.499 ± 0.023 |
| O I λ 1302 | 0.048 | 0.471 ± 0.017 | 0.533 ± 0.013 | 0.573 ± 0.013 | 0.658 ± 0.014 | 0.771 ± 0.013 |
| P II λ 1152 | 0.245 | 0.051 ± 0.020 | 0.031 ± 0.018 | 0.024 ± 0.018 | 0.028 ± 0.015 | 0.064 ± 0.018 |
| S II λ 1250 | 0.005 | 0.037 ± 0.014 | 0.034 ± 0.012 | 0.063 ± 0.014 | 0.051 ± 0.012 | 0.109 ± 0.013 |
| S II λ 1253 | 0.011 | 0.038 ± 0.013 | 0.060 ± 0.011 | 0.070 ± 0.014 | 0.088 ± 0.010 | 0.140 ± 0.011 |
| S III λ 1012 | 0.044 | 0.131 ± 0.060 | 0.068 ± 0.046 | 0.090 ± 0.043 | 0.020 ± 0.044 | 0.149 ± 0.042 |
| Si II λ 1020 | 0.017 | 0.059 ± 0.050 | 0.134 ± 0.045 | 0.095 ± 0.040 | 0.081 ± 0.038 | 0.200 ± 0.033 |
| Si II λ 1193 | 0.582 | 0.506 ± 0.022 | 0.546 ± 0.014 | 0.591 ± 0.015 | 0.645 ± 0.014 | 0.728 ± 0.013 |
| Si II λ 1304 | 0.086 | 0.316 ± 0.016 | 0.372 ± 0.010 | 0.414 ± 0.013 | 0.478 ± 0.011 | 0.595 ± 0.012 |
| Si II λ 1526 | 0.133 | 0.477 ± 0.012 | 0.532 ± 0.010 | 0.579 ± 0.009 | 0.655 ± 0.009 | 0.793 ± 0.010 |
| Si II λ 1808 | 0.002 | 0.037 ± 0.014 | 0.038 ± 0.012 | 0.061 ± 0.010 | 0.084 ± 0.008 | 0.167 ± 0.008 |
| Si III λ 1206 | 1.630 | 0.740 ± 0.018 | 0.757 ± 0.018 | 0.769 ± 0.015 | 0.751 ± 0.015 | 0.762 ± 0.019 |

Note. The values for $N_{\text{H I}}$ are the mean values of each range, for which values of the rest-frame equivalent width W with its error are given for each line.

Table 9
Rest Equivalent Widths of Absorption High-ionization Lines with Respect to the Hydrogen Column Density for the Metal Sample

| $\log(\bar{N}_{\text{H I}}/\text{cm}^{-2})$ Transition | f | 20.06 W (Å) | 20.22 W (Å) | 20.40 W (Å) | 20.65 W (Å) | 21.13 W (Å) |
|---|-------|-------------------|-------------------|-------------------|-------------------|-------------------|
| C IV λ 1548 | 0.190 | 0.575 ± 0.017 | 0.585 ± 0.013 | 0.559 ± 0.012 | 0.558 ± 0.011 | 0.553 ± 0.010 |
| C IV λ 1550 | 0.095 | 0.409 ± 0.014 | 0.419 ± 0.011 | 0.388 ± 0.010 | 0.391 ± 0.009 | 0.373 ± 0.008 |
| N V λ 1238 | 0.156 | 0.045 ± 0.019 | 0.077 ± 0.015 | 0.020 ± 0.016 | 0.044 ± 0.012 | 0.000 ± 0.013 |
| N V λ 1242 | 0.078 | 0.011 ± 0.017 | 0.023 ± 0.016 | 0.029 ± 0.013 | 0.021 ± 0.014 | 0.000 ± 0.014 |
| O VI λ 1031 | 0.133 | 0.410 ± 0.037 | 0.398 ± 0.036 | 0.385 ± 0.032 | 0.396 ± 0.030 | 0.481 ± 0.031 |
| O VI λ 1037 | 0.066 | 0.260 ± 0.028 | 0.270 ± 0.031 | 0.204 ± 0.023 | 0.256 ± 0.021 | 0.310 ± 0.023 |
| Si IV λ 1393 | 0.513 | 0.406 ± 0.013 | 0.410 ± 0.011 | 0.391 ± 0.010 | 0.395 ± 0.010 | 0.399 ± 0.010 |
| Si IV λ 1402 | 0.254 | 0.276 ± 0.012 | 0.291 ± 0.012 | 0.253 ± 0.009 | 0.263 ± 0.009 | 0.269 ± 0.008 |

Table 10
Rest Equivalent Widths of Absorption Low-ionization Lines with Respect to the Redshift for the Total Sample

| \bar{z}_{DLA} Transition | f | 2.12 W (Å) | 2.32 W (Å) | 2.54 W (Å) | 2.84 W (Å) | 3.50 W (Å) |
|--------------------------------------|-------|-------------------|-------------------|-------------------|-------------------|-------------------|
| Al II λ 1670 | 1.740 | 0.490 ± 0.009 | 0.474 ± 0.012 | 0.462 ± 0.010 | 0.422 ± 0.011 | 0.296 ± 0.010 |
| Al III λ 1854 | 0.559 | 0.151 ± 0.008 | 0.133 ± 0.009 | 0.116 ± 0.009 | 0.090 ± 0.011 | 0.067 ± 0.011 |
| Al III λ 1862 | 0.278 | 0.091 ± 0.009 | 0.077 ± 0.009 | 0.064 ± 0.009 | 0.054 ± 0.012 | 0.035 ± 0.011 |
| C III λ 977 | 0.757 | ... | ... | 0.809 ± 0.118 | 0.655 ± 0.034 | 0.607 ± 0.022 |
| Cr II λ 2056 | 0.103 | 0.028 ± 0.012 | 0.029 ± 0.013 | 0.030 ± 0.012 | 0.026 ± 0.017 | 0.023 ± 0.022 |
| Fe II λ 1081 | 0.013 | ... | 0.058 ± 0.025 | 0.043 ± 0.016 | 0.028 ± 0.015 | 0.010 ± 0.015 |
| Fe II λ 1096 | 0.032 | ... | 0.084 ± 0.021 | 0.100 ± 0.016 | 0.076 ± 0.017 | 0.047 ± 0.015 |
| Fe II λ 1608 | 0.058 | 0.254 ± 0.006 | 0.239 ± 0.009 | 0.228 ± 0.008 | 0.204 ± 0.009 | 0.133 ± 0.007 |
| Fe II λ 2249 | 0.002 | 0.038 ± 0.017 | 0.035 ± 0.016 | 0.040 ± 0.016 | 0.018 ± 0.021 | ... |
| Fe II λ 2260 | 0.002 | 0.051 ± 0.018 | 0.039 ± 0.016 | 0.046 ± 0.017 | 0.053 ± 0.021 | 0.056 ± 0.043 |
| Fe II λ 2344 | 0.114 | 0.553 ± 0.019 | 0.542 ± 0.019 | 0.517 ± 0.019 | 0.481 ± 0.024 | 0.392 ± 0.070 |
| Fe II λ 2374 | 0.031 | 0.332 ± 0.019 | 0.315 ± 0.019 | 0.298 ± 0.020 | 0.233 ± 0.030 | 0.148 ± 0.067 |
| Fe II λ 2382 | 0.320 | 0.756 ± 0.020 | 0.742 ± 0.021 | 0.717 ± 0.019 | 0.667 ± 0.028 | 0.516 ± 0.075 |
| Fe II λ 2586 | 0.069 | 0.534 ± 0.025 | 0.505 ± 0.025 | 0.456 ± 0.029 | 0.333 ± 0.048 | ... |
| Fe II λ 2600 | 0.239 | 0.768 ± 0.024 | 0.748 ± 0.025 | 0.682 ± 0.027 | 0.556 ± 0.081 | ... |
| Mg I λ 2852 | 1.830 | 0.228 ± 0.029 | 0.205 ± 0.038 | 0.329 ± 0.059 | ... | ... |
| Mg II λ 2796 | 0.616 | 1.267 ± 0.028 | 1.168 ± 0.034 | 1.117 ± 0.032 | ... | ... |
| Mg II λ 2803 | 0.306 | 1.117 ± 0.027 | 1.046 ± 0.034 | 1.127 ± 0.042 | ... | ... |
| Mn II λ 2576 | 0.361 | 0.056 ± 0.025 | 0.041 ± 0.023 | 0.035 ± 0.025 | 0.017 ± 0.050 | ... |
| N II λ 1084 | 0.111 | ... | 0.207 ± 0.025 | 0.187 ± 0.016 | 0.174 ± 0.013 | 0.105 ± 0.014 |
| Ni II λ 1317 | 0.057 | 0.036 ± 0.009 | 0.041 ± 0.010 | 0.031 ± 0.009 | 0.019 ± 0.011 | 0.003 ± 0.015 |
| Ni II λ 1370 | 0.077 | 0.019 ± 0.008 | 0.035 ± 0.010 | 0.023 ± 0.009 | 0.019 ± 0.008 | 0.018 ± 0.010 |
| Ni II λ 1709 | 0.032 | 0.020 ± 0.007 | 0.029 ± 0.008 | 0.019 ± 0.007 | 0.021 ± 0.009 | 0.015 ± 0.007 |
| Ni II λ 1741 | 0.043 | 0.034 ± 0.007 | 0.038 ± 0.008 | 0.023 ± 0.006 | 0.027 ± 0.009 | 0.017 ± 0.008 |
| Ni II λ 1751 | 0.028 | 0.026 ± 0.007 | 0.033 ± 0.009 | 0.027 ± 0.008 | 0.020 ± 0.010 | 0.010 ± 0.009 |
| O I λ 1302 | 0.048 | 0.445 ± 0.012 | 0.412 ± 0.013 | 0.403 ± 0.011 | 0.385 ± 0.012 | 0.297 ± 0.016 |
| S II λ 1250 | 0.005 | 0.031 ± 0.010 | 0.045 ± 0.010 | 0.045 ± 0.010 | 0.019 ± 0.013 | 0.037 ± 0.015 |
| S II λ 1253 | 0.011 | 0.067 ± 0.007 | 0.057 ± 0.009 | 0.055 ± 0.010 | 0.053 ± 0.010 | 0.040 ± 0.016 |
| S III λ 1012 | 0.044 | ... | ... | 0.060 ± 0.042 | 0.064 ± 0.026 | 0.045 ± 0.021 |
| Si II λ 1020 | 0.017 | ... | ... | 0.109 ± 0.030 | 0.075 ± 0.023 | 0.088 ± 0.021 |
| Si II λ 1304 | 0.086 | 0.378 ± 0.011 | 0.352 ± 0.012 | 0.327 ± 0.011 | 0.322 ± 0.011 | 0.224 ± 0.016 |
| Si II λ 1526 | 0.133 | 0.469 ± 0.007 | 0.461 ± 0.009 | 0.440 ± 0.008 | 0.428 ± 0.010 | 0.289 ± 0.008 |
| Si II λ 1808 | 0.002 | 0.076 ± 0.008 | 0.071 ± 0.009 | 0.058 ± 0.008 | 0.050 ± 0.011 | 0.013 ± 0.011 |
| Si III λ 1206 | 1.630 | 0.576 ± 0.013 | 0.541 ± 0.011 | 0.540 ± 0.011 | 0.529 ± 0.015 | 0.371 ± 0.019 |

Note. The values for \bar{z}_{DLA} are the mean values of each range, for which values of the rest-frame equivalent width W with its error are given for each line.

Table 11
Rest Equivalent Widths of Absorption High-ionization Lines with Respect to the Redshift for the Total Sample

| \bar{z}_{DLA} Transition | f | 2.12 W (Å) | 2.32 W (Å) | 2.54 W (Å) | 2.84 W (Å) | 3.50 W (Å) |
|--------------------------------------|-------|-------------------|-------------------|-------------------|-------------------|-------------------|
| C IV λ 1548 | 0.190 | 0.480 \pm 0.008 | 0.452 \pm 0.009 | 0.418 \pm 0.008 | 0.377 \pm 0.009 | 0.264 \pm 0.008 |
| C IV λ 1550 | 0.095 | 0.361 \pm 0.007 | 0.341 \pm 0.007 | 0.307 \pm 0.007 | 0.269 \pm 0.009 | 0.195 \pm 0.008 |
| N V λ 1238 | 0.156 | 0.029 \pm 0.010 | 0.008 \pm 0.012 | 0.025 \pm 0.011 | 0.030 \pm 0.013 | 0.005 \pm 0.019 |
| N V λ 1242 | 0.078 | 0.006 \pm 0.010 | 0.011 \pm 0.011 | 0.016 \pm 0.012 | 0.011 \pm 0.015 | 0.014 \pm 0.021 |
| Si IV λ 1393 | 0.513 | 0.325 \pm 0.008 | 0.298 \pm 0.008 | 0.272 \pm 0.008 | 0.263 \pm 0.007 | 0.180 \pm 0.011 |
| Si IV λ 1402 | 0.254 | 0.220 \pm 0.008 | 0.197 \pm 0.008 | 0.180 \pm 0.007 | 0.169 \pm 0.008 | 0.118 \pm 0.010 |

Table 12
Rest Equivalent Widths of Absorption Low-ionization Lines with Respect to the Redshift for the Metal Sample

| \bar{z}_{DLA} Transition | f | 2.12 W (Å) | 2.32 W (Å) | 2.54 W (Å) | 2.84 W (Å) | 3.50 W (Å) |
|--------------------------------------|-------|-------------------|-------------------|-------------------|-------------------|-------------------|
| Al II λ 1670 | 1.740 | 0.671 \pm 0.009 | 0.666 \pm 0.012 | 0.666 \pm 0.012 | 0.655 \pm 0.015 | 0.564 \pm 0.014 |
| Al III λ 1854 | 0.559 | 0.206 \pm 0.009 | 0.198 \pm 0.010 | 0.169 \pm 0.010 | 0.140 \pm 0.012 | 0.128 \pm 0.011 |
| Al III λ 1862 | 0.278 | 0.119 \pm 0.011 | 0.109 \pm 0.011 | 0.097 \pm 0.010 | 0.080 \pm 0.012 | 0.061 \pm 0.010 |
| C III λ 977 | 0.757 | ... | ... | 1.198 \pm 0.159 | 0.904 \pm 0.040 | 0.896 \pm 0.031 |
| Cr II λ 2056 | 0.103 | 0.031 \pm 0.015 | 0.047 \pm 0.014 | 0.047 \pm 0.013 | 0.035 \pm 0.017 | 0.056 \pm 0.021 |
| Fe II λ 1081 | 0.013 | ... | 0.082 \pm 0.027 | 0.071 \pm 0.017 | 0.031 \pm 0.018 | 0.029 \pm 0.016 |
| Fe II λ 1096 | 0.032 | ... | 0.116 \pm 0.021 | 0.136 \pm 0.018 | 0.132 \pm 0.019 | 0.090 \pm 0.021 |
| Fe II λ 1608 | 0.058 | 0.341 \pm 0.008 | 0.330 \pm 0.012 | 0.335 \pm 0.010 | 0.309 \pm 0.011 | 0.257 \pm 0.009 |
| Fe II λ 2249 | 0.002 | 0.053 \pm 0.021 | 0.056 \pm 0.017 | 0.056 \pm 0.018 | 0.042 \pm 0.022 | ... |
| Fe II λ 2260 | 0.002 | 0.073 \pm 0.021 | 0.061 \pm 0.018 | 0.068 \pm 0.017 | 0.074 \pm 0.024 | 0.039 \pm 0.034 |
| Fe II λ 2344 | 0.114 | 0.750 \pm 0.020 | 0.751 \pm 0.019 | 0.737 \pm 0.021 | 0.715 \pm 0.026 | 0.583 \pm 0.086 |
| Fe II λ 2374 | 0.031 | 0.451 \pm 0.021 | 0.438 \pm 0.019 | 0.443 \pm 0.022 | 0.382 \pm 0.030 | 0.254 \pm 0.079 |
| Fe II λ 2382 | 0.320 | 1.016 \pm 0.021 | 1.020 \pm 0.022 | 1.004 \pm 0.021 | 0.966 \pm 0.030 | 0.786 \pm 0.098 |
| Fe II λ 2586 | 0.069 | 0.716 \pm 0.027 | 0.713 \pm 0.026 | 0.674 \pm 0.029 | 0.619 \pm 0.058 | ... |
| Fe II λ 2600 | 0.239 | 1.048 \pm 0.026 | 1.049 \pm 0.024 | 0.992 \pm 0.030 | 0.844 \pm 0.129 | ... |
| Mg I λ 2852 | 1.830 | 0.295 \pm 0.035 | 0.282 \pm 0.040 | 0.389 \pm 0.065 | ... | ... |
| Mg II λ 2796 | 0.616 | 1.688 \pm 0.029 | 1.656 \pm 0.037 | 1.604 \pm 0.042 | ... | ... |
| Mg II λ 2803 | 0.306 | 1.501 \pm 0.029 | 1.493 \pm 0.033 | 1.550 \pm 0.045 | ... | ... |
| Mn II λ 2576 | 0.361 | 0.073 \pm 0.029 | 0.078 \pm 0.025 | 0.043 \pm 0.028 | ... | ... |
| N II λ 1084 | 0.111 | ... | 0.281 \pm 0.030 | 0.274 \pm 0.018 | 0.255 \pm 0.016 | 0.193 \pm 0.020 |
| Ni II λ 1317 | 0.057 | 0.040 \pm 0.011 | 0.059 \pm 0.012 | 0.041 \pm 0.012 | 0.036 \pm 0.016 | 0.012 \pm 0.017 |
| Ni II λ 1370 | 0.077 | 0.033 \pm 0.009 | 0.045 \pm 0.012 | 0.033 \pm 0.011 | 0.033 \pm 0.013 | 0.033 \pm 0.015 |
| Ni II λ 1709 | 0.032 | 0.035 \pm 0.007 | 0.040 \pm 0.010 | 0.029 \pm 0.009 | 0.028 \pm 0.009 | 0.027 \pm 0.009 |
| Ni II λ 1741 | 0.043 | 0.048 \pm 0.009 | 0.050 \pm 0.009 | 0.036 \pm 0.008 | 0.036 \pm 0.010 | 0.039 \pm 0.008 |
| Ni II λ 1751 | 0.028 | 0.035 \pm 0.009 | 0.042 \pm 0.011 | 0.035 \pm 0.008 | 0.028 \pm 0.010 | 0.027 \pm 0.009 |
| O I λ 1302 | 0.048 | 0.568 \pm 0.012 | 0.555 \pm 0.015 | 0.562 \pm 0.013 | 0.567 \pm 0.017 | 0.508 \pm 0.019 |
| S II λ 1250 | 0.005 | 0.051 \pm 0.010 | 0.075 \pm 0.013 | 0.065 \pm 0.012 | 0.035 \pm 0.017 | 0.068 \pm 0.026 |
| S II λ 1253 | 0.011 | 0.093 \pm 0.009 | 0.076 \pm 0.012 | 0.079 \pm 0.011 | 0.094 \pm 0.014 | 0.047 \pm 0.021 |
| S III λ 1012 | 0.044 | ... | ... | 0.083 \pm 0.061 | 0.104 \pm 0.032 | 0.075 \pm 0.027 |
| Si II λ 1020 | 0.017 | ... | ... | 0.156 \pm 0.040 | 0.128 \pm 0.027 | 0.133 \pm 0.024 |
| Si II λ 1304 | 0.086 | 0.492 \pm 0.012 | 0.478 \pm 0.013 | 0.457 \pm 0.012 | 0.458 \pm 0.016 | 0.391 \pm 0.019 |
| Si II λ 1526 | 0.133 | 0.634 \pm 0.009 | 0.634 \pm 0.010 | 0.624 \pm 0.011 | 0.634 \pm 0.012 | 0.557 \pm 0.013 |
| Si II λ 1808 | 0.002 | 0.102 \pm 0.010 | 0.099 \pm 0.010 | 0.085 \pm 0.009 | 0.077 \pm 0.010 | 0.051 \pm 0.011 |
| Si III λ 1206 | 1.630 | 0.763 \pm 0.014 | 0.730 \pm 0.017 | 0.736 \pm 0.015 | 0.763 \pm 0.019 | 0.665 \pm 0.023 |

Note. The values for \bar{z}_{DLA} are the mean values of each range, for which values of the rest-frame equivalent width W with its error are given for each line.

Table 13
Rest Equivalent Widths of Absorption High-ionization Lines with Respect to the Redshift for the Metal Sample

| \bar{z}_{DLA} Transition | f | 2.12 W (Å) | 2.32 W (Å) | 2.54 W (Å) | 2.84 W (Å) | 3.50 W (Å) |
|--------------------------------------|-------|-------------------|-------------------|-------------------|-------------------|-------------------|
| C IV λ 1548 | 0.190 | 0.608 ± 0.010 | 0.582 ± 0.011 | 0.550 ± 0.011 | 0.512 ± 0.013 | 0.444 ± 0.015 |
| C IV λ 1550 | 0.095 | 0.463 ± 0.008 | 0.438 ± 0.011 | 0.404 ± 0.009 | 0.358 ± 0.012 | 0.317 ± 0.013 |
| N V λ 1238 | 0.156 | 0.034 ± 0.012 | 0.021 ± 0.013 | 0.029 ± 0.016 | 0.035 ± 0.018 | 0.017 ± 0.024 |
| N V λ 1242 | 0.078 | 0.004 ± 0.013 | 0.004 ± 0.013 | 0.014 ± 0.017 | 0.007 ± 0.018 | 0.040 ± 0.025 |
| Si IV λ 1393 | 0.513 | 0.427 ± 0.009 | 0.402 ± 0.012 | 0.381 ± 0.010 | 0.377 ± 0.010 | 0.328 ± 0.018 |
| Si IV λ 1402 | 0.254 | 0.291 ± 0.008 | 0.269 ± 0.011 | 0.260 ± 0.007 | 0.248 ± 0.012 | 0.207 ± 0.014 |

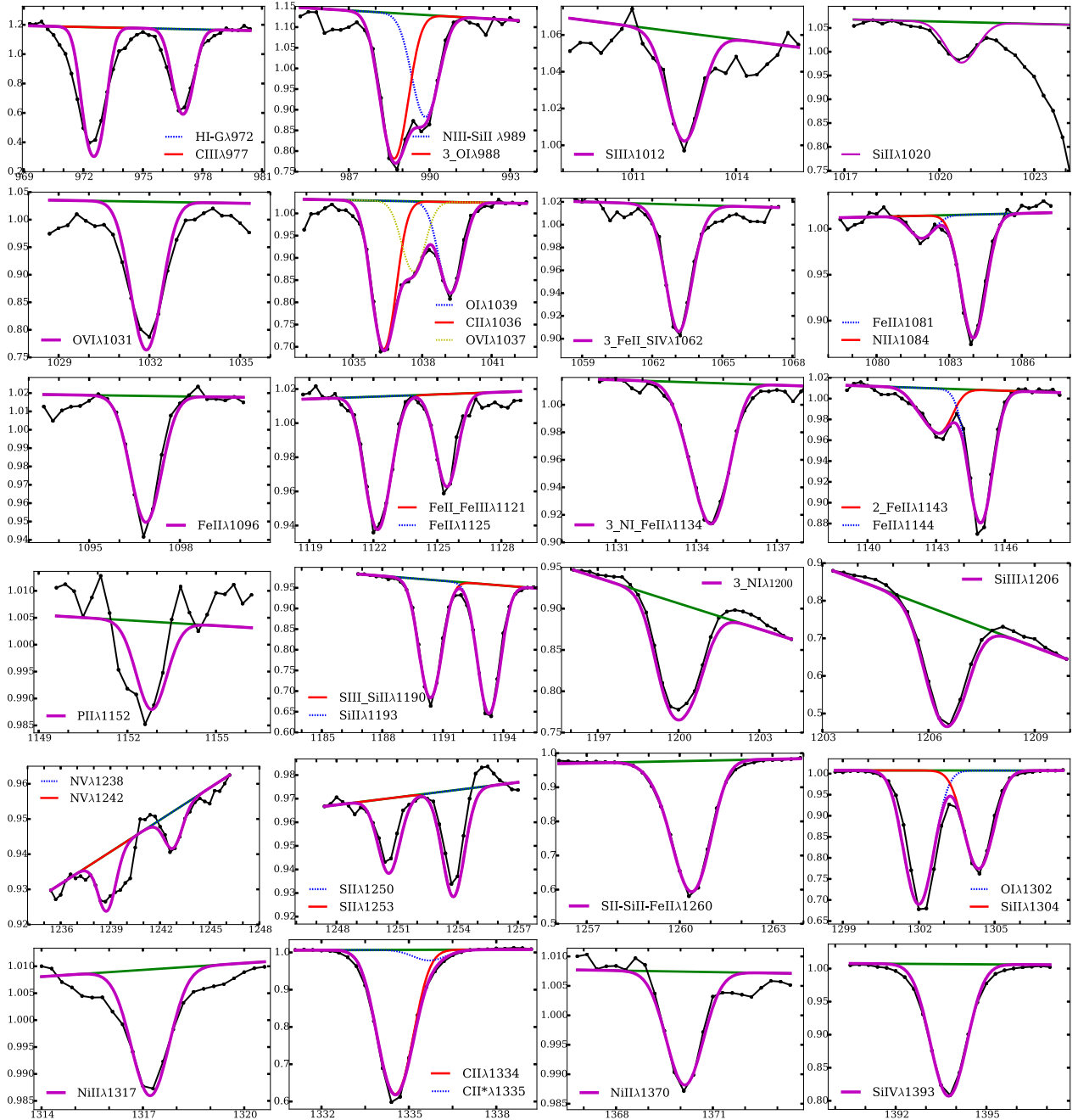


Figure 17. Absorption line profile fits for the total sample, denoting transmission as a function of DLA rest-frame wavelength (in Å). Black thin line: final stacked spectrum, with points indicating the data pixels. Green thick line: fitted continuum. Magenta thick line: Total fitted profile. Other lines (dotted thin blue and yellow, and solid red) represent the fits of individual absorption features. Good fits are generally obtained for the central parts of the lines. In some of the strong lines, the observed tails are broader than the fits, possibly due to the intrinsic velocity dispersions of the absorption systems. The $\text{Ly}\beta$ and $\text{Ly}\gamma$ lines are strong and have substantial damped wings, which explains why the fit is substandard in these cases. The fit to the Si II λ 1020 line does not account for the blend with the $\text{Ly}\beta$ line. The transmission scales vary with each panel to maximize the visibility of the lines.

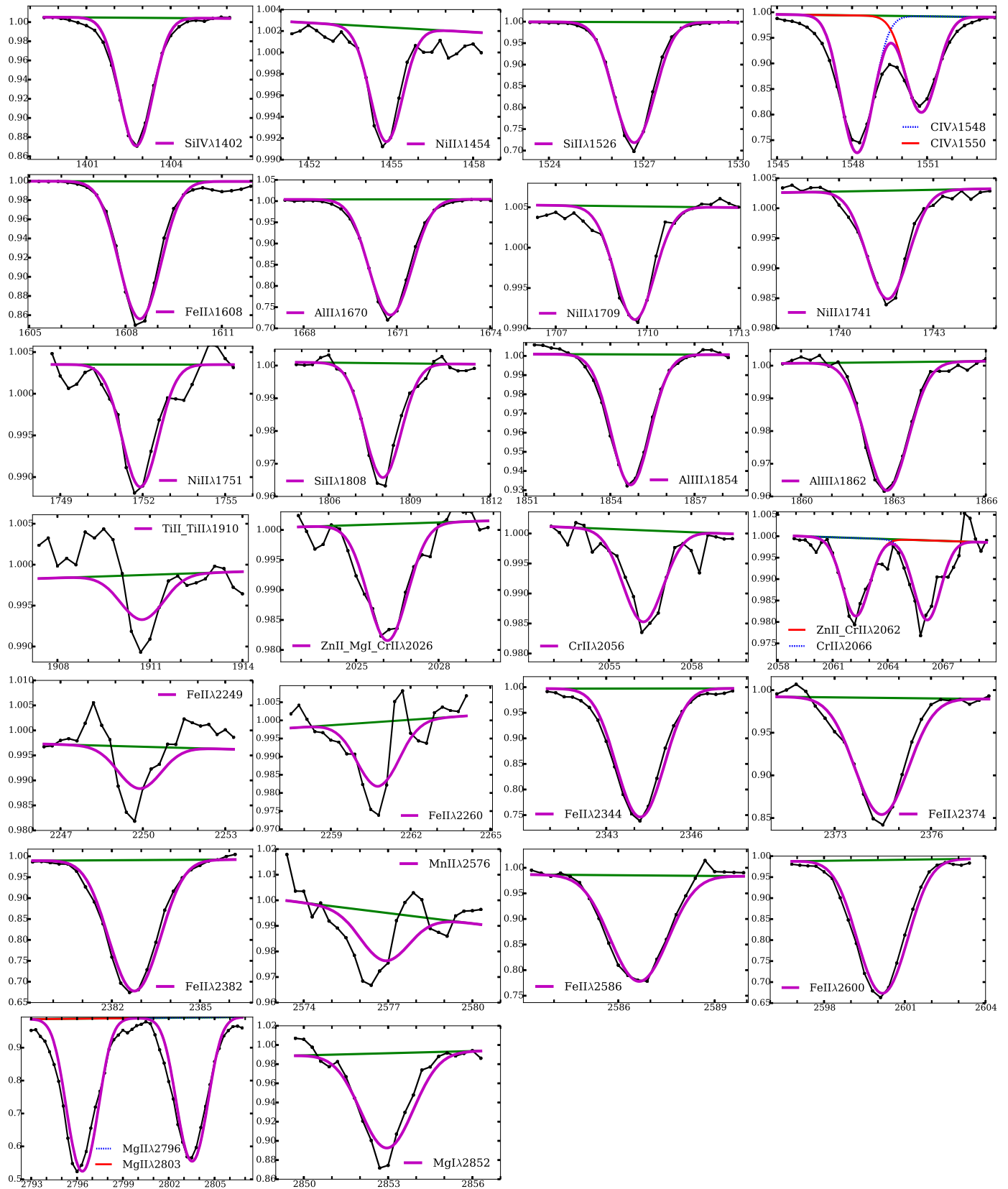



Figure 18. Continuation of Figure 17.

ORCID iDs

Lluís Mas-Ribas  <https://orcid.org/0000-0003-4584-8841>
 Andreu Arinyo-i-Prats  <https://orcid.org/0000-0001-8502-6725>

References

- Akerman, C. J., Ellison, S. L., Pettini, M., & Steidel, C. C. 2005, *A&A*, **440**, 499
- Alam, S., Albareti, F. D., Allende Prieto, C., et al. 2015, *ApJS*, **219**, 12
- Asplund, M., Grevesse, N., Sauval, A. J., & Scott, P. 2009, *ARA&A*, **47**, 481
- Baldwin, J. A. 1977, *ApJ*, **214**, 679
- Barnes, L. A., Garel, T., & Kacprzak, G. G. 2014, *PASP*, **126**, 969
- Barnes, L. A., & Haehnelt, M. G. 2014, *MNRAS*, **440**, 2313
- Bautista, J. E., Bailey, S., Font-Ribera, A., et al. 2015, *JCAP*, **5**, 060
- Berg, T. A. M., Ellison, S. L., Prochaska, J. X., Venn, K. A., & Dessauges-Zavadsky, M. 2015, *MNRAS*, **452**, 4326
- Berg, T. A. M., Ellison, S. L., Sánchez-Ramírez, R., et al. 2016, *MNRAS*, arXiv:1609.05968
- Berry, M., Somerville, R. S., Haas, M. R., et al. 2014, *MNRAS*, **441**, 939
- Bird, S., Haehnelt, M., Neeleman, M., et al. 2015, *MNRAS*, **447**, 1834
- Bland-Hawthorn, J., Sutherland, R., & Webster, D. 2015, *ApJ*, **807**, 154
- Boisse, P., Le Brun, V., Bergeron, J., & Deharveng, J.-M. 1998, *A&A*, **333**, 841
- Calura, F., Matteucci, F., & Vladilo, G. 2003, *MNRAS*, **340**, 59
- Cen, R. 2012, *ApJ*, **748**, 121
- Centurión, M., Molaro, P., Vladilo, G., et al. 2003, *A&A*, **403**, 55
- Cooke, R., Pettini, M., Jorgenson, R. A., et al. 2013, *MNRAS*, **431**, 1625
- Cooke, R., Pettini, M., Steidel, C. C., Rudie, G. C., & Nissen, P. E. 2011, *MNRAS*, **417**, 1534
- Cooke, R. J., Pettini, M., & Jorgenson, R. A. 2015, *ApJ*, **800**, 12
- Crighton, N. H. M., Murphy, M. T., Prochaska, J. X., et al. 2015, *MNRAS*, **452**, 217
- Dawson, K. S., Schlegel, D. J., Ahn, C. P., et al. 2013, *AJ*, **145**, 10
- Dessauges-Zavadsky, M., Calura, F., Prochaska, J. X., D'Odorico, S., & Matteucci, F. 2004, *A&A*, **416**, 79
- Dessauges-Zavadsky, M., Péroux, C., Kim, T.-S., D'Odorico, S., & McMahon, R. G. 2003, *MNRAS*, **345**, 447
- Dessauges-Zavadsky, M., Prochaska, J. X., D'Odorico, S., Calura, F., & Matteucci, F. 2006, *A&A*, **445**, 93
- Dutta, R., Srianand, R., Rahmani, H., et al. 2014, *MNRAS*, **440**, 307
- Eisenstein, D. J., Weinberg, D. H., Agol, E., et al. 2011, *AJ*, **142**, 72
- Ellison, S. L., Yan, L., Hook, I. M., et al. 2001, *A&A*, **379**, 393
- Ellison, S. L., York, B. A., Pettini, M., & Kanekar, N. 2008, *MNRAS*, **388**, 1349
- Fall, S. M., & Pei, Y. C. 1993, *ApJ*, **402**, 479
- Faucher-Giguère, C.-A., Prochaska, J. X., Lidz, A., Hernquist, L., & Zaldarriaga, M. 2008, *ApJ*, **681**, 831
- Font-Ribera, A., Miralda-Escudé, J., Arnau, E., et al. 2012, *JCAP*, **11**, 59
- Foreman-Mackey, D., Hogg, D. W., Lang, D., & Goodman, J. 2013, *PASP*, **125**, 306
- Foreman-Mackey, D., Price-Whelan, A., Ryan, G., et al. 2014, triangle.py v0.1.1, Zenodo, doi:10.5281/zenodo.11020
- Fox, A. J. 2011, *ApJ*, **730**, 58
- Fox, A. J., Ledoux, C., Petitjean, P., & Srianand, R. 2007a, *A&A*, **473**, 791
- Fox, A. J., Petitjean, P., Ledoux, C., & Srianand, R. 2007b, *A&A*, **465**, 171
- Fox, A. J., Prochaska, J. X., Ledoux, C., et al. 2009, *A&A*, **503**, 731
- Fukugita, M., & Ménard, B. 2015, *ApJ*, **799**, 195
- Fumagalli, M., O'Meara, J. M., Prochaska, J. X., Kanekar, N., & Wolfe, A. M. 2014, *MNRAS*, **444**, 1282
- Fumagalli, M., Prochaska, J. X., Kasen, D., et al. 2011, *MNRAS*, **418**, 1796
- Goody, R., & Yung, Y. 1996, *Atmospheric Radiation: Theoretical Basis* (Oxford: Oxford Univ. Press)
- Gunn, J. E., Carr, M., Rockosi, C., et al. 1998, *AJ*, **116**, 3040
- Gunn, J. E., Siegmund, W. A., Mannery, E. J., et al. 2006, *AJ*, **131**, 2332
- Haehnelt, M. G., Steinmetz, M., & Rauch, M. 1998, *ApJ*, **495**, 647
- Henry, R. B. C., & Prochaska, J. X. 2007, *PASP*, **119**, 962
- Hawk, J. C., & Sembach, K. R. 1999, *ApJL*, **523**, L141
- Jenkins, E. B. 2009, *ApJ*, **700**, 1299
- Jorgenson, R. A., Murphy, M. T., & Thompson, R. 2013, *MNRAS*, **435**, 482
- Khare, P., Kulkarni, V. P., Lauroesch, J. T., et al. 2004, *ApJ*, **616**, 86
- Khare, P., Kulkarni, V. P., Péroux, C., et al. 2007, *A&A*, **464**, 487
- Khare, P., vanden Berk, D., York, D. G., Lundgren, B., & Kulkarni, V. P. 2012, *MNRAS*, **419**, 1028
- Kisielius, R., Kulkarni, V. P., Ferland, G. J., et al. 2015, *ApJ*, **804**, 76
- Krogager, J.-K., Fynbo, J. P. U., Noterdaeme, P., et al. 2016, *MNRAS*, **455**, 2698
- Kulkarni, V. P., & Fall, S. M. 2002, *ApJ*, **580**, 732
- Kulkarni, V. P., Fall, S. M., Lauroesch, J. T., et al. 2005, *ApJ*, **618**, 68
- Kulkarni, V. P., Fall, S. M., & Truran, J. W. 1997, *ApJL*, **484**, L7
- Kulkarni, V. P., Khare, P., Péroux, C., et al. 2007, *ApJ*, **661**, 88
- Kulkarni, V. P., Som, D., Morrison, S., et al. 2015, *ApJ*, **815**, 24
- Ledoux, C., Noterdaeme, P., Petitjean, P., & Srianand, R. 2015, *A&A*, **580**, A8
- Ledoux, C., Petitjean, P., Fynbo, J. P. U., Møller, P., & Srianand, R. 2006, *A&A*, **457**, 71
- Lehner, N., Howk, J. C., Prochaska, J. X., & Wolfe, A. M. 2008, *MNRAS*, **390**, 2
- Lehner, N., O'Meara, J. M., Fox, A. J., et al. 2014, *ApJ*, **788**, 119
- McDonald, P., & Miralda-Escudé, J. 1999, *ApJ*, **519**, 486
- Meiring, J. D., Kulkarni, V. P., Khare, P., et al. 2006, *MNRAS*, **370**, 43
- Møller, P., Fynbo, J. P. U., Ledoux, C., & Nilsson, K. K. 2013, *MNRAS*, **430**, 2680
- Morton, D. C. 2003, *ApJS*, **149**, 205
- Murphy, M. T., & Bernet, M. L. 2016, *MNRAS*, **455**, 1043
- Neeleman, M., Prochaska, J. X., & Wolfe, A. M. 2015, *ApJ*, **800**, 7
- Neeleman, M., Wolfe, A. M., Prochaska, J. X., & Rafelski, M. 2013, *ApJ*, **769**, 54
- Noterdaeme, P., Petitjean, P., Carithers, W. C., et al. 2012, *A&A*, **547**, L1
- Noterdaeme, P., Petitjean, P., Ledoux, C., & Srianand, R. 2009, *A&A*, **505**, 1087
- Noterdaeme, P., Petitjean, P., Pâris, I., et al. 2014, *A&A*, **566**, A24
- Noterdaeme, P., Petitjean, P., & Srianand, R. 2015, *A&A*, **578**, L5
- Padmanabhan, H., Choudhury, T. R., & Refregier, A. 2015, arXiv:1505.00008
- Palanque-Delabrouille, N., Yèche, C., Borde, A., et al. 2013, *A&A*, **559**, A85
- Pâris, I., Petitjean, P., Aubourg, É., et al. 2012, *A&A*, **548**, A66
- Pâris, I., Petitjean, P., Ross, N. P., et al. 2016, arXiv:1608.06483
- Pérez-Ràfols, I., Miralda-Escudé, J., Lundgren, B., et al. 2014, arXiv:1402.1342
- Péroux, C., Dessauges-Zavadsky, M., D'Odorico, S., Kim, T.-S., & McMahon, R. G. 2003a, *MNRAS*, **345**, 480
- Péroux, C., Dessauges-Zavadsky, M., D'Odorico, S., Sun Kim, T., & McMahon, R. G. 2005, *MNRAS*, **363**, 479
- Péroux, C., McMahon, R. G., Storrie-Lombardi, L. J., & Irwin, M. J. 2003b, *MNRAS*, **346**, 1103
- Petitjean, P., Ledoux, C., & Srianand, R. 2008, *A&A*, **480**, 349
- Pettini, M. 2004, in *Cosmochemistry. The Melting Pot of the Elements*, ed. C. Esteban et al. (Cambridge: Cambridge Univ. Press), 257
- Pettini, M. 2006, in *Proc. of the 5th Marseille International Cosmology conference, The Fabulous Destiny of Galaxies: Bridging Past and Present*, ed. V. Le Brun et al. (Paris: Frontier Group), 319
- Pettini, M., Boksenberg, A., & Hunstead, R. W. 1990, *ApJ*, **348**, 48
- Pettini, M., Ellison, S. L., Bergeron, J., & Petitjean, P. 2002, *A&A*, **391**, 21
- Pettini, M., King, D. L., Smith, L. J., & Hunstead, R. W. 1997, *ApJ*, **478**, 536
- Pettini, M., Lipman, K., & Hunstead, R. W. 1995, *ApJ*, **451**, 100
- Pieri, M. M., Mortenson, M. J., Frank, S., et al. 2014, *MNRAS*, **441**, 1718
- Planck Collaboration 2015, arXiv:1502.01589
- Pontzen, A., & Pettini, M. 2009, *MNRAS*, **393**, 557
- Prochaska, J. X. 2003, arXiv:astro-ph/0310850
- Prochaska, J. X., Chen, H.-W., Wolfe, A. M., Dessauges-Zavadsky, M., & Bloom, J. S. 2008, *ApJ*, **672**, 59
- Prochaska, J. X., Gawiser, E., Wolfe, A. M., Castro, S., & Djorgovski, S. G. 2003a, *ApJL*, **595**, L9
- Prochaska, J. X., Gawiser, E., Wolfe, A. M., Cooke, J., & Gelino, D. 2003b, *ApJS*, **147**, 227
- Prochaska, J. X., Herbert-Fort, S., & Wolfe, A. M. 2005, *ApJ*, **635**, 123
- Prochaska, J. X., & Wolfe, A. M. 1997, *ApJ*, **487**, 73
- Prochaska, J. X., & Wolfe, A. M. 2002, *ApJ*, **566**, 68
- Prochaska, J. X., & Wolfe, A. M. 2009, *ApJ*, **696**, 1543
- Prochaska, J. X., Wolfe, A. M., Tytler, D., et al. 2001, *ApJS*, **137**, 21
- Quiet, S., Péroux, C., Zafar, T., et al. 2016, *MNRAS*, **458**, 4074
- Rafelski, M., Neeleman, M., Fumagalli, M., Wolfe, A. M., & Prochaska, J. X. 2014, *ApJL*, **782**, L29
- Rafelski, M., Wolfe, A. M., Prochaska, J. X., Neeleman, M., & Mendez, A. J. 2012, *ApJ*, **755**, 89
- Rahmani, H., Srianand, R., Noterdaeme, P., & Petitjean, P. 2010, *MNRAS*, **409**, L59
- Rahmati, A., & Schaye, J. 2014, *MNRAS*, **438**, 529

- Ross, N. P., Myers, A. D., Sheldon, E. S., et al. 2012, *ApJS*, 199, 3
- Rubin, K. H. R., Hennawi, J. F., Prochaska, J. X., et al. 2015, *ApJ*, 808, 38
- Sánchez-Ramírez, R., Ellison, S. L., Prochaska, J. X., et al. 2016, *MNRAS*, 456, 4488
- Shull, J., & Thronson, H. 2012, *The Environment and Evolution of Galaxies* (Amsterdam: Springer)
- Smee, S. A., Gunn, J. E., Uomoto, A., et al. 2013, *AJ*, 146, 32
- Smette, A., Wisotzki, L., Ledoux, C., et al. 2005, in *IAU Coll. 199, Probing Galaxies through Quasar Absorption Lines*, ed. P. Williams, C.-G. Shu, & B. Menard (Cambridge: Cambridge Univ. Press), 475
- Som, D., Kulkarni, V. P., Meiring, J., et al. 2013, *MNRAS*, 435, 1469
- Som, D., Kulkarni, V. P., Meiring, J., et al. 2015, *ApJ*, 806, 25
- Srianand, R., Petitjean, P., Ledoux, C., Ferland, G., & Shaw, G. 2005, *MNRAS*, 362, 549
- Trenti, M., & Stiavelli, M. 2006, *ApJ*, 651, 51
- Vladilo, G. 2002, *A&A*, 391, 407
- Vladilo, G., Abate, C., Yin, J., Cescutti, G., & Matteucci, F. 2011, *A&A*, 530, A33
- Vladilo, G., Centurión, M., Bonifacio, P., & Howk, J. C. 2001, *ApJ*, 557, 1007
- Vladilo, G., Prochaska, J. X., & Wolfe, A. M. 2008, *A&A*, 478, 701
- Webster, D., Bland-Hawthorn, J., & Sutherland, R. S. 2015, *ApJ*, 804, 110
- Welty, D. E., Frisch, P. C., Sonneborn, G., & York, D. G. 1999, *ApJ*, 512, 636
- Wolfe, A. M., Gawiser, E., & Prochaska, J. X. 2003, *ApJ*, 593, 235
- Wolfe, A. M., Gawiser, E., & Prochaska, J. X. 2005, *ARA&A*, 43, 861
- Wolfe, A. M., Howk, J. C., Gawiser, E., Prochaska, J. X., & Lopez, S. 2004, *ApJ*, 615, 625
- Wolfe, A. M., & Prochaska, J. X. 1998, *ApJL*, 494, L15
- Wolfe, A. M., & Prochaska, J. X. 2000, *ApJ*, 545, 591
- Wolfe, A. M., Turnshek, D. A., Smith, H. E., & Cohen, R. D. 1986, *ApJS*, 61, 249
- York, D. G., Adelman, J., Anderson, J. E., Jr., et al. 2000, *AJ*, 120, 1579
- York, D. G., Dopita, M., Green, R., & Bechtold, J. 1986, *ApJ*, 311, 610
- York, D. G., Khare, P., Vanden Berk, D., et al. 2006, *MNRAS*, 367, 945
- Zafar, T., Centurión, M., Péroux, C., et al. 2014, *MNRAS*, 444, 744
- Zafar, T., Péroux, C., Popping, A., et al. 2013, *A&A*, 556, A141
- Zwaan, M., Walter, F., Ryan-Weber, E., et al. 2008, *AJ*, 136, 2886